ANALYSIS OF SCLERAL BUCKLING SURGERY: BIOMECHANICAL MODEL

by

Raed Aldhafeeri

B. S. in Mechanical Engineering, King Fahd University of Petroleum and Minerals, 2009

M.S. in Mechanical Engineering, University of Pittsburgh, 2015

Submitted to the Graduate Faculty of

Swanson School of Engineering in partial fulfillment

of the requirements for the degree of

Doctor of Philosophy in Mechanical Engineering

University of Pittsburgh

2017

UNIVERSITY OF PITTSBURGH

SWANSON SCHOOL OF ENGINEERING

This dissertation was presented

by

Raed Aldhafeeri

It was defended on

July 21, 2017

and approved by

Patrick Smolinski, PhD, Associate Professor

Mark C Miller, PhD, Associate Professor

Qing-Ming Wang PhD, Professor

Thomas Friberg, MD, Professor

Dissertation Director: Patrick Smolinski, PhD, Associate Professor

ANALYSIS OF SCLERAL BUCKLING SURGERY: BIOMECHANICAL MODEL

Raed Aldhafeeri, PhD

University of Pittsburgh, 2017

The objective of this study was to analyze deformation and stresses and resultant refractive error of human eyes subjected to scleral buckling surgery by encircling band; and segmental buckle with encircling buckling. Experimental evaluation of buckling of the eye was conducted using animal model for evaluation of the axial length change and tilting of the cornea. For different segmental buckle widths and extents, the axial length increased and cornea tilt increased for all models. Axisymmetric and three-dimensional finite element models of the eye and buckles were constructed to calculate eye deformation. The analysis found that the change in the axial length, which is a factor in the myopia of the eye is mainly influenced by the amount of indentation. Steepening of the cornea and thus cornea and total eye power are mainly effected by the cornea thickness in addition to the indentation. The width of the band or buckle and band location have no effect on myopic shift. The reduction of the anterior chamber depth increased for band closer to limbus and with less cornea thinning where width of the band and the buckle and extent of the buckle had no effect. Additional types of refractive errors and deformation were encountered in buckled eye. The astigmatism of the cornea increased with increased indentation, corneal thinning and extent of the segmental buckle. Tilting of the cornea away from the center of the buckle was observed and it increased for higher indentation and decreased extent of the buckle. Greater indentation induced more displaced vitreous cavity volume and maximum stresses in the sclera. The maximum stress was located at the sclera-choroid interface and in at sclera surface close to the buckle edge contact location. Pressure-volume relationship was modeled for eyes with and without buckling by increasing the pressure and recording the added fluid volume and linear relationship was found for all models. The slope of the relationship can give rigidity factor for each model where the buckled eyes had less rigidity. The rigidity also showed decrease in thinner band, higher indentation, shorter buckle, thinner cornea and for band closer to the limbus.

TABLE OF CONTENTS

LIST OF TABLES

LIST OF FIGURES

ACKNOWLEDGMENT

I wish to express my sincere gratitude to Allah (God) for providing me with patient and wisdom in completion of this work.

I would like to express my appreciation to my advisor Dr. Patrick Smolinski for his full support, understanding and encouragement through my study and research. With his guidance, I had new experiences in conference meetings, publications and conducting interesting researches. I express my appreciation to Dr. Thomas Friberg for his brilliant ideas and Dr. Qing-Ming Wang and Dr. Mark Miller for serving in my master and dissertation committee.

I would like to thank all my family especially my parents for their love and prayers. I would like to thank my brothers especially Najem Alsuwait, sisters and my wife for their love and support.

1.0 INTRODUCTION

Scleral buckling is an ophthalmology surgery for treatment of retinal detachment (RD). The surgery is based on an indenting the eye using a buckle or band in area parallel to the retina breaks or detachment inside the eye. The surgery has been in use since 1949 (Brinton D. 2009) and 25,000 Americans per year in the range of 40-70 years old are diagnosed with retinal detachment (sightwise.org., Obi et al. 2005).

Scleral buckling surgery can cause changes in the eye vision, angle-closed glaucoma and ciliary body edema (Kawana et al. 2006). Many clinical measurements have been performed after the procedure to measure the deformation of the eye leading to visual changes with different conclusions and results. The scleral buckling procedure can vary due to many surgical specifications, for example, the amount of indentation, buckle thickness, location and extension of the buckle. Common preoperative conditions of the eye, for example, eyes subjected to corneal thinning are an important issue to consider in the procedure. Therefore, a study considering different surgical variables and eye conditions is needed to analyze their effects on eye deformation and vision. Information on this can aid in predicting surgical outcome.

In engineering applications, the finite element analysis is a commonly used method in modeling the deformation and the stresses in structures resulted from prescribed loads. It has been used for modeling the eye deformation for different purposes. Here, the finite element models of the eye will be generated for analyzing the deformation and stresses and the resulting change in vision by simulating the effect of contact buckling to the eye.

Two different models will be used in this study. The axisymmetric model is used for indentation by full encircling band to analysis the effect of different pre-thinning of the cornea, widths, indentations amount and locations of the band. Since with partial buckle the axisymmetric geometry is not preserved, a planar symmetric three-dimensional model is used for buckling with partial segmental buckle to investigate the effect of different buckle widths and extents on vision. A sensitivity analysis is performed using the model and experimental testing is done using a porcine model.

The study is offering advantages in predicting outcomes of scleral buckling more accurately and disadvantageous outcomes of different specifications of the surgery than by the clinical measurements. In addition to the specifications of the surgery, it gives the effect of the preoperative condition of the cornea namely thinning of the cornea. Thus, the surgery can be improved by avoiding or minimizing such outcomes. Also, the study provides finite element models of the eye which can be used for buckling or other related surgeries.

A limitation of this study is the use of linearly elastic material properties for the eye tissues as linearized elastic materials. This is done because of the lack of data for the use of hyper-elastic material models.

In the introduction of this dissertation, an overview of eye anatomy and optics and scleral buckling is given. Also, previous studies of eye tissues mechanical properties, finite element models of eye and clinical results of scleral buckling are presented. This is followed by discussion of the finite element modeling. Finally, there is presentation of experimentation and results of the computer analysis.

2.0 BACKGROUND

2.1 EYE ANATOMY

The eye globe has a sphere-like shape embedded in a bony orbit filled with fatty tissues, vessels, supportive tissue and six extraocular muscles attached to the eye. The globe is divided into the aqueous and vitreous cavities (Figure 2.1).

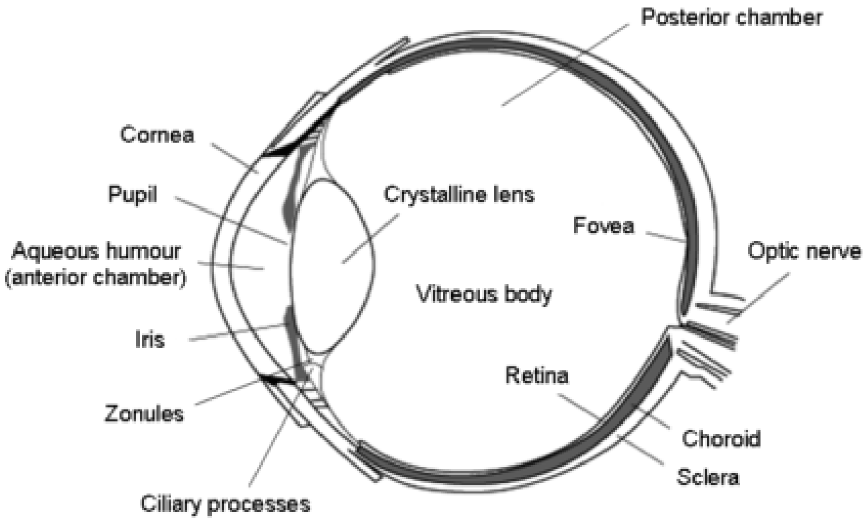

Figure 2.1 Eye cross section with different tissues structures (Biano F 2010a).

The eye globe mainly consists of three layers: the fibrous layer (sclera and cornea), the middle vascular layer (the choroid, iris and ciliary body) and the inner nerve layer (retina). The vitreous cavity contains the vitreous humor which is a transparent jelly-like fluid. The vitreous cavity wall consists of the sclera, choroid and retina tissue layers. The sclera is the thickest layer and is a white stiff tissue with varying thickness providing protection for the other tissues and preventing light transmission into the eye. The choroid is a thin vascular tissue from which the ciliary body, the iris and the zonulas fibers extended. The iris is the colored tissue at the front eye with pupil as the central opening. The pupil controls the amount of light that enters the eye. Zonulas fibers are attached to the lens, and adjust its geometry to focus light into the retina. The retina is the innermost layer in the vitreous cavity containing light receptors, which convert light to signals running to the brain through a back-inserted optic nerve.

The scleral joins the cornea in front of the eye at a junction called the limbus in the aqueous cavity. The geometry of the aspheric cornea provides refraction of light into the eye. The aqueous cavity contains water-like fluid called aqueous humor which provides nutrients and cleans the interior optical tissues. It is produced in posterior chamber from the ciliary body and flows into the anterior chamber and drains in Schlemm's canal at the limbus. Both humors in the eye have an intraocular pressure (IOP), which is about 12-18 mmHg.

The eye globe is separated from the fatty tissue and muscles by Tenon’s capsule which is a thin sheet extended from the optic nerve to the limbus. The eyelids and the capsule are connected by the conjunctiva at the anterior portion of the eye. The six extraocular muscles are attached to the globe include four rectus muscles (superior, inferior, medial and lateral rectus) and two oblique muscles (superior and inferior oblique). The configuration of the muscles provides the movement of the eye.

Figure 2.2 shows the terms used to define the meridians of the right eye from back view of the globe and the quadrants of the eye are called by the axis normal to its area. The sclera is divided into three main regions from far to near the optic nerve head: anterior, equatorial and posterior sclera which is divided into peripapillary, peripheral sclera.

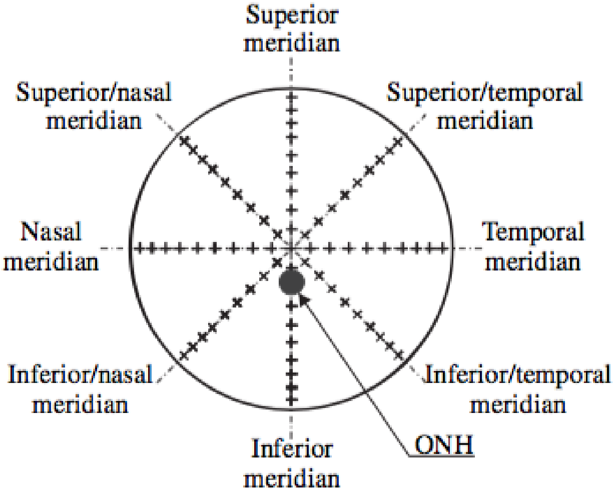

Figure 2.2 Meridians of the right eye globe (Elsheikh et. al 2010a).

2.2 EYE OPTICS

The eye is a multi-lens system where the light is refracted first at the cornea, then in the lens through the pupil, and converge at an image point to the retina surface. The optical power of a surface is measured in diopters which is the reciprocal of the meter. The power of a refracting thin medium which is between two other mediums is the ratio between the difference of their refraction indices and the surface radius of curvature. Increasing the curvature results in decreasing the absolute power of a lens and vice versa. A thick lens can be considered to have the power of two thin surfaces where the effect of the thickness is subtracted from the total power of the lens.

The crystalline lens consists of three parts: thin capsule, cortex and nucleus. Each of these is a lens with a specific radius of curvature and refractive index. The composite lens is considered as one refractive lens with an averaged index representing less than 30% of the eye total visual power. The lens can change its curvatures using a physiological mechanism called accommodation (focusing), where it is only activated for a small range with a small correction to the lens' power (Atchison et al. 2008).

Since the difference of refractive indices between the cornea and the air is larger than differences between any other surfaces in the eye, most of the light is refracted at the cornea, and its curvature represents about 70% of the total eye power. The cornea, lens and cornea-lens distance all determine the focal length, which is the travel distance of light inside the eye.

The axial length of the eye is the geometric distance from the anterior of the cornea to the surface of the retina. If both the focal and the axial length are equal, the optical power of the eye is normal and the eye is called an emmetropic eye. However, if the former is shorter than the axial length, the light will fall before the retina (myopic eye) and the opposite is true for hyperopic eye (Figure 2.3).

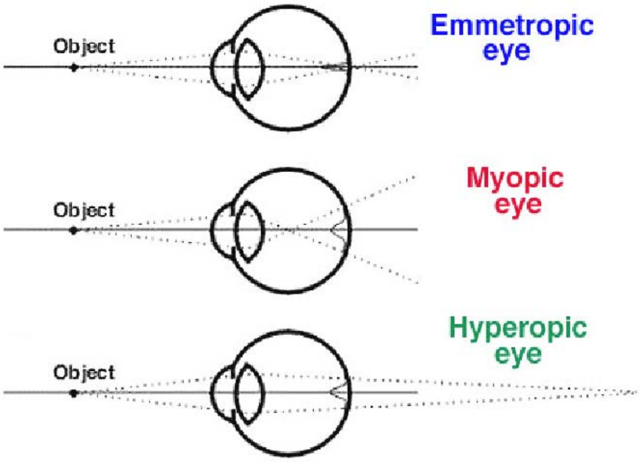

Figure 2.3 Different vision states of the eye (http://webvision.med.utah.edu).

Asymmetry of the cornea anterior surface (astigmatism) is another important refractive error which results in multiple images developed in the eye. Astigmatism is mainly caused when meridians axes on surface of the cornea have different curvatures. The orientation between the flat and steep axes can be 90˚ degrees as in regular astigmatism or different than 90˚ degrees as in irregular astigmatism.

The correction of common refractive errors can be done by introducing a negative/positive lens using eyeglasses, contact lens or by reshaping the anterior curvature of the cornea using refractive surgeries, for example, LASIK (laser-assisted in situ keratomileusis) and PRK (photorefractive keratectomy).

2.3 RETINAL DETACHMENT AND SCLERAL BUCKLING

Retinal detachment (RD) is a separation of the neurosensory retina from the underlying pigment epithelium. It is commonly treated with the scleral buckling procedure in a band or buckle is placed around the eye and tensioned causing an indentation in the eye forcing the layers back together. The buckle can have various shapes and circumferential lengths.

2.3.1 Retinal detachment

The types of the retinal detachment and the treatment methods are determined by the cause and the shape of the detachment. Rhegmatogenous retinal detachment (RRD) is where the vitreous fluid enters the sub-retinal space through a retinal tear. Tractional retinal detachment (TRD) results by pulling the retina by fibrovascular tissue. Exudative RD (ERD) is caused by fluid leakage from blood vessels. The last two types are usually caused by trauma, inflammation or abnormal blood vessels. At middle and old age, diseases can cause the most common type of detachment, RRD, for example, posterior vitreous detachment (PVD) where the vitreous humor shrinks due to certain changes in the compositional changes and pulls the retina and creating a break in addition to traction points.

A retinal detachment causes a partial loss of vision, where the detached retina blocks the light entering the eye. If not treated, it can progress to total detachment of the posterior retina leading to complete vision loss.

Procedures for treating retinal detachment are laser retinopexy, retinal cryopexy, pneumatic retinopexy, vitrectomy and scleral buckling. These procedures can be combined or done individually depending on the type of the detachment. The first method is simply applying a laser around the retina break developing a scar for reattaching the retina, and it is applicable for a small tear, a weak retina or a retina having abnormal blood vessels. For larger tears and for areas that cannot be reached by a laser, a retinal cryopexy probe is used for freezing the detached area outside the eye to seal it. Pneumatic retinopexy is a procedure where gas is injected in the vitreous chamber forcing the sub-retinal fluid to flow out of the sub-retina space and the patient is oriented in a position to ensure the gas gets to the detached location. Vitrectomy is the removal of partial or full volume of the vitreous humor which is used for removing blood, scar tissue and the vitreous tractions on the retina in addition to sealing the tear. Scleral buckling is a more common procedure involving indentation of the sclera using a buckle for closing the break and reattachment of the retina.

2.3.2 Scleral buckling procedure

The scleral buckling procedure can vary depending on factors such as the eye condition, the location and shape of the retinal detachment, whether a single or multiple tears exist, buckle shapes and the surgeon’s experience. The general buckling procedures are circumferential or segmental, radial, encircling buckle alone or in combination with the previous buckles. The segmental buckle is oriented parallel to the limbus junction, whereas the local buckle direction is normal to the limbus where both alone are buckled mainly by suturing. The encircling buckle is a band tightened by reducing its circumferential length around the full circumferential of the eye (Figure 2.4).

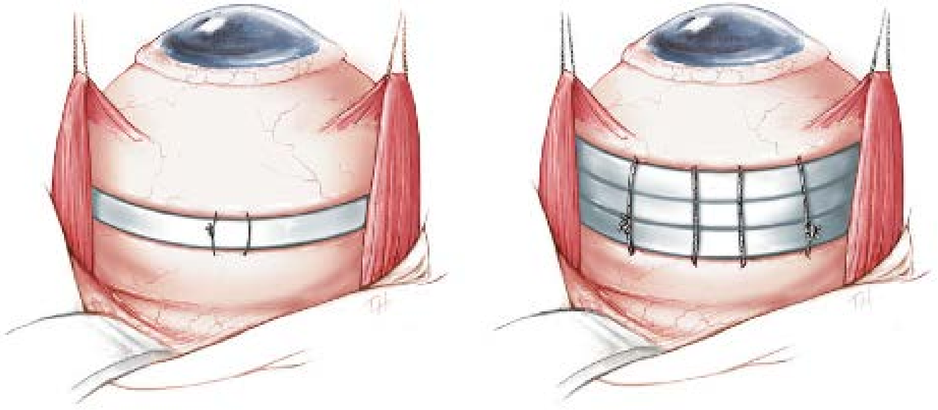

Figure 2.4 Encircling buckle (left), segmental buckle with encircling buckle (right) (Brinton et al. 2009).

The first step of the buckling procedure is to make a 360-degree incision in the eye conjunctive tissue which attached the eyelids to the Tenon’s capsule on the globe. Four sutures are inserted under the four rectus muscles to control the movement of the globe exposing more surface area of the eye. The retina breaks are located and marked at the sclera's surface (Figure 2.5) and sutures are applied at three to five mm from the buckle and in one to two-thirds of the sclera thickness. Finally, the buckle is placed and tightened if it is an encircling buckle, or the sutures bed are tightened if it is a local buckle (Williams and Aaberg 2006, Brinton et al. 2009).

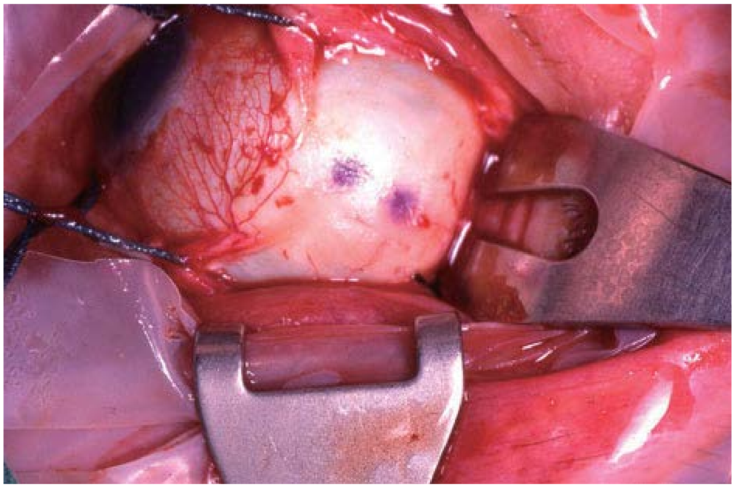

Figure 2.5 Marked location of RD on sclera surface (Brinton et al. 2009).

There are many sizes and shapes of buckles and different materials have been used for the buckle. However today, solid silicone rubber is the most common buckle material since it is pliable, cheap and has minimal long-term complications, such as scleral erosion, increase of the intraocular pressure or foreign body sensation. The silicone buckles can be solid or porous and buckles can have a variety of shapes (Figure 2.6).

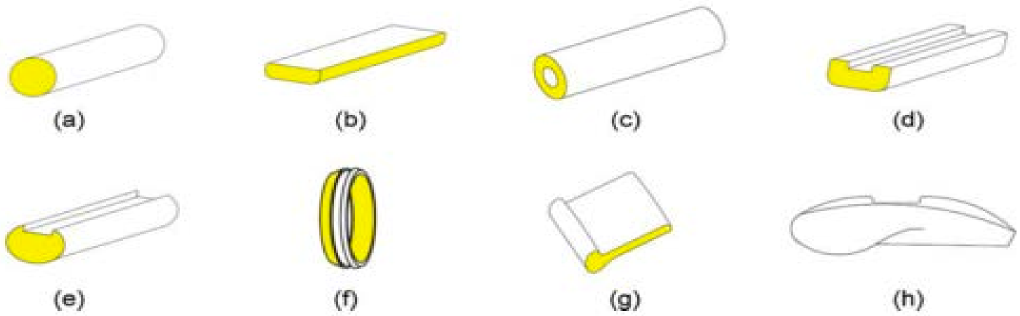

Figure 2.6 Different solid silicon buckles: (a) round, (b) flat, (c) round with sleeve, (d and e) grooved, (f) tire, (g) meridional and (h) wedge buckle (Biano F 2010a).

Rounded buckles are used to eliminate the sclera erosion reported in buckles with sharp edges, however, it can cause higher localized tension on the sclera surface, which can be eliminated by the flat buckle with rounded edges. Grooved buckles accompanying the flat bands can achieve a wider buckling on the sclera. Partial or full tire are stiffer than buckles with other shapes due to their curved designs and are available in different shapes: convex, concave and asymmetric for the desired indentation. Encircling rounded sleeve bands have threaded ends to attach them together and other bands can be attached using clips and stitches in the sclera (Baino F 2010a, b).

3.0 LITRATURE REVIEW

3.1 MECHANICAL PROPERTIES OF SCLERA, CORNEA AND LENS

Living tissues typically have nonlinear, viscoelastic, highly incompressible and anisotropic material properties because of their content of high fluid and distributed fibers. The mechanical behaviors of the sclera, cornea and lens have been most widely investigated since they comprise most of the eye structure and because of their significant role in visible power of the eye.

3.1.1 Sclera

The sclera consists of 50-75% of collagen and has a 68% of water content. The stroma is the main part of the sclera, which has multiple layers of dense lamellae, each of which has collagen bundles running with different orientations and parallel with respect to each other and to the surface of the sclera. The stroma also contains blood vessels, nerves and distributed elastin fibers (Keely et al. 1984, Boubriak et al. 2000).

Woo et al. (1972) used a testing chamber where seven posterior segments of human eyes were mounted and pressurized using a saline injection. The deformation was measured based on a photo reflection of two parallel thin strips placed a few millimeters apart on the sclera away from the optic nerve head. These strips were oriented at three different angles: 0, 45 and 90 degrees for investigating isotropy of the sclera. By alternating the pressure from 4 to 40 mmHg in two minutes, the sclera showed a nonlinear, exponential-like stress-strain relationship, negligible hysteresis and in-plane anisotropy. Also, an axisymmetric finite element model was used for obtaining constants of a trilinear constitutive relation of the sclera.

Graebel and van Alphen (1977) performed uniaxial test on nine strips of human sclera of various having different ages (4-88 years old). The resultant stress-strain curves were nonlinear and the stiffness increased as the age increased. The relationship was expressed in an exponential equation with two coefficients analogous to each sample estimated using thin shell governing equations.

The earliest experiment for determining the stiffness of the sclera in the radial direction was conducted by Battagioli and Kamm (1984). Eight cylindrical samples with 9 mm diameter and a 1 mm thickness were taken from anterior of three aged human eyes. Using a compression test at a low strain rate and an optical probe for measuring the displacement, the results showed that the radial stiffness was highly linear with greater compliance than the in-plane direction by more than two orders of magnitude and the Poisson ratio range was 0.46-0.5. In addition, there was some viscoelastic creep effect and hysteresis but no plastic behavior.

Friberg and Lace (1988) investigated the sclera elasticity and its relation with age. Sixity-four sclera strips of different orientations and locations were completely immersed and uniaxially tested in a strain rate of 0.1 mm/s. The results showed that the modulus of elasticity is approximately linear, the posterior sclera is less stiff than the anterior sclera by 40% and the average globe elasticity increased linearly with the sample age.

Bisplinghoff et al. (2009) investigated the dynamic material properties of human sclera by applying high loading rate pressure to the globe through the optic nerve head until rupture. The true stress was calculated using a thin sphere formula and the true strain by tracing a square of five markers at the equator with high speed camera measuring the normal and parallel strains to the eye axial axis. The resultant average rupture stress was 13.89 MPa at 30.78 milliseconds and the parallel maximum strain was higher than the normal strain, whereas both had a similar stress-strain relationship.

Another unconfined compression test following Battaglioli and Kamma (1984) was done by Mortazavi et al. (2009) in addition to a stress relaxation test. From 10 human sclera, 5 mm cylindrical samples were extracted from inferior-nasal quadrants close to the optic nerve head. The averaged stress-strain curve had some nonlinearity where the resultant drained moduli were 1.1,1.09 and 1.47 KPa for 5%,10% and 15% of strain, respectively.

Elsheikh et al. (2010a) investigated the stiffness of the scleral at different locations around and away from the optic nerve head with 8% and 200% strain rate. Testing 36 human sclera having a mean age of 62.3 years, where five strips of 20 by 4 mm were extracted from anterior, equatorial and posterior locations in each eye. The stress-strain curves showed that the tangent module increases as the strain rate, age and the distance from the optic nerve head increases. They also obtained an average stress-strain relationship for the sclera fitted to an exponential equation.

Eliaghi et al. (2010) studied the elasticity of the posterior sclera and its anisotropy using 10 sclera obtained from five donors at an average age of 55.4 years. Equibiaxial tests with repeated load cycles of low strain rate were applied to 30 samples obtained from equal orientations around the optic nerve head. By fitting the results to a reduced form of the Fung exponential model, there was no significant anisotropy within each sample or between orientations of different samples in each eye and between the right and left eye. Furthermore, at low stress, the averaged linear elasticity modulus was close to the reported values by Woo et al. (1972) and Friberg and Lace (1988).

Geraghty et al. (2012) did uniaxial tests on five samples of 4 by 12 mm tissue per eye extracted from 45 human sclera of different ages. Two from the anterior, two from equator and one from posterior sclera were tested at low strain rate of 1mm/min (8%) up to 1 MPa. The resultant stress-strain curves of the tenth cycle were nonlinear with lower stiffness than curves in the proceeding cycles. The tangent modulus ratio between the modulus at the last and the initial stress were similar for all locations. The tangent modulus increased by 24% and 54% from posterior to equatorial sclera and from equatorial to anterior sclera, respectively. Stiffening increased from the first to third cycle where negligible changes were observed up to the tenth cycle, and the older samples stabilized faster than the younger samples. As the age of the sample increased, the stiffening increased especially at the anterior region, and the differences between two successive decade groups were insignificant.

Courdriller et al. (2012) conducted inflation tests at a low strain rate on 24 normal human sclera and 12 with glaucoma. The strains at peripapillary (close to the nerve) and peripheral sclera were transformed to in-plane Cartesian and spherical coordinates, respectively, and the stresses were calculated using thin ellipsoidal membrane equations. The accompanied incompressible anisotropic hyperelastic constitutive model with two unidirectional in-plane fibers was represented by an exponential relation, and the matrix was assumed isotropic and assigned to Neo-Hookean model. The results showed that all eyes had similar thickness variation, where they were thicker at the superior-temporal than the inferior-nasal quadrant and they are thicker in younger eyes and in eyes with glaucoma. The sclera's response showed nonlinear and time-dependent behavior with hysteresis and creep at constant loads; and an increased stiffness as the sclera get old in both directions in the mid-posterior region. In peripapillary region, meridional and circumferential strains were higher in normal eyes than eyes with glaucoma and most of the sclera samples had more meridional than circumferential strains in both regions.

Fazio et al. (2014) did inflation tests on 19 human eyes using a 3D digitizer used to obtain the displacement as continuous function from which five directional strains were obtained, three using strain compatibility equations and the last one by assuming incompressibility. The averaged results showed that strains were higher at the edge of constrained samples and close to the optic nerve head, where the tensile maximum principle strain decreased as age increased at the peripapillary region, whereas strains at the mid-peripheral region did not significantly decreased. However, the nasal part at the mid-peripheral region and inferior-temporal part at the peripapillary region showed softening as the age increased.

The sclera shear behavior had not been well characterized until Argento et al. (2014) conducted shear tests using a tensile tester at body temperature on hydrated bovine sclera samples at 1 mm/min strain rate up to failure. The 142 samples were extracted from different quadrants, orientations, and within two locations from the optic nerve head. Their results of in-plane and out-of-plane shear tests showed that both have negligible nonlinearity within 0-2% strain with 0.2 MPa failure stress and no dependence on the orientations and quadrant locations. The in-plane shear modulus was 3.7-9.3 times higher than out-of-plane modulus, and the out-of-plane shear did not vary with respect to the distance from the optic nerve head. Stress relaxation and creep tests showed that samples have higher viscosity coefficient in in-plane direction.

3.1.2 Cornea

The cornea accounts for about two-third of the eye’s visual power. Altering its stiffness and geometry has a large impact on its refractive power. It mainly consists of five distinct layers from the anterior to posterior surface: external epithelium, Bowman’s membrane, stroma, Descemet’s membrane and the internal epithelium, where the stroma accounts for 90% of the cornea thickness. The stroma contains about 80% water and 200-500 sheet-like lamella, where most collagen fibers are parallel to each other except a small interweaving pattern at the anterior of the cornea. A high density of the fibers run in the nasal-temporal direction and in the superior-inferior direction, where they arrange themselves parallel to the cornea’s edge at limbus (Ruberti and Klyce 2001, Pinsky et al. 2005).

Woo et al. (1972) in the same experiment discussed previously for the sclera, used the same procedure for 15 anterior segments of the cornea. The results showed that the cornea had nonlinear, exponential like stress-strain relationship, very small visco-plastic effect and some plane anisotropy. Moreover, axisymmetric finite element model of the anterior segments were used for obtaining constants of a trilinear constitutive relation for cornea.

Hoeltzel et al. (1992) performed uniaxial tests with three cycles for preconditioning 2 by 10-20 mm strips of four human, three bovine and three rabbit corneas at 0.5mm/min elongation rate. The second and third cycles had 0.9 and 1% strain, respectively. A nonlinear stress-strain relationship was fitted to a power function, where the power coefficient was about two.

Bryant et al. (1994) performed uniaxial tests with a 1 Newton preloaded on nine 2x4 mm strips of normal corneas from the cornea center and four strips from the peripheral location having radial keratotomy (RK) normal to their length. In addition to inflation testing of cornea with four incisions oriented at the 0˚, 90˚, 180˚ and 270˚ meridians up to failure. Under tension the results showed that the average failure stresses and strains were 19.1 MPa and 0.211 for normal corneas, and 16.6 MPa and 0.178 for incised corneas, where the failure in the former was either normal or oblique to the direction of the load, and in the latter corneas it was along the incisions. The pressurized corneas had large gaps in the incisions within a pressure range of 30-40 psi, and the rupture occurred at 50 psi. A symmetric nonlinear finite element model of incised cornea with different epithelial plugs was given in the same study and it showed that if 90% of the cornea thickness was removed, the stress in the incision will be higher than the strip by 50%.

Elsheikh et al. (2007, 2008) did inflation tests from 0.75 to 170 mmHg on 23 and 13 corneas at pressure rates of 37.5 and 3.75 mmHg/min, respectively. The specimens were divided into three age groups of 50 to 64, 65 to 79 and 80 to 95 years. Analysis of the results using a linear relationship of the modulus and the pressure along with shell theory resulted in two moduli: secant and tangent modulus. The results after the third pressure cycle showed that the deformation was large up to 12-20 mmHg then the stiffness increased as the stress increased, and the modulus was almost linear from 0 to 75 mmHg. Increased age or loading rate increased the stiffening effect. In the following published work the hysteresis was calculated as the difference between areas during loading and unloading stress-strain curves and concluded that a high pressure rate had more hysteresis with a negligible difference between ages. Elsheikh et al. (2010b) in a later investigation of the age included 59 corneas with 30-90 years old to increase the age range of the study. Similar previous study, the testing produced the same conclusions, and the average stress-strain curves were fitted to an exponential function.

Characterization of the transverse shear along the thickness of the human cornea was conducted by Petsche et al. (2012) using a torsional rheometer. In their study, each of four human cornea pairs were laser cut to three depths: anterior, central and posterior cut at a 6 mm diameter. The shear modulus increased with increasing the compressive stress and strain with a nonlinear relationship. For each layer, a mean shear modulus was calculated at 0% strain, which decreased from the anterior to posterior cornea, and the full cornea modulus was larger than all layers' modulus.

3.1.3 Lens

The lens is an important part in the visual power of the eye in that it controls the focusing power of the eye. The lens mainly consists of three parts: thin capsule, cortex and nucleus. Accommodation, diseases, and cataract surgery are the main purposes for the lens' mechanical properties investigations.

Fisher R. (1971) did spinning test on 40 isolated lenses to stimulate the thinning of the lens by the zonular fibers, where the stress, strain, and the elasticity modulus were approximated by assuming the lens is composed of an infinite number of staked disks. The in and out-of-plane stress-strain data had S-shaped curves, where the latter had plasticity occurred at 1250 rev/min, and both strains increased with the age. The lens modulus was linear up to 35 years old and then increased with the age. Modulus of the nucleus and cortex were also approximated in the study.

Krag et al. (1997) studied the properties of 67 anterior lens and compared them to 25 posterior lenses in following work (Krag and Andreassen 2003). Rings at the center of each location were mounted between two pins and subjected to tensile stress at 0.05 mm/s stretch rate up to failure. The results of both studies showed that the thickness of the anterior lens increases with the age to a maximum of 75 years. The thickness of the anterior lens was three to five times larger than the posterior lens whose thickness is relatively constant with the age. Both stress-strain curves were nonlinear and the failure stress and strain, tangent modulus and elastic modulus at the failure decreased with the age significantly in the anterior lens. The elastic modulus of 0-10% strain of both lens increased up to 35 years old, which after it remained constant.

Pedrigi et al. (2007) investigated anterior mechanical properties of 12 anterior lenses out of which six had diabetes. The specimens were subjected to internal pressure periods of 0-5 mmHg/1-2 min up to 35 mmHg and the displacements were recorded using surface markers. A simple axisymmetric finite element model with constrained edges was used to extract the constants of Fung exponential model. The pressure-strain relationship had pseudoelastic nonlinearity with insignificant hysteresis. The two in-plane shears were almost zero and the diabetic lenses were stiffer than normal lenses. The two in-plane normal strains became equibiaxial toward the pole and the meridional was larger than the circumferential strain.

3.2 EYE FINITE ELEMENT MODELS

Finite element analysis has been widely used for modeling the eye for different purposes. Models ranged from specific tissues with appropriate boundary conditions to whole eye models and from simplified geometry and material properties to more complicated geometries and nonlinear properties. Whole eye models were used for stimulating trauma from different objects or explosion pressure and sclera models have been used for inverse finite analysis to extract the material properties and for analyzing its effect on the neighbor tissue. Models of the cornea have been widely used for modeling different refractive surgeries and tonometry measurements and the lens models are used mainly for studying the accommodation mechanism.

3.2.1 Whole eye models

For investigating the suspension of the eye in the orbit, Schutte et al. (2006) created a simple three-dimensional model of a spherical eye attached to the four rectus muscles (Figure 3.1). The mechanical properties of the eye ball and the orbital fat were assumed to be isotopic linear elastic, whereas the muscles were modeled as orthotropic linear elastic with linear thermal expansion coefficient. The model was constrained from translation at the posterior, and thin compliant elastic sphere was used in the model to stimulate the contact between muscles and fat. The contraction of the muscles was accomplished by applying a temperature change. The main finding from the eyes' vertical and horizontal movements was the importance of the fat in providing suspension and the stability of the muscle paths.

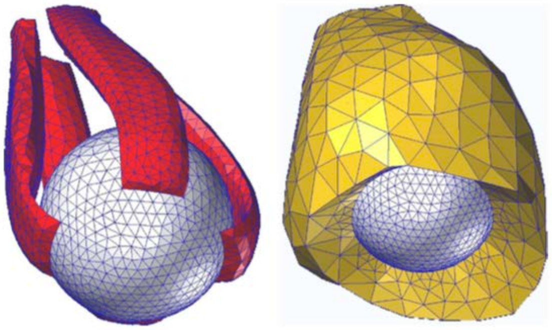

Figure 3.1 Eye ball model with the muscles (left) and fatty tissue (right) (Schutte et al. 2006).

Wang et al. (2007) used a half three-dimensional model similar to VTEM dynamic model (Stitzel et al. 2002) to analyze the effect of segmental sclera buckling surgery by varying different parameters such as: size of the eye, intraocular pressure, indentation of the buckle and its orientation and size (Figure 3.2). The solid tissues were modeled with two constant Moony Rivilin model and the humors using equation of state. The hyperelastic constants for the tissues were not well documented. The contact between the buckle and the sclera was modeled using penalty method and the indentation was achieved by applying tangent forces to the buckle edges at suturing points. The location and the type of the boundary condition for constraining the rotation at the posterior of the eye was not specified. The results showed that decreasing the overall buckle size and increasing the indentation will increase the von Mises stresses around the suturing points, whereas the intraocular pressure and buckle location from the eye equator have no significant effect on stress. The axial length of the eye increased up to certain indentation then it gradually decreased. The lens maintained its shape with little rotation; however, the cornea curvature rotated and its anterior surfaces was deformed. The total refractive error increased for high indentation for all pressure levels.

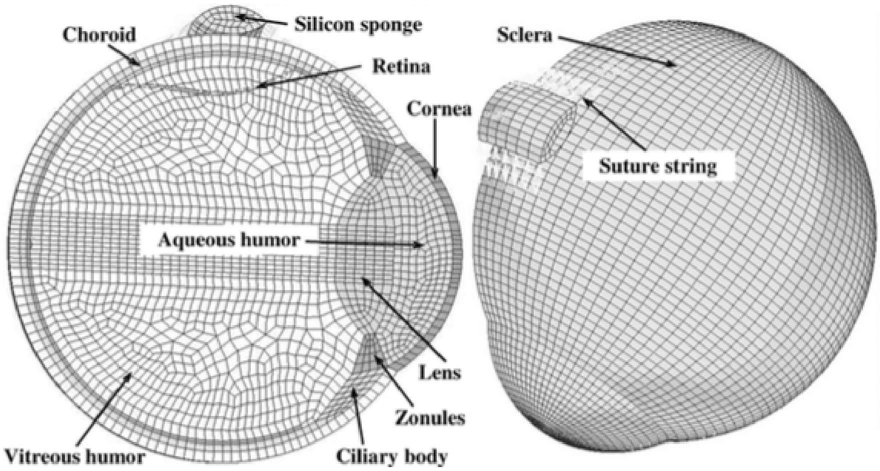

Figure 3.2 Finite element eye model with buckle and sutures location (Wang et al. 2007).

Aldhafeeri R. (2015) created an axisymmetric model of the eye where most of the tissue were included and modeled as linear elastic materials (Figure 3.3). The model is constrained at the middle of equatorial sclera from horizontal displacement and along the axis of symmetry. The fluids were assumed to be incompressible having same density of the water. Different thicknesses and indentations of a contacting encircling buckle, modelled as a rigid material, were used in addition to different cornea thicknesses. The results of axial length change and the von Misses stresses showed that increasing the encircling buckle width and indentation has more effect than reduction of the cornea thickness.

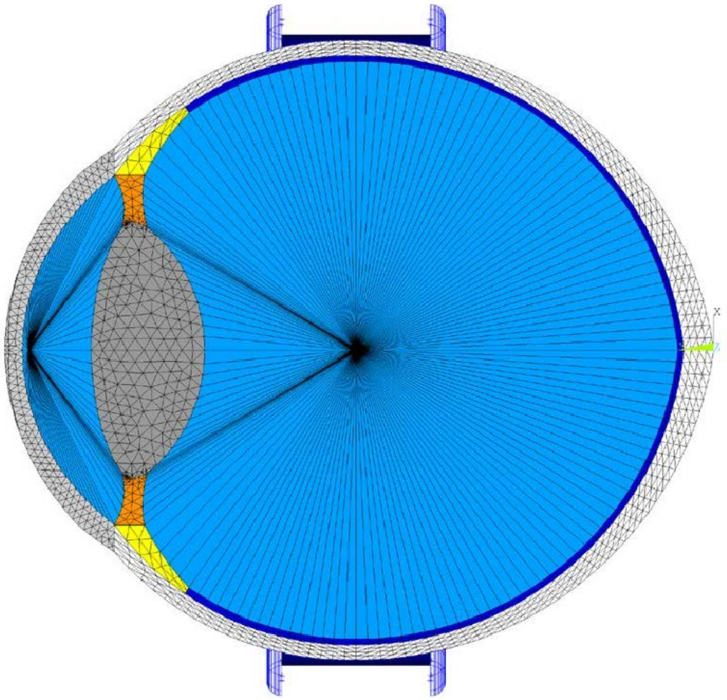

Figure 3.3 Axisymmetric finite element model (Aldhafeeri R. 2015).

3.2.2 Sclera models

For characterizing the mechanical behavior of the sclera, Girard et al. 2009a developed anisotropic hyperelastic constitutive model for the posterior sclera, which accounts for two families of fibers parallel to the sclera surface. Uniaxial test on eight-node hexagonal element constrained at bottom had excellent agreement with the analytical results as the fibers concentration in constitutive model changed. Also, changing the orientation of the fibers showed that circumferential fiber around the optic nerve head (0 degree) had a small effect on the expansion and twisting of the scleral canal and a large effect on its longitudinal displacement and on the posterior laminar deformation (Figure 3.4).

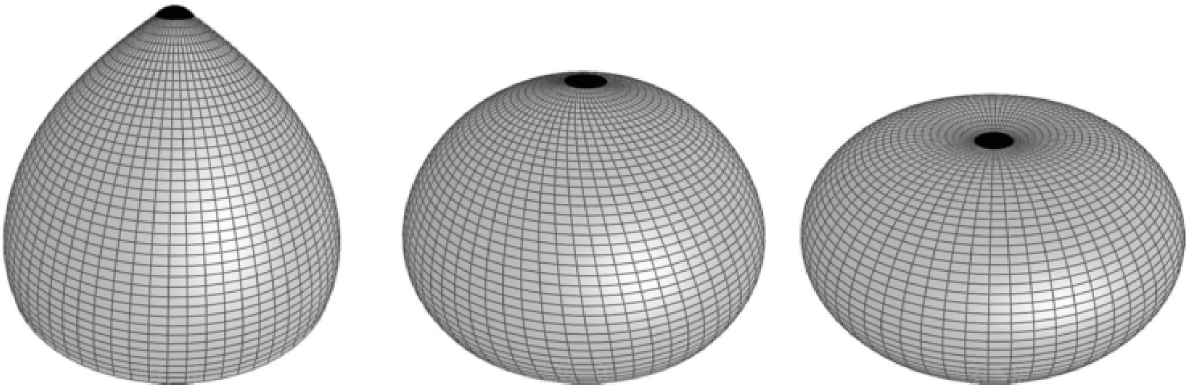

Figure 3.4 Sclera deformation for different fibers orientation 0, 45 and 90 degrees from left to right (Girard et al. 2009a).

In a following study (Girard et al. 2009b), experimentally inflated monkey eyes and an inverse finite element analysis was used with two models of the sclera posterior each divided into nine regions (Figure 3.5) to determine the 13 constants of the constitutive model: three elastic constants, two concentration factors for regions close and far from the optic nerve head and eight fiber orientations in each region. The sensitivity analysis showed that varying the bulk modulus from 0.1 to 1 GPa had less effect on the regions close to the optic nerve head, and changing the linear properties of the optic nerve head had influence on the parameters of the model. Finally, the extracted material parameters indicated that the concentration of the fibers is higher in the peripapillary sclera and there was an inverse relationship between tangent moduli and the thickness was observed. Also, the experimental displacements maps were in agreement with the model, where the nonlinearity highly dominated after 30 mmHg.

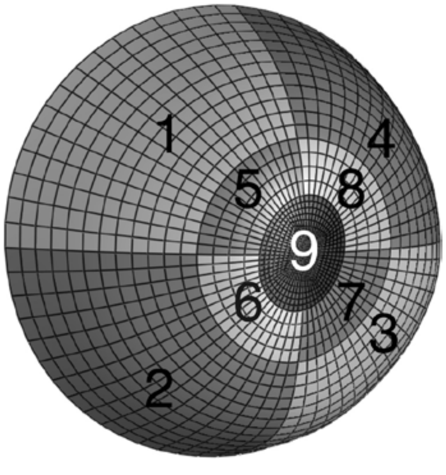

Figure 3.5 The postrior sclera divided into nine reigons (Girard 2009b).

Coudrillier et al. (2013) created anisotropic hyperelastic model of two inflated human sclera for extracting the parameters of the material model and characterizing the effect of fibers on mechanical response of the sclera and optic nerve head. The material model had the matrix represented by Neo-Hooken relationship and accounted for one family of fibers, where a probability density function was implemented in the anisotropic term of the strain energy function.

An X-ray mapping of the fibers showed that the fibers are more aligned in the peripethial than in the mid-posterior region. The experimental and finite element mapping of the strains had good agreement at 30 mm Hg with large local error. The degree of anisotropy was larger at the peripethial sclera by both X-ray and the model measurements, where the fibers in the circumferential direction were stiffer resulting in the heterogeneity of the sclera. Furthermore, simulation of the biaxial tests of Eilaghi et al. (2010) produced mechanical behavior falling in a range between most the compliant and the stiffest of the samples. They also showed that increasing isotropy degree parameter in the sclera will increase scleral canal expansion, maximum principle shear and tensile strains, and decrease lamina cribrosa deformation.

Grytz et al. (2014) conducted similar test to the previous one on nine pairs of the eyes aged from 20-90 years of human sclera for extracting collagen stiffness, shear modulus of the matrix and five parameters of a microstructure-based constitutive model: two for preferred orientation and collagen fibril concentration factor of the at meso-scale; and two defining the crimp fibril angle; and the ratio between its amplitude and cross section radius. The finite element model used for the inverse calculation was constrained by using spring supports through posterior sclera thickness with fixed edge, and extended mesh was used on the sclera surface for modeling the local anisotropy (Figure 3.6). The results showed that the three displacements maps of all eyes closely matched the experimental results and the average collagen orientation degree was obtained. In-plane strain was higher close to the optic nerve head region, collagen fibril strains were smallest than in and out of plane strains, and all strains became linear after a pressure of 20 mm Hg. The results of parametric study showed that varying shear modulus will have less effect on the circumferential strain, the elastic modulus had the most important effect on the meridional strain, and increasing fibril angle will increase the in-plane strain, whereas varying its geometry ratio will have less effect on the stiffness, and all regions of the sclera have the same dependence on the pressure.

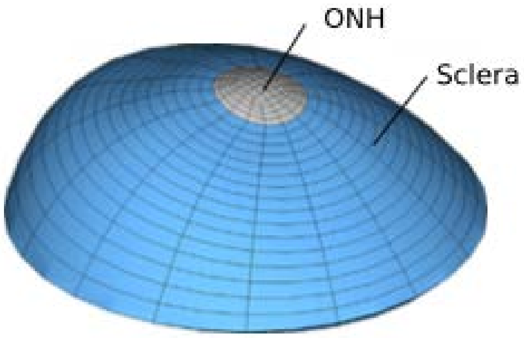

Figure 3.6 Posterior sclera model (Grytz et al. 2014).

3.2.3 Cornea models

Pinsky and Datye (1991) created first cornea finite element model based on the microstructure of the cornea for modeling the effect of radial keratotomy (RK) on the cornea. The lamella sheets were considered in-plane orthotropic linear elastic, where the variable is the orientation of the fibrils, and summation of all these sheets' rigidities represents the cornea rigidity. The finite element equations were obtained mathematically from the shell membrane constitutive relation by including geometrical nonlinearity with small strains and moderate rotation and considering one symmetric quadrant of the cornea fixed at the limbus with initial pressure of 2.135 kPa. The results of changing the number and depth of the incisions and optic zone diameter showed that the power change increases by increasing the depth and the latter had a large impact on the resultant power, where the largest change was for 90 to 95% depth for 8 and 16 incisions, respectively. The power change linearly increased with increasing the pressure, whereas increasing the optic zone decreased the diopters gradually at 3-4 mm zone (Figure 3.7). After using a spherical fit, the shape of the deformed cornea became more concave at the center as the number of the incision increased and their deformed profiles intersected at about 45-degrees from the cornea edge.

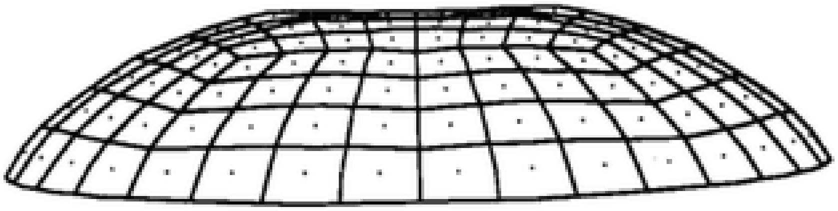

Figure 3.7 Deformed cornea model with 8 incisions and 95% depth (Pinsky and Datye 1991).

In a following study, Pinsky and Datye (1992) modeled astigmatic and hexagonal keratotomy using the same finite element model and compared all three surgeries to ex-vivo eye results in previous experiments (Salz et al. 1985, Lindquist et al. 1986, Gilbert et al. 1990). The difference between the total average power correction of the experimental and numerical results are about: 1.47, 1.08 and 0.36 diopters for radial, astigmatic and hexagonal keratotomy, respectively.

Bryant and McDonnell (1996) measured apical displacements of twelve human corneas resulting from the third cycle of pressurizing them up to 40 mm Hg. The material properties of linear isotropic, linear transversely isotropic, nonlinear isotropic and hyperplastic (Ogden’s model) models were approximated by an inverse finite element analysis of an axisymmetric cornea fixed at the limbus (Figure 3.8). Both linear models had similar plane tangent modules at 15 mmHg, where the pressure-displacement curves are almost the same. A nonlinear isotropic model with power function fitted the experimental results well, whereas Ogden's model had a poor fit. Furthermore, four radial keratotomy incisions at each principle meridian were stimulated by using all material models excluding Ogden's model. The resultant curvatures changes in diopters showed that the linear models had similar changes and the nonlinear model produced higher changes in addition to higher changes in the stiffness at the point posterior to the incision.

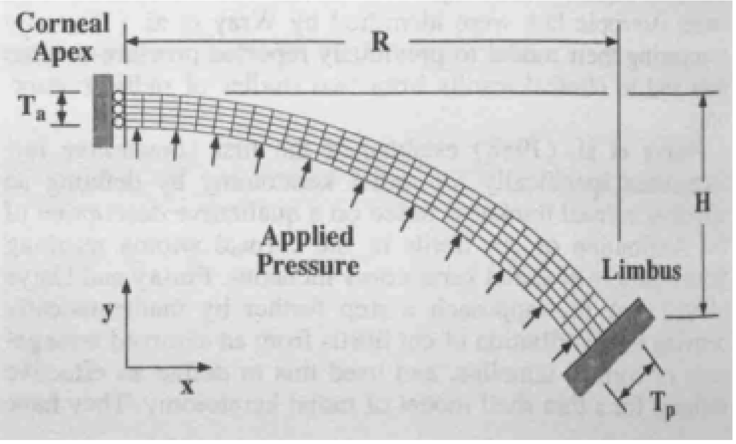

Figure 3.8 Axisymmetric model of the cornea (Bryant and McDonnell 1996).

Pinsky et al. (2005) developed an incompressible anisotropic hyperelastic constitutive model for a spherical stroma where the strain energy function of the lamella has four invariants and is weighted by probability density function based on X-ray diffraction imaging of the cornea. They used the finite element formulation of the model for stimulating the effect of a 7 mm tunnel scleral incision, 2 mm from the limbus with and without intraocular pressure. The results showed that the response of the model with the pressure caused astigmatism of 0.5-1 D which is close to the reported clinical results, while the model without the pressure had 1.5 D astigmatism.

For stress analysis of LASIK surgery, Fernandez et al. (2006) created an axisymmetric model of the cornea with translation-fixed and rotation free limbus and tangential free-translation at the center, where the anterior was meshed finer than the posterior cornea (Figure 3.9). The ablation lens within the cornea was modeled using gap elements and the material property of the cornea was assumed to be nearly incompressible nonlinear elastic (exponential model of Woo et al. 1972). The results showed that increasing removed segment's thickness will increase the plane stresses, and the anterior curvature of the cornea increased after 160 micrometers of segment's thickness, and the maximum curvature increase was located at peripheral cornea.

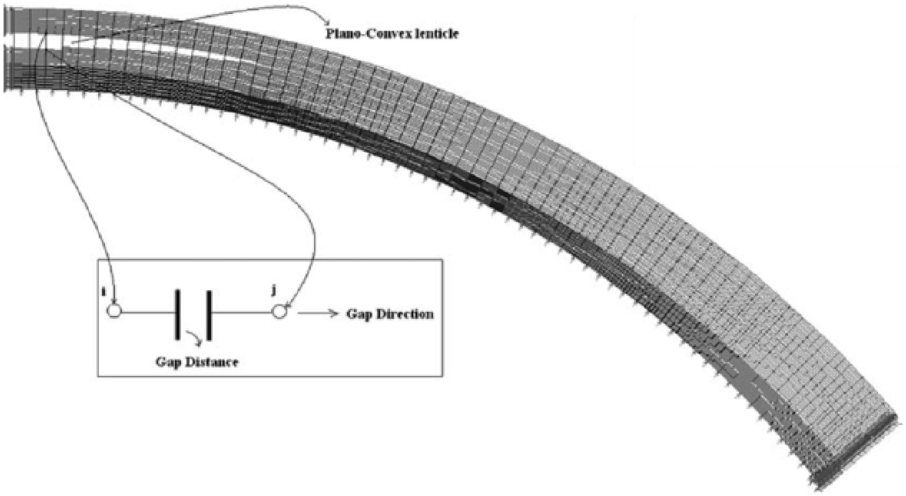

Figure 3.9 LASIK cornea model (Fernandez et al. 2006).

Elsheikh and Wang (2007) created a three-dimensional cornea model to study different parameters that may affect the results, namely, the mesh shape and refinement, boundary conditions, linear verses nonlinear material and thickness variation of the cornea in addition to obtaining correction factor for Goldman tonometry (Figure 3.10). The parametric results showed that increasing the rings which divide elements along a meridian on cornea beyond three rings and two layers along cornea thickness keeping the same number of elements will have insignificant accuracy on either intraocular pressure or concentric point load at the cornea center, and rollers spaced at 23˚ attached at the limbus will best match the results of the whole eye model. Furthermore, nonlinear material properties expressed by Ogden's model could represent the shape of nonlinear central cornea displacement due to pressure or point load more accurately than the linear material model. Considering cornea with different horizontal and vertical diameters had a negligible effect, and varying the cornea thickness had averaged of two models having constant thickness. Finally, cornea model was constructed based on the previous results that showed an error of 4% with experimental inflation of cornea. Then, Goldman tonometry was stimulated by a disk contacting the central cornea and the results used to obtain a correction factor of one.

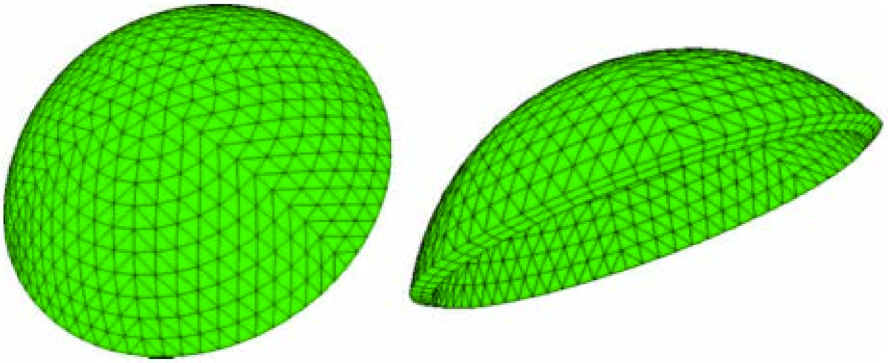

Figure 3.10 Two layer thick with six segments cornea model (Elsheikh and Wang 2007).

For modeling Photorefractive keratectomy (PRK) and limbal relaxing incisions (LRI), Alastrue et al. (2006) developed a nonlinear anisotropic, nearly incompressible hyperelastic model with two in-plane orthogonal fiber families. This general type of constitutive model was developed by Holzapfel and Gasser (2001) for arteries, and they adapted it for the cornea. Among linear elastic and Ogden's model, the proposed constitutive model fit the inflation test done by Bryant and McDonnell (1996), and negligible difference was obtained by including part of the sclera rather than fixed limbus boundary condition. For modeling the incisions, different material regions in the cornea were considered: zone without fiber stiffness representing the incision, zone with one family of fibers representing parallel areas to the cut; and the two fiber families zone for uncut fibers. Stress analysis for the healthy cornea was obtained and used later for computing the pressure change due to surgeries in an inverse method by applying the displacements resulting from surgeries. For the surgeries, ablation thicknesses were calculated using Munnerlyn's equation, depending on desired diopters correction, and the resultant curvature was calculated using least square spherical fit. Photorefractive keratectomy corrections of 2,4,6,8 and 10 D were made in optical zone of 6 mm-diameter resulted in a correction of 98.75 to 87.23 percent and a decrease in the pressure of 0.27 to 2.78 mmHg (Figure 3.11). Limbal relaxing incisions of 45, 60, 75, and 90 degrees of arcuate incisions will result in diopter errors of 3.6575 to 6.0618 D (Figure 3.12). Using the linear elastic and Ogden's model showed that the linear elastic model produced highest error in PRK, whereas Ogden's model will have maximum error in LRI, and the fibers model had the best results among all models.

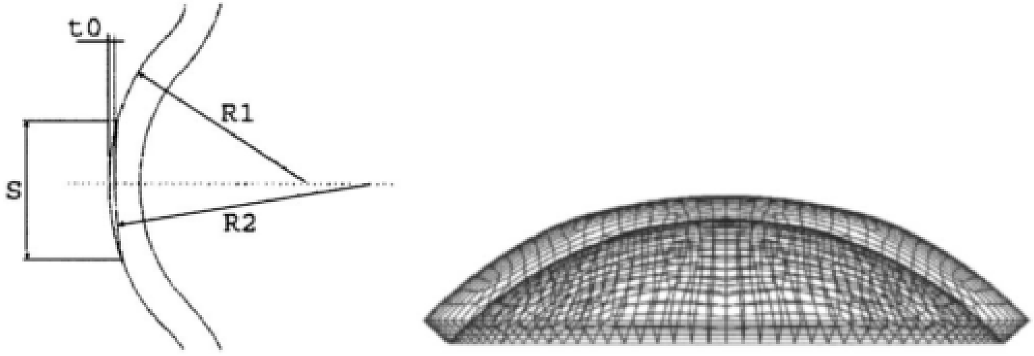

Figure 3.11 PRK model (right) and ablation profile (left) (Alastrue et al. 2005).

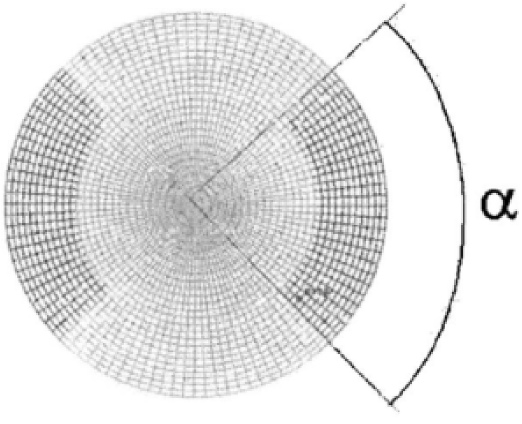

Figure 3.12 LRI model showing ablation angle (Alastrue et al. 2005).

Pandolfi and Maganiello (2006) used a similar formulation of Alastrue et al. (2006), used for the arteries, except that the volumetric strain energy function had a different form (Figure 3.13). The whole three-dimensional cornea model including the circumferential fibers at the edges was used to stimulate four uniaxial tests in literature and an inflation test on five samples by Bryant and McDonnell (1996). For the uniaxial tests, the model was fitted to all the results and its parameters were calculated in addition to Mooney-Rivlin constants using two tests. For the inflation test and using other parameters, the resultant curve was located between two out of five curves. Center keratocouns zones were defined in which fibers do not contribute to the stiffness zone, and the pressure-apical displacement showed that the healthy cornea had large stiffening compared to the diseased cornea.

In a following study, Pandolfi et. al (2008) used the model for studying two cases of myopic cornea, with and without astigmatism, by developing the biconic equation of the ablation profile. Quasi-static inflation of normal cornea and the two cases were done separately. The results of the von Mises stresses of both cases showed an increase of 20% to the normal cornea. Also, the dioptric power of the myopic cornea and the myopic cornea with astigmatism closely matched the normal cornea at normal intraocular pressure.

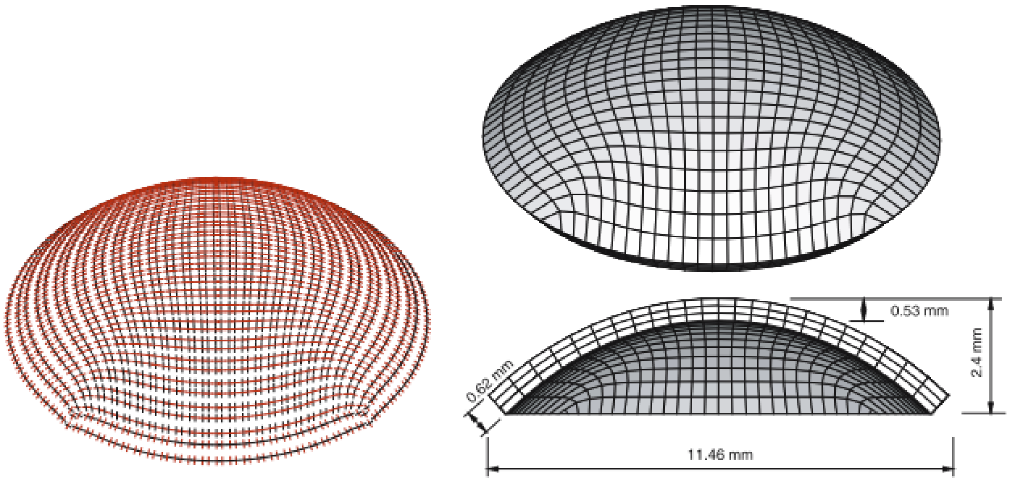

Figure 3.13 Cornea model: meshed (right) and fibers orientation (left) (Pandolfi and Maganiello 2006).

Lanchares et al. (2008) used the Pandlofi et al. (2006) model for modeling a three-dimensional cornea with planer symmetry, the limbus and a spherical sclera (Figure 3.14) with one and two 90% deep arcuate astigmatism correction incisions of 45, 60 and 90 degrees each with an optical zone of six and seven mm. The constants of the hyperelastic models were obtained from previous literature except for sclera where it was approximated. The model was constrained to only radial displacement in the middle of the sclera and outward translation in the center of the cornea. The optical power difference was measured within 1.5, 2, 2.5, 3 mm optical zone radii and produced different diopters. The results measured in a 3 mm optical zone of different incisions are very close to a referenced study used as a clinical guide for arcuate surgery. Furthermore, the stress analysis showed that the longer the incision the higher the von Mises stress, and based on larger principle stress results from one incision at 90 degrees compared to two incisions with 45 degrees, they recommend the latter, even though both clinically produce similar results.

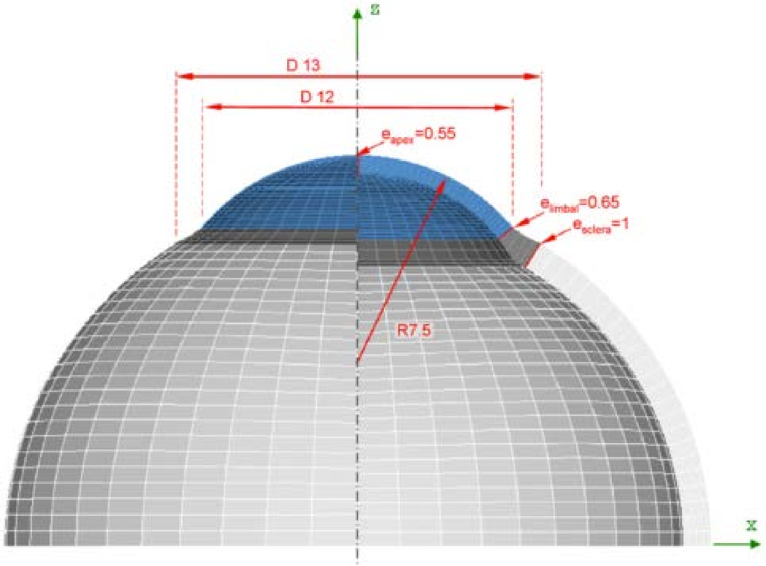

Figure 3.14 Symmetric eye model including cornea, limbus and sclera (Lanchares et al. 2008).

Studer et al. (2010, 2013) developed cornea model by obtaining constants of a similar constitutive model of Pinsky et al. (2005) in addition to uncrimping fibers effect using uniaxial and inflation tests done by Elsheikh et al. (2007). The proposed model fit all tests and the constants were obtained for two age groups in the experimental study. Next, they stimulated cornea, constrained at a portion of the sclera, for thirteen patient-specific cataract surgeries (Figure 3.15). The power changes matched most data of the patients at one month measured in in 3 mm optical zone with a device having an error of five micrometers.

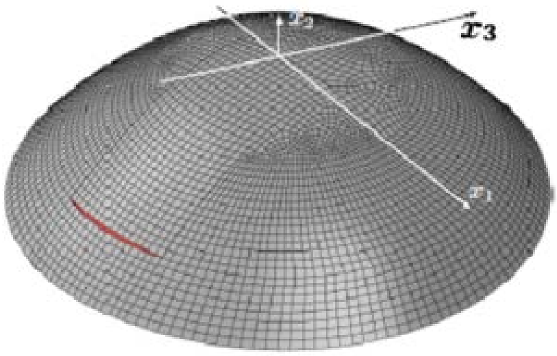

Figure 3.15 Meshed cornea model showing ablation area (Studer et al. 2013).

3.2.4 Lens models

Burd et al. (2002) created axisymmetric models of the lens system for 11, 29 and 45 year old lenses with their corresponding geometries and linear elastic constants. Each lens model contained the capsule with varying thickness, the cortex and the nucleus attached the three annular sheets of the zonulas fibers meshed with capsule using membrane element to the ciliary body at one point. An equation for ciliary body translation in relation to age was applied to each model representing the accommodation state. The results showed that all the lenses optical powers decreased as the displacement increased, where there was large reduction in the 29-year lens (Figure 3.16). The forces exerted by the zonulas increased with the displacement and the 45-year lens had the maximum increase. Sensitivity studies showed that a Poisson's ratio of 0.49 and nearly 0.5 had 3% difference in the diopters and increasing the stiffness ratio between the fibers will decrease the lens power.

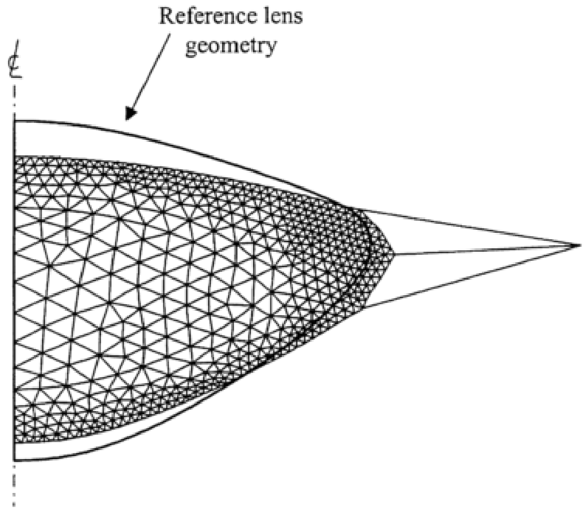

Figure 3.16 Deformed 29-year lens model (Burd et al. 2002).

Hermans et al. (2006) used a model similar to the 29-year lens model of Burd et al. (2002) with correction to the lens geometry and replacing the fiber attachment points by either one nodal force at center or at anterior and posterior or combination of both resulting in three models. An inverse finite element method was used to determine the net force needed for the accommodation amplitude in diopter and it was found to decrease linearly with the diopter. Stress analysis showed that the nuclear zone had minimum stresses and all the posterior regions of the models showed no change in curvature.

Ljubimova et al. (2008) utilized the axisymmetric model in the Burd et. al (2002) study in addition to a spherical vitreous body in an initial free stress configuration (Figure 3.17) within the fibers were oriented so that the lens is in contact with the vitreous. Displacements were applied on the body to introduce the cavity of the lens while keeping the posterior of the body displacement fixed. The results of the presence and absence of the middle fibers showed that less net force is required in the former model with force ratio of 3:1:2 for anterior, central and posterior fibers. A sensitivity study of the cortex and nucleus stiffness showed that increasing both stiffnesses will decrease the curvature changes as do the presence of the vitreous contact where the change in the lens central thickness is mainly driven by the changed nucleus stiffness which is consistent with reported measurements in the study.

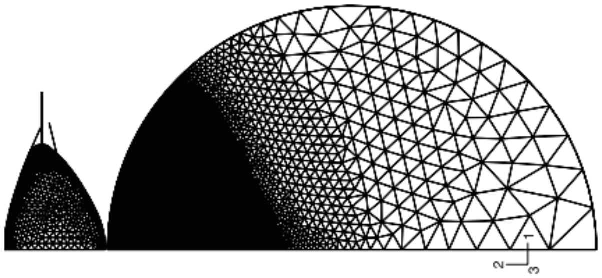

Figure 3.17 Stress free configuration of the lens and vitreous body (Ljubimova et al. 2008).

3.3 CLINICAL MEASUREMENTS OF SCLERAL BUCKLING EFFECTS

Many clinical studies have been conducted for evaluating the effects of the surgery on the eye since the early use of the scleral buckling. The evaluations of the patients were done preoperatively and postoperatively in weeks or months or even after years after the surgery. The refractive power change is either negative or positive diopter for flattening and steepening of the cornea, respectively. Different buckling procedures have been evaluated, for example, local buckling, segmental buckling and encircling buckling solely or combined with other buckling. The clinical studies have measured different parameters such as: axial length change, anterior length chamber, power and astigmatism of the cornea.

Burton et al. (1977) evaluated eighteen phakic and twelve aphakic (without lens) eyes after six weeks of encircling buckling. Overall measurements showed that 60% of the all eyes had an increase in their axial length and a decrease in the anterior chamber. For example, phakic eyes had average changes in the anterior chamber, lens thickness and vitreous cavity length of -0.19, +0.134 and +0.214 mm respectively.

Larsen et al. (1979) did ultrasonographic study five to eight weeks post surgery on ten patients subjected to 2 mm encircling buckle with a small local buckle. The study showed that the axial length increased by 0.98 mm and the average changes in the anterior chamber, lens thickness and vitreous cavity length of -0.02, 0.0 and +0.98 mm, respectively.

Goel et al. (1983) measured the astigmatic refractive error of three groups of patients: thirty-seven with radial buckle, twenty-six with encircling band and twenty with combination of both. Six month postoperative results showed that 69% of all eyes had error less than 2 diopters where more than the half of the first group had error more than 3 diopters. Also, the refractive error of eight patients with moderate to high indentation of the first group had not changed 3-5 years after the procedures.

Smiddy et al. (1989) evaluated seventy-five eyes three to six months after surgeries of radial, segmental or encircling alone or in its combination with the previous buckles. The evaluations showed that the astigmatism was 0.31 and 2.75 D and the axial length changes were 0.26 and 0.99 mm for non-encircled and encircled eyes, respectively.

Tanihara et al. (1993) measured in-vivo the axial length and cornea curvature of ninety-four eyes with segmental buckles and sixty-seven eyes with encircling buckles. After two weeks, the results showed that of 70% of the eyes with segmental buckles and 42% of the encircled eyes had shortening and 65% of segmental buckled eye and 75% of encircled eye had steepening in the cornea.

Wang et al. (1994) investigated the changes in twelve eyes with encircling band and thirty-two eyes with segmental buckle one week postoperatively. The axial length was elongated by 0.81 mm for encircling and shortened by 0.09 mm for segmental buckle. The anterior chamber depth and the lens thickness were decreased by 0.04 and 0.06 mm, respectively, while the vitreous chamber decreased by 0.05 mm. The astigmatism was 0.56 D for the segmental buckle.

Kinoshita et al. (1994) found that an encircling buckle increased the cornea power by an average of 0.01 D and decreased the astigmatism by 1.64 D. For a segmental buckle, the cornea power increased by 0.2 D and the increase in the astigmatism of one, two and three quadrant extent buckle was 0.88, 1.65 and 1.09 D, respectively.

Toyota et al. (1995) measured the axial length change of eighteen eyes with segmental buckles and twenty eyes having segmental with encircling buckling. The axial length increase was

0.6 mm for encircling with additional buckle and 0.04 mm for segmental buckle. The change in the eye power was -2.2 D for encircling and 0.01 D for segmental buckle.

Hayasshi et al. (1997) investigated the change in cornea shape due to: local buckling, encircling, encircling with vitrectomy and encircling with segmental buckle. The refractive change was 4.59, -1.7, -1.3 and -0.23 D, respectively. The surface asymmetry and differential maps of the cornea is shown in Figure 3.18 for each group.

Okada et al. (2000) examined the change in the topography of the cornea and the axial length of thirty-eight eyes in terms of range, distance and direction of the buckle (Figure 3.19). First group was subjected to segmental buckles and the second group had encircling with segmental buckles. The results are summarized as follow: 70.8% of the first group had an average decrease of 0.48 mm in their axial length, while 71.4% of the second group had elongation in their axial length of 0.47 mm. All deformed corneas showed steepening tendency towered the center of the buckles and closer the buckle was from the limbus larger was the absolute astigmatism of the cornea, whereas the range of the buckles has no significant effect on the axial length.

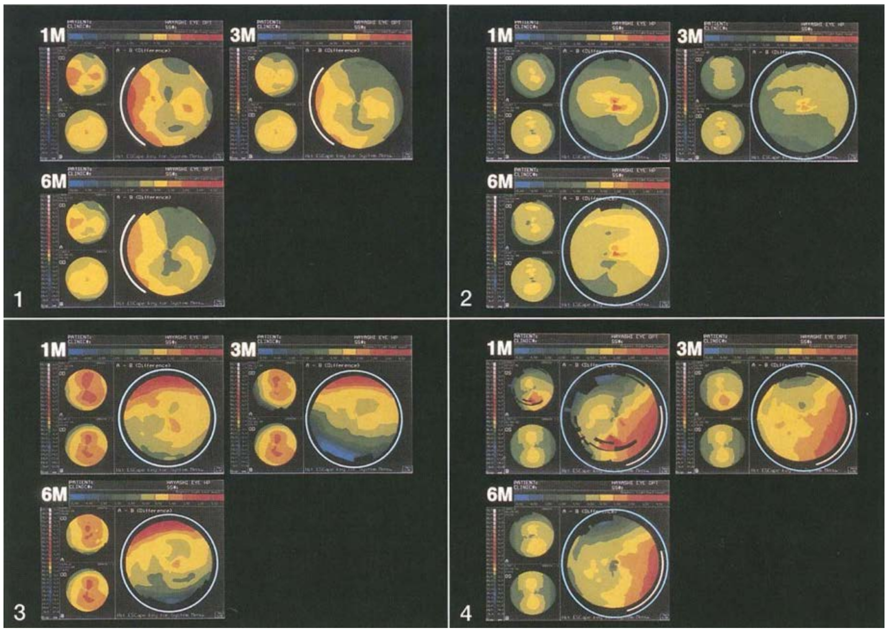

Figure 3.18 Maps of the corneas one, three and six months postoperative: (1) local, (2) encircling, (3) encircling with vitrectomy and (4) segmental with encircling. The white line around the cornea indicate the buckle orientation (increased bright color for steepening) (Hayasshi et al. 1997).

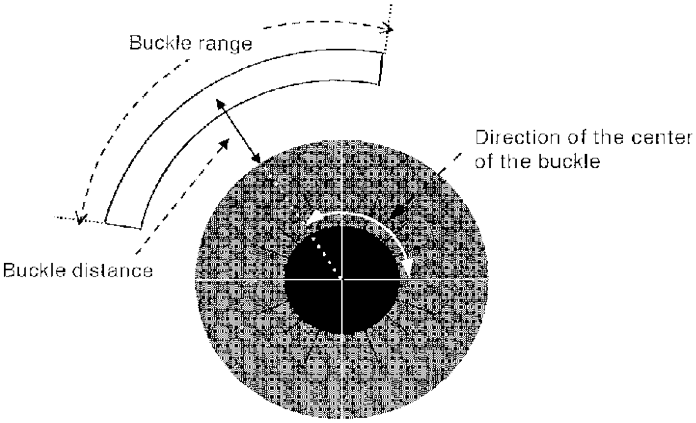

Figure 3.19 Buckle configurations (Okada et al. 2000).

Malukiewicz and Stafie (1999) evaluated the effect of segmental buckles with an encircling band on seventy-four patients with a large age range. The results for one month and one year post surgery were founded to be -0.22 and -0.43 D of flattening in the cornea curvature and 0.77 and 0.57 mm increase in the average axial length.

Weinberger et al. (1999) evaluated corneal topography of ten patients with an encircling buckle, eleven with a segmental and encircling buckle and four with a radial and encircling buckle. The curvatures of the corneas were evaluated as overall and in the central cornea. Twelve weeks results of the overall cornea showed that first group had no change. The second group had a 0.5 D steeping and the last group had a -0.3 D flattening, whereas at the central cornea no change was in the last two groups and the first had flattening about -1.1 to -1.6 D.

Domniz et al. (2000) found that a three months' evaluation of the cornea astigmatism after an encircling buckle had an increase of 0.11 D. Ornek et al. (2002) in similar study found that there is no difference between preoperative and six months' postoperative astigmatism.

Cetin et al. (2004) examined thirty-two eyes with one quadrant segmental with encircling band. The three months' results showed that the anterior chamber decreased by 0.204 mm, the cornea was flattened by an average of -1.1 D in the central zone and the quadrant corresponding to the segmental buckle exhibited more astigmatism.

Karimian et al. (2006) evaluated the diopters change of three encircled eye and thirty eye with segmental and encircling buckle. The results of three months postoperatively showed that the power of the cornea increased by 1.58 D in the first group and decreased by -0.07 D in the second group, whereas both had increase in the astigmatism of 0.36 D and 0.43 D, respectively.

Recently Tonghe C. (2014) investigated the effect of segmental scleral buckle without encircling on the depth of the anterior chamber and axial length of forty-nine eyes. After four months, the averages of the preoperative and postoperative axial length (from the back of the eye to the anterior lens) were 23.47 and 25.25 mm where the corresponding values for the anterior chamber depth were 3.2 and 2.97 mm. The increases in the intraocular pressure decreased to normal pressure one month after the surgeries. Figure 3.20 shows sample of the anterior chamber deformation.

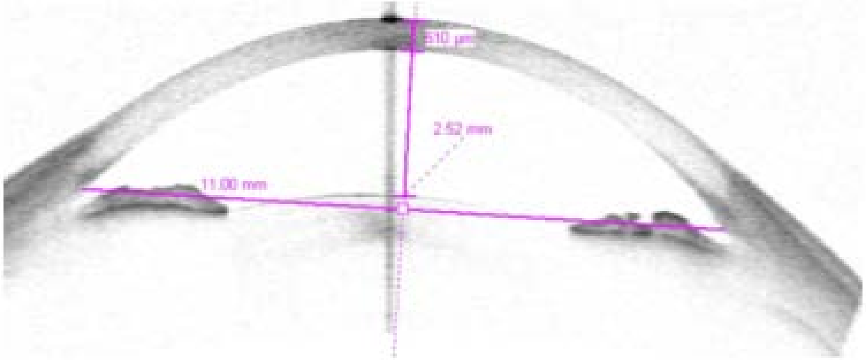

Figure 3.20 Deformed anterior chamber (Tonghe C. 2014).

In summary, the effects of scleral buckling have been an open question since the use of the scleral procedure. Most of the investigations of its effect were based on the evaluation of the patients' postoperative results using different tools. Different results have been found for changes in the eye dimensions and cornea refractive power in terms of the numerical results or conclusion as for the axial length change for segmental buckle. Also, most results have not been reported together for single investigation, for example, total refractive power change, astigmatism and axial length change. Although, some specifications have been improved like eyes criterions included in the study and proper time for evaluation, other rarely have been reported. Important parameters which should be addressed together for more accurate results are: location, range, distance from limbus and indentation of the buckle. Other could be accompanying the surgery such as: removal of the sub-fluid, amount and location of sutures and including other surgeries such as viteroctomy.

4.0 FINITE ELEMENT EYE MODEL DESCRIPTION

ANSYS 15.0 (ANSYS Inc., Canonsburg, PA) software was used in creating the geometry, meshing and running all the analyses. The steps of the analysis will be discussed in detailed: creating eye geometry, defining the material properties, meshing, applying load and boundary conditions.

4.1 GEOMETRY

The eye tissues have complex geometries where cornea and lens shapes are vital in determining the visual power of the eye. The tissues included in the model are sclera, cornea, lens, choroid, retina, ciliary body and zonular fibers. Detailed geometry of sclera, cornea and lens are included to eliminate any source of error and to increase the accuracy of the stimulation. The geometry of the eye is age and diseases dependent, for example, old aged eyes has longer axial length. The selected geometry was for normal eye with an average age of 55 years in age range where retinal detachment is commonly diagnosed.

Table 1 shows detailed dimensions of the eye with references. The thickness variation of the scleral is considered since it is the largest tissue, and choroid and retina were assumed to have uniform thicknesses. The retina was considered to have extension of 120˚ from the eye posterior (Atchison et al. 2016). Also, the lens and cornea detailed geometries are considered due to their significant in the optical power of the eye. The cornea was generated assuming its inner and outer surfaces are partial spheres. The optic nerve was not modeled and boundary conditions were applied to the posterior of the eye be used instead. The axial length (AL) is the normal distance from the anterior surface of the cornea to the surface of the retina and the anterior chamber length (ACL) is the distance from the cornea posterior surface to the anterior lens capsule. Figure 4.1 shows the locations of the dimensions of the eye.

Table 1 Geometry of the eye

Parameter	Dimension (mm)	Reference
posterior sclera thickness	1	Norman et. al 2011, Elsheikh et al. 2010a
equator sclera thickness	0.55	
anterior sclera thickness	0.8	
central cornea thickness (CCT)	0.54	Atchison et al. 2008, Prasad et al. 2011
cornea thickness at limbus	0.64	
center lens thickness	4.4	Atchison et al. 2008, Doyle et al. 2013
choroid thickness	0.2	Sigal et al. 2004
retina thickness	0.24	
cornea anterior radius	7.8	Atchison et al. 2008, Dubbelman et al. 2006
cornea posterior radius	6.5	
lens anterior radius	9.9	Atchison et al. 2008, Dubbelman, M., & van der Heijde, G. L. 2001
lens posterior radius	-6.9	
cornea outer dimeter at limbus	12.56	Pandlofi et al. 2008
cornea inner dimeter at limbus	12	
axial length (AL)	23.6	Atchison et al. 2008
anterior chamber depth (ACD)	2.75	Atchison et al. 2008, Bhardwaj et al. 2013
vitreous chamber length (VCL)	15.8	
vertical dimeter at equator	23	Atchison et al. 2008, Gilmartin et al. 2003

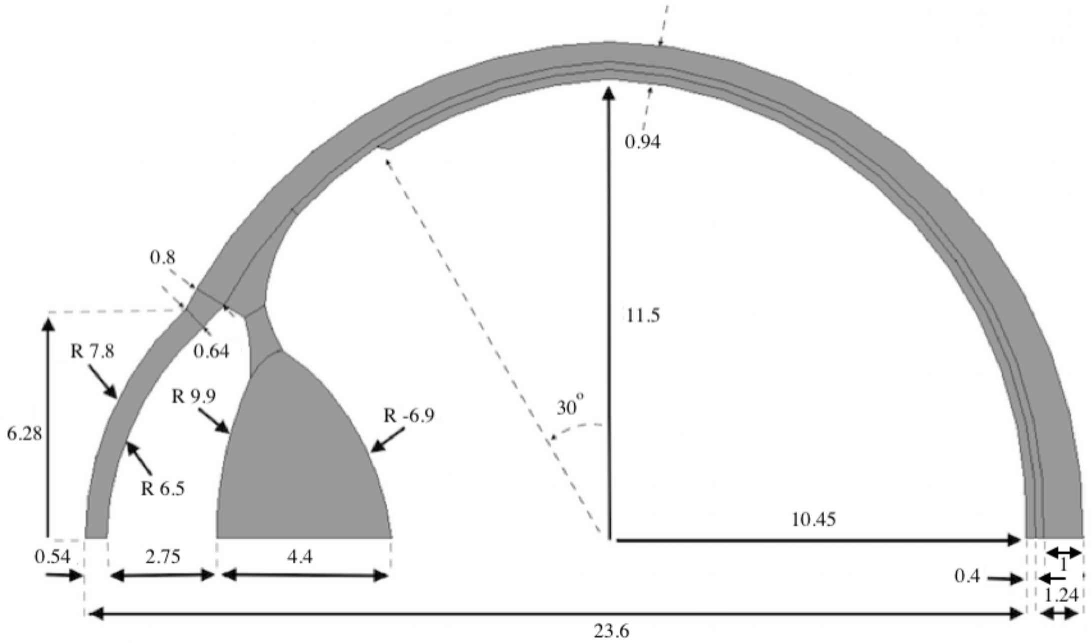

Figure 4.1 The structure and dimensions of the eye (all in mm).

One factor that can change the lens thickness and its curvatures and the anterior chamber length is the accommodation of the lens itself. However, the accommodation process was shown to be decrease to one diopter at an age of 40 years and to be lost at an age of 50 years (Atchison et al. 2008). Here, the accommodation is assumed to be absent that is all the lens dimensions are constants. Zonular fibers and the ciliary body shape were approximated close to their in vivo unaccommodated shape. The iris is a very thin and compliant part of the eye and therefore it was neglected from this study. The pupil diameter is important in determining the optical zone and the ablation diameter is where most of the light is transmitted to the eye. The optical zone and the ablation diameter were assumed to be 6 mm. For including thinned cornea, idealized thinned profiles can be generated using LASIK surgery of 25 and 50% reduced thickness. The anterior curvature is obtained for each reduced thickness from the Munnerlyn et al. (1988) formulations on relation between thinning by LASIK and the new anterior curvature of the cornea. The cornea reduced diopter (D) and ablation thickness (t) in an optical zone (S) and the profile is generated from the equation:

$$D = (n_c - 1)(1/R_2 - 1/R_1) \quad (4.1)$$

$$t \approx -S^2 D/8\,(n_c - 1) \quad (4.2)$$

where R_1 and R_2 are the anterior cornea radius of curvature before and after the thinning, respectively, and n_c is the refractive index of the cornea of 1.336. Using equation (4.2) and (4.1) for removed thickness of 0.135 and 0.27 mm (25% and 50% of the cornea original thickness) in ablation diameter of 6 mm will result in the altered radii of curvature of 10.2 and 14.4 mm, respectively. Figure 4.2 illustrates shapes of the 25 % and 50% thinned corneas (reduced thickness).

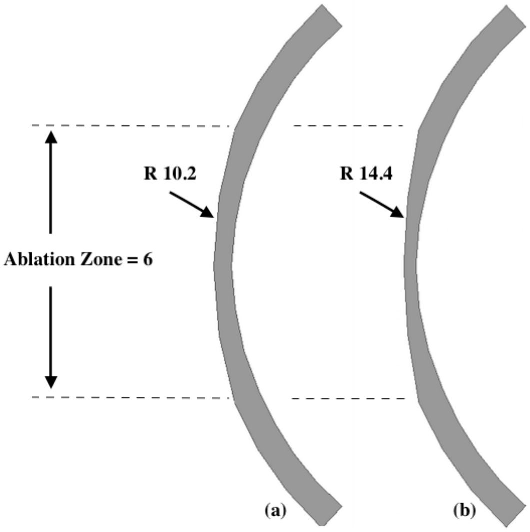

Figure 4.2 Thinned corneas: (a) 25%, (b) 50% (all in mm).

4.2 MATERIAL PROPERTIES AND MESHING

As with many biological tissues tissue, the material properties of the eye tissues are nonlinear, anisotropic with high incompressibility. The sclera, cornea and lens have been modeled as isotropic linear, isotropic and anisotropic hyperelastic materials. However, the nonlinear models have been based on more assumptions and simplifications under finite strains. In addition, the loading in the models were inflation or thinning of the solid material under constant pressure. Although some assumptions could help in constructing an advanced material model, the load of the scleral buckle is combination of tensile, compression and shearing which requires characterization of the materials for these stresses. Unfortunately, complete experimental characterizations of the materials in these forms are not available.

In this study, isotropic linear elastic models are used for all the tissues. The Young modulus and Poisson's ratio for each tissue are given in Table 2.

Table 2 Material properties of eye tissues.

Tissue	E (MPa)	V	Reference
Sclera	3	0.47	Friberg et al. 1988, Sigal et. al 2004
Choroid	0.88	0.49	Friberg et al. 1988
Retina	0.02	0.49	Jones et. al 1992
Cornea	1.5	0.42	Rossi et. al 2011, Uchio et. al 1999
Lens	6.88	0.49	Czygan and Hartung 1996
Zonular	0.35	0.4	Michael et. al 2012, Power et. al 2000
Ciliary Body	11	0.4	Power et. al 2000

The fluids are enclosed within solid structures and contain high percent of water of 98% and 99% for aqueous and vitreous humors (Dzierka and Jurczac 2015, Bishop 2000), respectively. The fluids will be modeled as hydrostatic incompressible fluids having density of water of 1000 kg/m^3. The encircling and the segmental buckle are made of solid silicone rubber with a Young modulus of 3.26 MPa and 0.47 Poisson ratio (Keeling et al. 2009).

To allow large variations in the geometry, the higher order elements of 8 nodes quadrilateral and 20 nodes hexahedron were used for meshing axisymmetric and three-dimensional model, respectively. Also, these elements have parabolic shape variation along edges which can produce higher accuracy at the cornea surface and to avoid distortion of element at the buckle indentation on the sclera surface. Although, the used material properties have a high Poisson ratio, however full rather than reduced integration method was used since there was no volumetric locking indication in the model.

For the three-dimensional model, revolved mesh having prism elements at the cornea apex and the eye posterior along the revolved axes was avoided since using such method will result in an underestimated displacement at the tip of the cornea (Elsheikh and Wang 2007). Lens, zonulas fibers and ciliary body were meshed using 10 nodes Tetrahedral for the lens in the three-dimensional model because of the geometric complexity.

Both fluids are contained within the solid tissues and modeled using the incompressible hydrostatic fluid element. This element is used for an enclosed compressible/incompressible hydrostatic fluid within a solid structure. The pressure node was positioned at the axisymmetric line and the symmetric plane of the axisymmetric and three-dimensional model, respectively. The final meshed model for axisymmetric and three-dimensional model are shown in Figure 4.3.

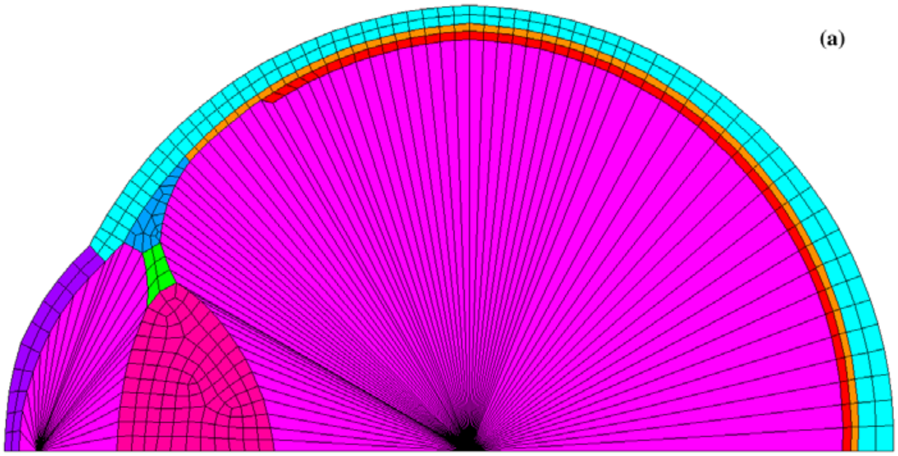

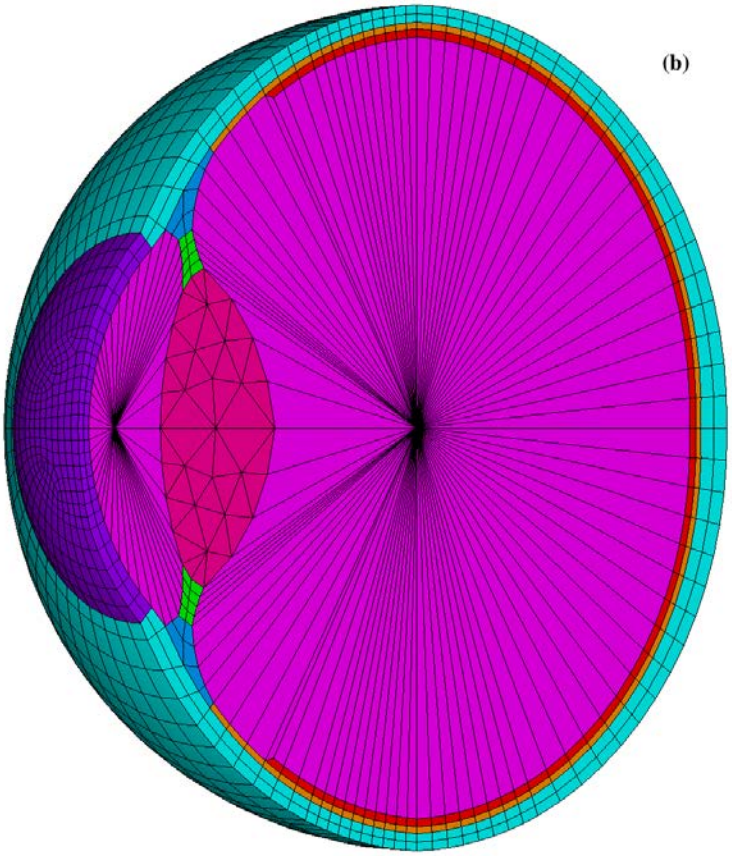

Figure 4.3 Meshed models of (a) axisymmetric, and (b) three-dimensional meshed model.

4.3 BOUNDARY CONDITIONS, LOADS AND INFLATED EYE

4.3.1 Boundary conditions

The eye globe is surrounding by fatty tissue, Tenon's capsule and attached to muscles. The fatty tissue are compliant materials and have complex distribution out of the capsule. The capsule is a thin body which covers the eyeball and removed before the procedure and reattached again after the buckling. The effect of the fatty tissue and the capsule are neglected from this study. Also, since muscles have to accommodate to different tension conditions and they are controllable by the surgeon, their effect was assumed to be negligible as with the eye models discussed previously. The optic nerve is inserted in the globe posterior with small opening of about 1.8 mm and its attachment has similar structure to the globe wall (Sigal et al. 2004). Instead of including its geometry in the model, appropriate boundary conditions replaced the nerve. In addition, enough boundary conditions are needed for constraining the model from rigid body motion.

For the axisymmetric model, to restrain the rigid body motion in the horizontal direction the node at the posterior eye is constrained from horizontal displacement. Three-dimensional model has a plane of symmetry which constrains some rigid body motions. This leaves rigid body motions in horizontal and vertical directions and a rotation around the axis of symmetry. The posterior node is prevented from both horizontal and vertical displacement and for constraining the rotation an additional node at the anterior of the posterior sclera has the vertical displacement constrained. In the surgery, before tightening a buckle, the buckle is fixed at the chosen position from the limbus by fixation sutures which provide constraint on the buckle from movement out of its position during and after tightening. For simulating this constraint, the horizontal displacement of middle of the buckle is coupled with same degree of freedom of node at position on the sclera.

4.3.2 Buckle tension

The buckle tension was applied in a static implicit analysis by assuming quasi-static state where the load is discretized and applied in sub-steps resulting in negligible inertia effect. Simulating the real configuration of the load is important for reliable results. The indentation of the encircled eye and model with the segmental buckle can be accomplished by the tightening of the encircling band in the surgery. For this purpose, frictionless contact analysis was use in the axisymmetric model between band and sclera and for the symmetric three-dimensional model between band-segmental buckle, upper sclera-segmental buckle, and lower sclera-band. The band was assumed to have an arbitrary thermal expansion coefficient along its circumference in both models of 1/13.5 ${C^0}^{-1}$. Applying a negative temperature difference in the band will cause a thermal contraction in circumferential length simulating tightening of the band.

4.3.2.1 Contact formulation

The contact analysis is highly nonlinear problem, where several parameters should be properly defined before running the analysis for obtaining more accurate results and increasing the convergence rate. The contact areas in the considered problem should be defined in terms of contact location, existence of gap and sliding.

For axisymmetric model, the contact is defied between the lines in the lower half of the band and lines at sclera surface where the buckling contact is likely to occur. For the segmental buckle with encircling band, three pairs of contacting surfaces are defined as shown in Figure 4.4. The predicted contact areas for the first pair are between the sclera surface and the extension of the segmental buckle bottom surface. The second contact pair are defined as the bottom surface of the encircling band and the grooved surface of the segmental buckle. The areas in third contact pair are defined for lower surface of the sclera with the bottom lower surface of the band.

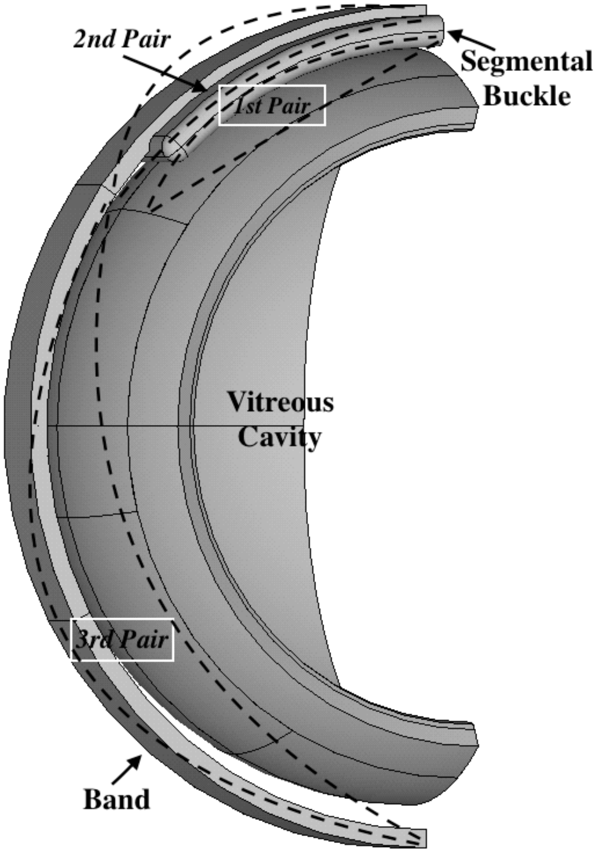

Figure 4.4 Contact pairs on half three-dimensional wall of vitreous cavity and buckles.

Each surface of a pair should be identified as target or contact surface, where the nodes on the contact elements (slaves) do not pass the target elements (master) in a contact pair. The target surface in a contact pair should be the part with the stiffer material, concave shape or with coarse mesh. Based on the previous factors, the target is defined as the upper sclera in the axisymmetric model. In the three-dimensional model, the target surfaces are the sclera surface in the first pair, the bottom of encircling band surface in the second pair, and the sclera surface in the third pair. The two-dimensional target/contact elements shape have the same shape of each brick element face, for example, it is quadrilateral element with 8 nodes on the surface of the sclera. The band is meshed with 4 nodes quadrilateral element in axisymmetric model and 8 nodes hexahedral element with the segmental buckle in the three-dimensional model.

There are three methods available for defining the contact in an implicit static analysis: the penalty, the augmented Lagrange and the multipoint constraint method. Here, all contact areas are surface to surface unbounded contact, where the first two methods are applicable. The first method calculates the normal forces as the multiplication of a stiffness contact coefficient and penetration distance (for example: spring is attached between two surfaces) resulting in sensitivity calculation with respect to the stiffness coefficient and the second method adds term to the calculation for reducing sensitivity to the defined stiffness coefficient. In buckle contact, the latter method can cause convergence difficulties and more iterations to convergence. Here, the penalty method is used where the contact stiffness factor was defined several times until the calculated coefficient before the analysis fell in range between the modulus of elasticity of the paired bodies for axisymmetric and the three-dimensional model for obtaining a converge solution.

The contact behavior can be defined as: bonded, no separation, rough, frictionless and frictional contact. The bonded and frictional contact can cause tangential stresses. In both models, the contact is defined as frictionless and for all the contact pairs in the three-dimensional model.

4.3.3 Pre-buckled inflated eye

To stimulate the vivo eye before the buckle application, the eye should be inflated to introduce the physiological pressure in addition to the residual stresses and strains. Including the inflation step as first step before application of buckle can produce many sources of error, for example, it can disrupt the contacts causing initial penetration and contact forces. Also, most of reported eye dimensions in literature, for example in Table1, are extracted from in vivo measurements, inflating this geometry can misrepresent the original geometry, stresses and strains. To overcome these effects, the pressurization of humors was done in a sequence step.

A simple iteration method, similar to the work done by Elsheikh et al. 2013, is adopted here to produce the approximate shape of the eye, pressure, stresses and strains:

1- A pressure is applied to both fluids in the in-vivo geometric model without the buckle.
2- The resultant displacements for the main dimensions of the eye (Table 1) are subtracted from in-vivo geometry producing new geometry. This new geometry is now used in step 1.
3- The loop between step 1 and 2 is repeated until the reported percentile difference in the geometries from the defined values is less than 0.01%.

The previous analysis was done for axisymmetric model and two iterations were required untill the maximum resultant error was 0.01% in the posterior retina thickness. The resultant geometry, from the axisymmetric model, was then used for the three-dimensional model where it was inflated and then the initial pressure, stresses and strains are exported for use in the model with buckle. Figure 4.5 shows the von Mises stress disruption for inflation of the axisymmetric and three-dimensional models where the maximum is at the limbus in both models. The stresses are imported as residual stresses with the pressure as initial pressure. In the finite element programme, the stresses of the inflation are assigned as residual values where the total stress is:

$$\sigma_{total} = \sigma_{buckling} + \sigma_{residual} \quad (4.3)$$

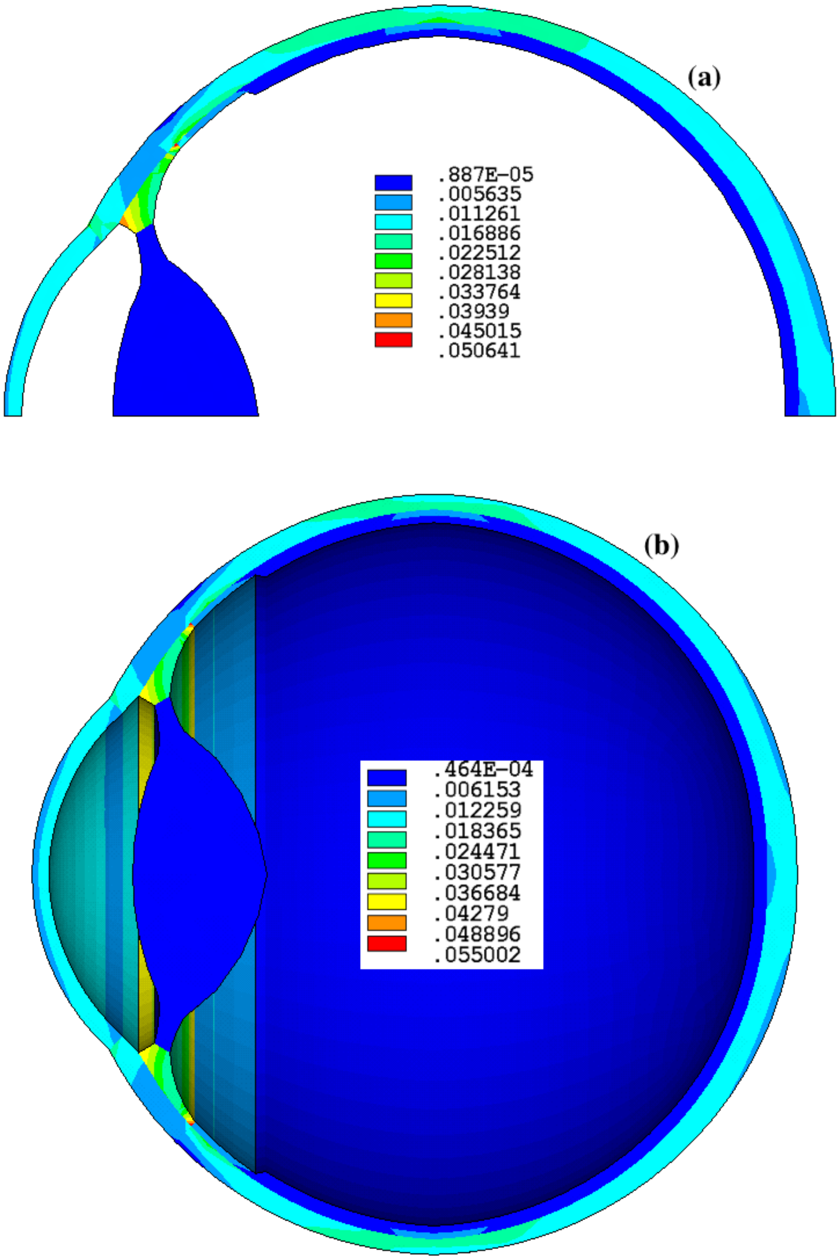

Figure 4.5 von Mises stress distribution by inflation in the (a) axisymmetric and (b) three-dimensional model.

5.0 BUCKLING EXPERIMENT AND MODEL ASSESSMENT

5.1 EXPERIMENTAL SCLERAL BUCKLING

In this part of study, an experimental of the deformation of the eye in terms of change in the axial length and the tilting of corneas by buckling with additional segmental buckle having different extents and widths. This is done using a porcine eye and by laser scanning of the eye before and after the buckling.

There is a lack of experimental results of the scleral buckling in the literature as related to geometric measurements. One reported experimental eye deformation measurement study was based on digital image correlation (DIC) for eye inflation deformation (Coudrillier et al. 2012), which measures strains. Here, a laser scanning measurement device (Faroarm, Faro Inc.) was used to measure the geometry of the buckled eyes.

Eight porcine eye samples kept in an insulated box filled with ice were acquired from a local butcher and the experiments were conducted within 12 hours of harvest. The eyes prepared by removing all surrounding tissues (muscles, fat and Tenon's capsule) leaving the globe and partial optic nerve. The scanning tissues can be challenging since the tissue can have specular reflection, multiple scattering underneath the surface or light emission in transparent tissue. The cornea did not show up in the scan since it was reported not to reflect light due to its high transparency to red laser wavelength (Mrochen M., Seiler T. 2003). For this purpose, the surface of the cornea was coated with graphite powder which is previously tested for sclera in the DIC experiment and had no effect on its mechanical properties (Coudrillier et al. 2012).

Before the scanning, all the eyes were inflated with intraocular pressure to simulate the in vivo physiological pressure using simple water column pressure setup commonly used in medical eye experiments. The intraocular pressure was introduced by a hydrostatic pressure of water column of 20.4 cm analogous to 15 mmHg through needle in the partial optic nerve (Figure 5.1). Water fluid was injected in the eye using a syringe connected to the system where the eye axial axis is kept approximately parallel to the zero scale in the column.

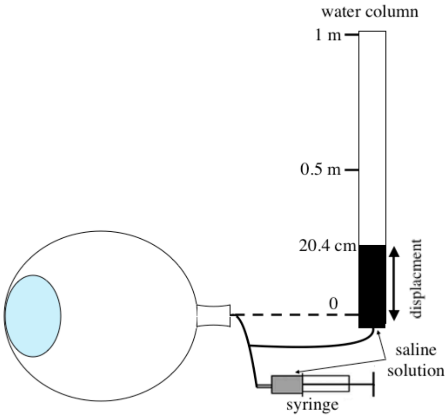

Figure 5.1 Eye pressure setup.

The inflated eyes were positioned on a stand to provide resistance to gravity and remove any undo constraints. Four of the eyes had inserted weightless shortened needles with betaine end as targets for measuring the tilting of the cornea due to buckling. Two of the targets were placed at the edge of the cornea approximately along the axis that is normal to buckle and one target was placed at the posterior of the eye as a reference point where all targets formed a triangle. Segmental buckles were prepared from silicone rubber of widths 5 and 7 mm each with 90° and 180° extents, and each was used in eyes with and without the targets with 2.5 mm wide silicone band for encircle buckling at the equator of the eye. After firm attachment of the band and the buckle, the band was shortened 3 mm. All eyes were scanned before and after buckling. Figure 5.2 shows an eye with the targets mounted on the clay and an eye initial scanned with a sketched triangle connecting all targets.

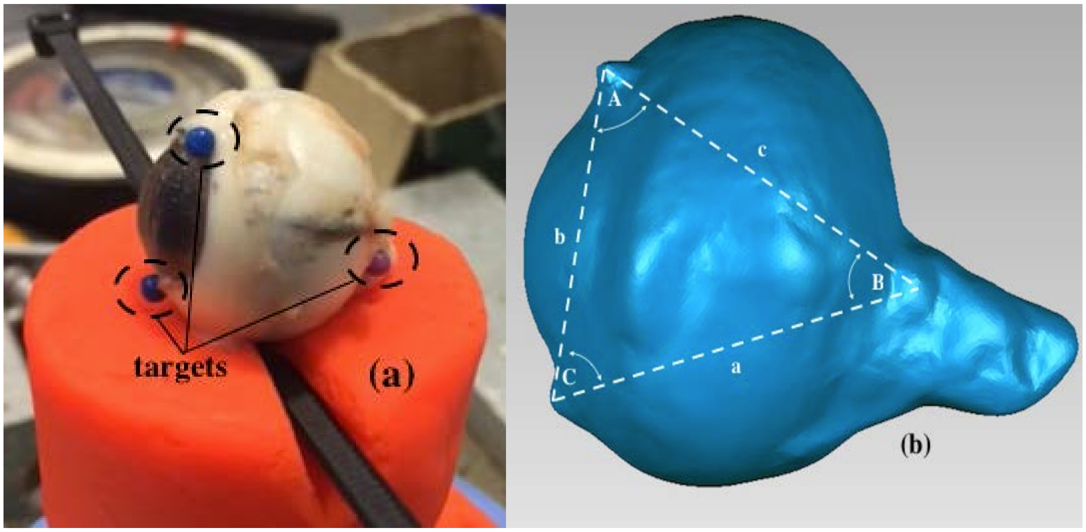

Figure 5.2 (a) eye with applied targets, (b) scanned eye with projected triangle.

After the scanning and measuring of the vectors magnitudes in the triangle, the angle C (cornea angle) can be calculated using law of cosines:

$$C = \cos^{-1}\left[\frac{\|a\|^2 + \|b\|^2 - \|c\|^2}{2\|a\|\|b\|}\right] \quad (5.0)$$

Figure 5.3-4 shows the scans for the eyes before and after buckling for the eyes with and without targets, respectively.

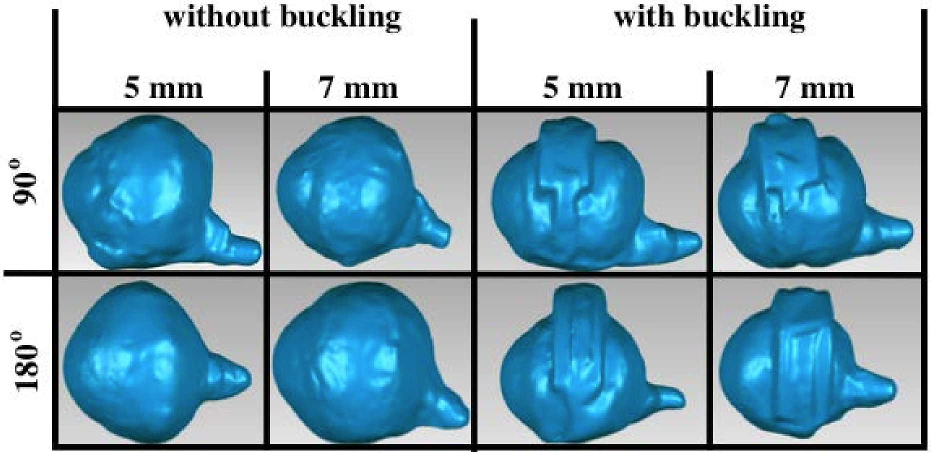

Figure 5.3 Scanned eyes without targets with 5 and 7 mm wide buckle and 90° and 180° extent before and after buckling.

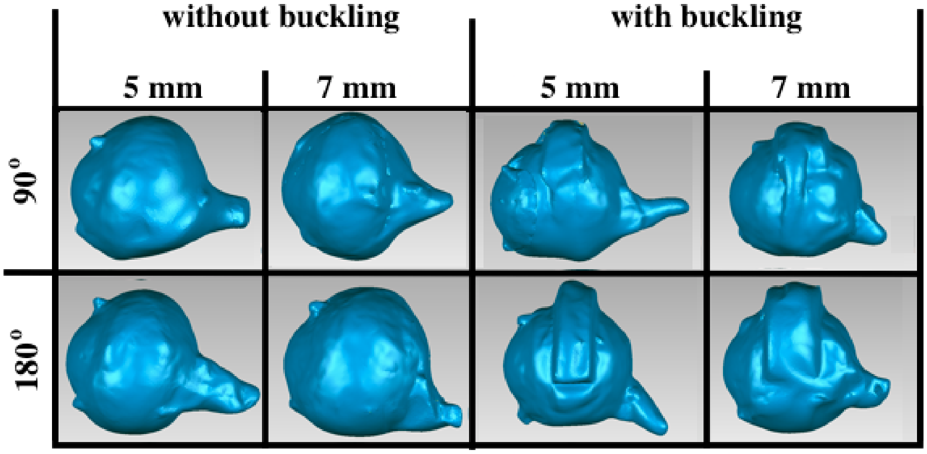

Figure 5.4 Scanned eyes with targets with 5 and 7 mm wide buckle and 90° and 180° extent before and after buckling.

The axial length was as an average of two eyes with same buckle where the eye posterior thickness was included in the axial length measurements. Figure 5.5 gives the axial length and the cornea angle for pre-buckled and buckled eyes.

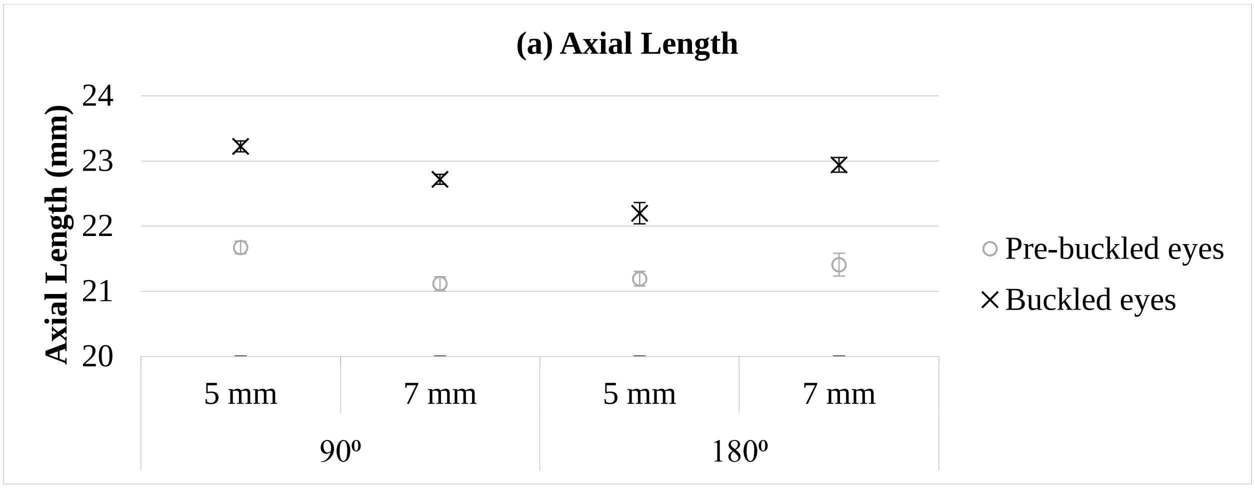

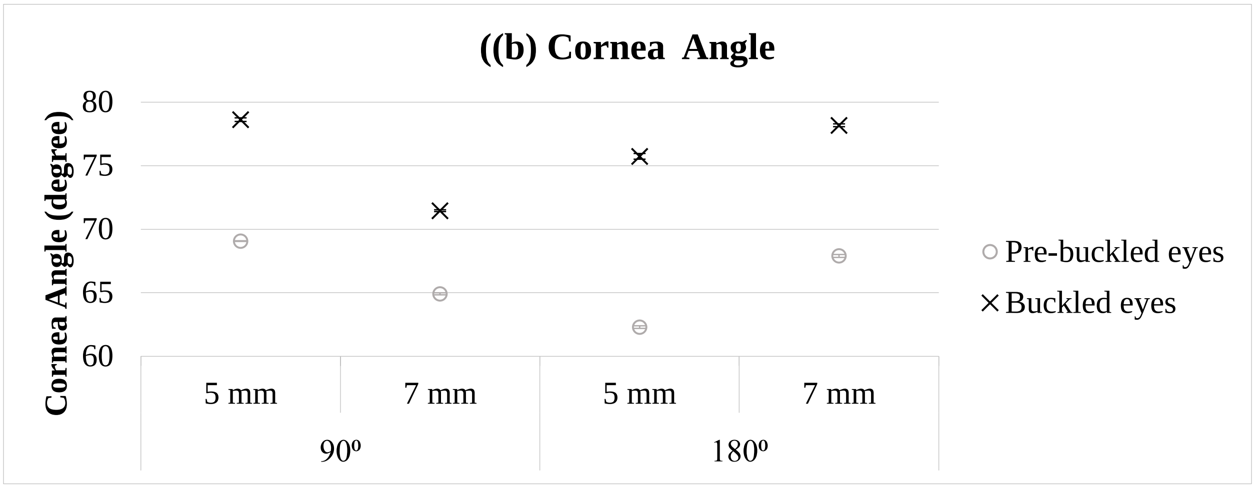

Figure 5.5 (a) axial length percent change for all eyes, (b) cornea tilt in four eyes (bars for standard errors of CAD measurements within each scan)

In summery the eyes had an increase in their axial length where it is similar increase for all eyes and the average axial length of pre-buckled eyes (21.35 ± 0.26 mm) was increased by buckling (22.77 ± 0.24 mm) and the average cornea Buckling caused pre-buckled cornea angle (66.05°± 0.89°) away from the center of the buckling (76°± 1.55°). Results of different widths and extents showed no significant deviation from each other.

5.2 SENSITIVITY ANALYSIS

5.2.1 Load sequence in static analysis

The pressure and the volume in the eye can be affected by buckling. In successful surgery for retinal reattachment, the physiological pressure should return to its original value. This can be done by surgical intervening, for example, removal of sub-retinal fluid before high buckling or within vitrectomy surgery after buckling. Also, the eye can return to its normal pressure by the physiological regulation of the aqueous humor (Williams and Aaberg 2006, Brinton et al. 2009). In this part of analysis, the differences between different sequences of applying buckles and removal of additional fluid were evaluated by a static analysis.

Keeling and Propst (2009) formulated a mathematical model of the buckled spherical eye where the eye can undergo different stages of loads. As shown in figure 5.6, buckling the eye can increase the pressure during the surgery and then the pressure is reduced to its original state by removing some of the eye volume. The band external pressure for changing the eye shape is added to the fluid pressure with no change in the fluid volume.

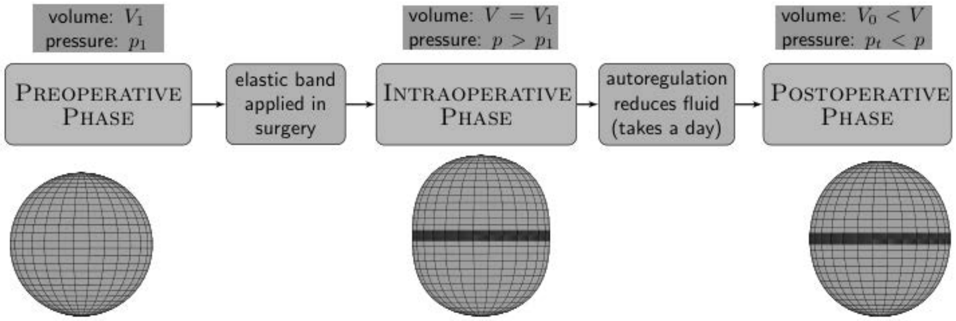

Figure 5.6 Schematic sequence of buckling load (Keeling and Propst 2009).

In this analysis, different simulation sequences are examined within static analysis where the postoperative phase results retention of the physiological pressure of 2 kPa for three indentation of 0.5,1 and 1.5 mm. The first model used the sequences illustrated in Figure 5.6 for separated indentations analysis where it resulted in three models for three indentations (two load steps/model). Figure 5.7 illustrates the paths of additional models with different load sequences where the second model represent stabilization of the pressure (P_i) after each indentation (T_i) steps and the third model has the pressure is fixed before buckling. For the three indentations, the second and third model both resulted in one model for all the three indentations; and six and three load steps per model, respectively. In this model, the fluid element expanded its volume to accomplished the prescribed pressure.

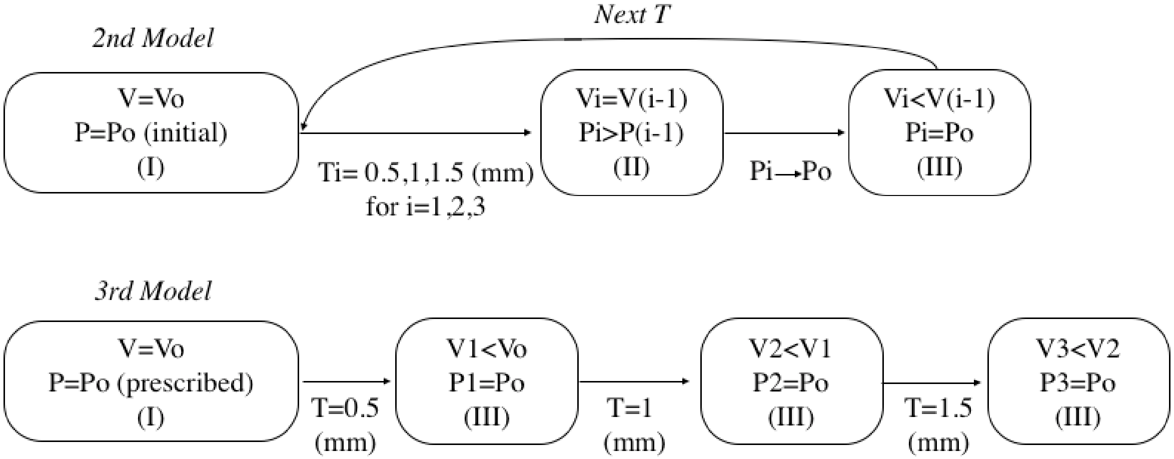

Figure 5.7 Schematic path of 2nd and 3rd model (I, II and III for preoperative, intraoperative and postoperative phase).

Table 3 lists the percent change in the axial length (%) and the maximum von Mises stress (kPa) for the models at different indentations. The results of all models are numerically very close where the errors can be resulted from different iteration paths in the nonlinear analysis.

Table 3 Postoperative results for the models with different load sequence.

Indentation	0.5 mm		1 mm		1.5 mm	
Model	AL (%)	S_{max} (kPa)	AL (%)	S_{max} (kPa)	AL (%)	S_{max} (kPa)
1	1.312	179.828	2.251	338.657	2.7	519.019
2	1.312	179.828	2.25	338.655	2.7	519.001
3	1.312	179.828	2.251	338.654	2.7	518.996

In the summary, models with different buckling load sequences have similar results within static analysis. For simulating large number of models, the third sequence can be used since it is computationally less expensive and since the targeted results are postoperative results.

5.2.2 Analytical solution of transverse isotropic pressurized spherical shell

For including a transverse isotropic sclera in sensitivity analysis (section 5.2.3), an analytical solution is in need for validating the numerical solution of the code and since the transversely isotopic model is defined in the general orthotropic model in ANSYS. Formulation of the solution will be carried out since there is no similar problem was found in literature.

In this formulation, we consider a transverse isotropic elastic spherical pressure vessel, where the properties are symmetric around the radial axis, with internal and external radius of a, b and applied internal pressure of p_i. Here an exact solution is derived for this problem. Starting with stating the required equations:

If e_{33} *is* the material symmetry axis, Hook's law expressing the principle stresses in terms of the principle strains for transverse isotropic medium (Bower, A.F. 2009) is given as:

$$\begin{aligned} S_{11} &= C_{11}\varepsilon_{11} + C_{12}\varepsilon_{22} + C_{13}\varepsilon_{33} \quad \text{(a)} \\ S_{22} &= C_{12}\varepsilon_{11} + C_{11}\varepsilon_{22} + C_{13}\varepsilon_{33} \quad \text{(b)} \\ S_{33} &= C_{13}\varepsilon_{11} + C_{13}\varepsilon_{22} + C_{33}\varepsilon_{33} \quad \text{(c)} \end{aligned} \tag{5.1}$$

if directions e_{11}, e_{22}, e_{33} are analogues to $e_{\theta\theta}, e_{\emptyset\emptyset}, e_{\rho\rho}$ directions in spherical coordinates, by expressing (5.1) equations in spherical coordinates and rearranging, where $e_{\rho\rho}$ became the axis of material symmetry, we get:

$$\begin{aligned} S_{\rho\rho} &= C_{33}\varepsilon_{\rho\rho} + C_{13}\varepsilon_{\theta\theta} + C_{13}\varepsilon_{\emptyset\emptyset} \quad \text{(a)} \\ S_{\theta\theta} &= C_{13}\varepsilon_{\rho\rho} + C_{11}\varepsilon_{\theta\theta} + C_{12}\varepsilon_{\emptyset\emptyset} \quad \text{(b)} \\ S_{\emptyset\emptyset} &= C_{13}\varepsilon_{\rho\rho} + C_{12}\varepsilon_{\theta\theta} + C_{11}\varepsilon_{\emptyset\emptyset} \quad \text{(c)} \end{aligned} \tag{5.2}$$

if we expressed the elastic constants of the transverse isotropic sphere by:

$E_{\theta\theta} = E_{\emptyset\emptyset} = E_p$; $E_{\rho\rho} = E_t$;

$v_{\theta\emptyset} = v_{\emptyset\theta} = v_p$; $v_{\rho\theta} = v_{\rho\emptyset} = v_{tp}$; $v_{\theta\rho} = v_{\emptyset\rho} = v_{pt}$

where the sub-notations p and t are for plane and transverse direction, respectively.

The stiffness constants are given by:

$$C_{11} = C_{22} = E_p(1 - v_{pt}v_{tp})\Upsilon, \quad C_{33} = E_t(1 - v_p{}^2)\Upsilon, \quad C_{12} = E_p(v_p - v_{pt}v_{tp})\Upsilon$$

$$C_{13} = C_{23} = E_p(v_{tp} + v_p v_{tp}), \quad \Upsilon = E_t(v_{pt} + v_p v_{pt})\Upsilon, \quad C_{44} = \mu_t, \quad C_{66} = \mu_p$$

$$v_{tp}/E_t = v_{pt}/E_p, \ \mu_p = E_p/2(1 + v_p), \quad \Upsilon = 1/(1 - v_p{}^2 - 2v_{pt}v_{tp} - 2v_p v_{pt} v_{tp}) \tag{5.3}$$

The stress equilibrium equations in spherical coordinates are given as:

$$\frac{\partial S_{\rho\rho}}{\partial \rho}+\frac{1}{\rho}\frac{\partial S_{\rho\theta}}{\partial \theta}+\frac{1}{\rho \sin\theta}\frac{\partial S_{\rho\emptyset}}{\partial \emptyset}+\frac{1}{\rho}\left(2S_{\rho\rho}-S_{\theta\theta}-S_{\emptyset\emptyset}+S_{\rho\theta}\cot\theta\right)+f_{\rho}=\varrho\ddot{u}_{\rho} \qquad (a)$$

$$\frac{\partial S_{\theta\rho}}{\partial \rho}+\frac{1}{\rho}\frac{\partial S_{\theta\theta}}{\partial \theta}+\frac{1}{\rho \sin\theta}\frac{\partial S_{\theta\emptyset}}{\partial \emptyset}+\frac{1}{\rho}\left((S_{\theta\theta}-S_{\emptyset\emptyset})\cot\theta+3S_{\theta\rho}\right)+f_{\theta}=\varrho\ddot{u}_{\theta} \qquad (b)$$

$$\frac{\partial S_{\emptyset\rho}}{\partial \rho}+\frac{1}{\rho}\frac{\partial S_{\emptyset\theta}}{\partial \theta}+\frac{1}{\rho \sin\theta}\frac{\partial S_{\emptyset\emptyset}}{\partial \emptyset}+\frac{1}{\rho}\left(2\,S_{\emptyset\theta}\cot\theta+3S_{\emptyset\rho}\right)+f_{\emptyset}=\varrho\ddot{u}_{\emptyset} \qquad (c) \qquad (5.4)$$

where $f_i, \ddot{u}_i$ are the body forces and the accelerations, respectively.

The strain-displacement relations in spherical coordinates are given as:

$$\varepsilon_{\rho\rho}=\frac{\partial u_{\rho}}{\partial \rho} \qquad (a)$$

$$\varepsilon_{\theta\theta}=\frac{1}{\rho}\left(\frac{\partial u_{\theta}}{\partial \theta}+u_{\rho}\right) \qquad (b)$$

$$\varepsilon_{\emptyset\emptyset}=\frac{1}{\rho\sin\theta}\left(\frac{\partial u_{\emptyset}}{\partial \emptyset}+u_{\rho}\sin\theta+u_{\theta}\cos\theta\right) \qquad (c)$$

$$\varepsilon_{\rho\theta}=\frac{1}{2}\left(\frac{1}{\rho}\frac{\partial u_{\rho}}{\partial \theta}+\frac{\partial u_{\theta}}{\partial \rho}-\frac{u_{\theta}}{\rho}\right) \qquad (d)$$

$$\varepsilon_{\theta\emptyset}=\frac{1}{2\rho}\left(\frac{1}{\sin\theta}\frac{\partial u_{\theta}}{\partial \emptyset}+\frac{\partial u_{\emptyset}}{\partial \theta}-u_{\emptyset}\cot\theta\right) \qquad (e)$$

$$\varepsilon_{\emptyset\rho}=\frac{1}{2}\left(\frac{1}{\rho\sin\theta}\frac{\partial u_{\rho}}{\partial \emptyset}+\frac{\partial u_{\emptyset}}{\partial \rho}-\frac{u_{\emptyset}}{\rho}\right) \qquad (f) \qquad (5.5)$$

After stating the required equations, the boundary conditions in this problem are traction boundary conditions of $t(a)=p_i e_{\rho}$, $t(b)=-p_o e_{\rho}$, where $p_o=0$; by substituting each in the following equation:

$$S.n=t$$

we get the boundary conditions as:

$$S_{\rho\rho}=-p_i\,, \qquad S_{\rho\theta}=S_{\rho\emptyset}=0 \quad at\ \rho=a$$

$$S_{\rho\rho}=0, \qquad S_{\rho\theta}=S_{\rho\emptyset}=0 \quad at\ \rho=b$$

By assuming linearized elasticity of the problem, the solution will be derived using “The semi-inverse method” (Slaughter, W.S. 2002). In this method, an educated prediction for the solution is made and then the derived solution must satisfy equations of elasticity and the boundary conditions. In this problem, the assumption is that the displacement field has the spherical symmetry of the problem that is the displacement field is only function of the radius:

$$u_\rho = U(\rho) \qquad u_\theta = u_\emptyset = 0$$

by substituting the displacements in the strain-displacement equations (5.4), we get the strains as follows:

$$e_{\rho\rho} = U'(\rho), \qquad e_{\theta\theta} = e_{\emptyset\emptyset} = \frac{U(\rho)}{\rho}, \qquad e_{\rho\theta} = e_{\theta\emptyset} = e_{\emptyset\rho} = 0,$$

and then by substituting the strains in the stress-strain relations given in (5.2), we get the stresses as:

$$S_{\rho\rho} = C_{33}U'(\rho) + 2C_{13}\frac{U(\rho)}{\rho}$$

$$S_{\theta\theta} = S_{\emptyset\emptyset} = C_{13}U'(\rho) + (C_{11} + C_{12})\frac{U(\rho)}{\rho} \qquad , S_{\rho\theta} = S_{\rho\emptyset} = S_{\theta\emptyset} = 0$$

by substituting the stresses in the equilibrium equations (5.4) and assumes the problem is static and there are no internal body forces that is $f_i = \ddot{u}_i = 0$, the second and the third equations are satisfied and we get from the first equation the following differential equation:

$$C_{33}U'' + 2C_{13}\left(\frac{U'}{\rho} - \frac{U}{\rho^2}\right) + \frac{1}{\rho}\left(2C_{33}U' + 4C_{13}\frac{U}{\rho} - 2C_{13}U' - 2(C_{11} + C_{12})\frac{U}{\rho}\right) = 0$$

which is reduced to:

$$C_{33}U'' + 2C_{33}\frac{U'}{\rho} + 2(C_{13} - C_{11} - C_{12})\frac{U}{\rho^2} = 0$$

This is a second differential equation has Cauchy-Euler equation form and can be solved using Euler method by assuming the solution has a form of $U = \rho^n$ and subtitutite it in

$$C_{33}n(n-1)\rho^{n-2} + 2C_{33}n\rho^{n-2} + 2(C_{13} - C_{11} - C_{12})\rho^{n-2} = 0, \quad \text{dividing by } \rho^{n-2}$$

$$C_{33}n^2 + C_{33}n + 2(C_{13} - C_{11} - C_{12}) = 0, \quad \text{solving for } n$$

$$n_{1,2} = \frac{-C_{33} \pm \sqrt{{C_{33}}^2 - 8C_{33}(C_{13} - C_{11} - C_{12})}}{2C_{33}}$$

and the general solution of the displacement field and the stresses becomes as:

$$U = A\rho^{n_1} + B\rho^{n_2}$$

$$S_{\rho\rho} = (n_1C_{33} + 2C_{13})A\rho^{(n_1-1)} + (n_2C_{33} + 2C_{13})B\rho^{(n_2-1)}$$

$$S_{\theta\theta} = S_{\emptyset\emptyset} = (n_1C_{33} + (C_{11} + C_{12}))A\rho^{(n_1-1)} + (n_2C_{33} + (C_{11} + C_{12}))B\rho^{(n_2-1)}$$

A, B are constants and can be found by applying the boundary conditions as follow:

$$0 = (n_1C_{33} + 2C_{13})A\, {r_0}^{(n_1-1)} + (n_2C_{33} + 2C_{13})B\, {r_0}^{(n_2-1)} \quad \text{, writing } A \text{ in terms of } B$$

$$A = -\frac{(n_2C_{33} + 2C_{13})}{(n_1C_{33} + 2C_{13})} B\, {r_0}^{(n_2-n_1)}$$

$$p_i = (n_1C_{33} + 2C_{13})A\, {r_i}^{(n_1-1)} + (n_2C_{33} + 2C_{13})B\, {r_i}^{(n_2-1)}, \text{ substituting A}$$

$$p_i = -(n_2C_{33} + 2C_{13})\, B\, {r_0}^{(n_2-n_1)}\, {r_i}^{(n_1-1)} + (n_2C_{33} + 2C_{13})B\, {r_i}^{(n_2-1)}$$

solving for the constants we get:

$$B = \frac{p_i\ {r_i}^{(1-n_1)}}{(n_2C_{33} + 2C_{13})({r_0}^{(n_2-n_1)} - {r_i}^{(n_2-n_1)})}\ ;\ A = -\frac{p_i\ {r_i}^{(1-n_1)}\ {r_0}^{(n_2-n_1)}}{(n_1C_{33} + 2C_{13})({r_0}^{(n_2-n_1)} - {r_i}^{(n_2-n_1)})}$$

By substituting the constants in the general form of the displacement and stresses equations with rearranging we get the solution:

$$U = \frac{p_i\ {r_i}^{(1-n_1)}}{({r_0}^{(n_2-n_1)} - {r_i}^{(n_2-n_1)})}\left(\frac{1}{(n_2C_{33} + 2C_{13})}\ \rho^{n_2} - \frac{{r_0}^{(n_2-n_1)}}{(n_1C_{33} + 2C_{13})}\rho^{n_1}\right)$$

$$S_{\rho\rho} = \frac{p_i \ r_i^{(1-n_1)}}{(r_0{}^{(n_2-n_1)} - r_i{}^{(n_2-n_1)})}\left(\rho^{(n_2-1)} - r_0{}^{(n_2-n_1)}\rho^{(n_1-1)}\right)$$

$$S_{\theta\theta} = S_{\emptyset\emptyset} = \frac{p_i \ r_i^{(1-n_1)}}{(r_0{}^{(n_2-n_1)} - r_i{}^{(n_2-n_1)})}\left(\frac{(n_2C_{33} + (C_{11} + C_{12}))}{(n_2C_{33} + 2C_{13})}\rho^{(n_2-1)} - \frac{r_0{}^{(n_2-n_1)}(n_1C_{33} + (C_{11} + C_{12}))}{(n_1C_{33} + 2C_{13})}\rho^{(n_1-1)}\right)$$

Since the equations satisfy the boundary conditions, this is the solution to the problem. These equations hold for linear transverse isotropic sphere where linear isotropic sphere become a special case here. Since this problem is more general than isotropic pressurized sphere, the common stresses and displacement equations for isotropic pressurized sphere can be derived by substituting $C_{11} = C_{33}$, and $C_{12} = C_{13}$ in the solution resulting in $n_1 = 1$ and $n_2 = -2$ (Slaughter, W.S. 2002).

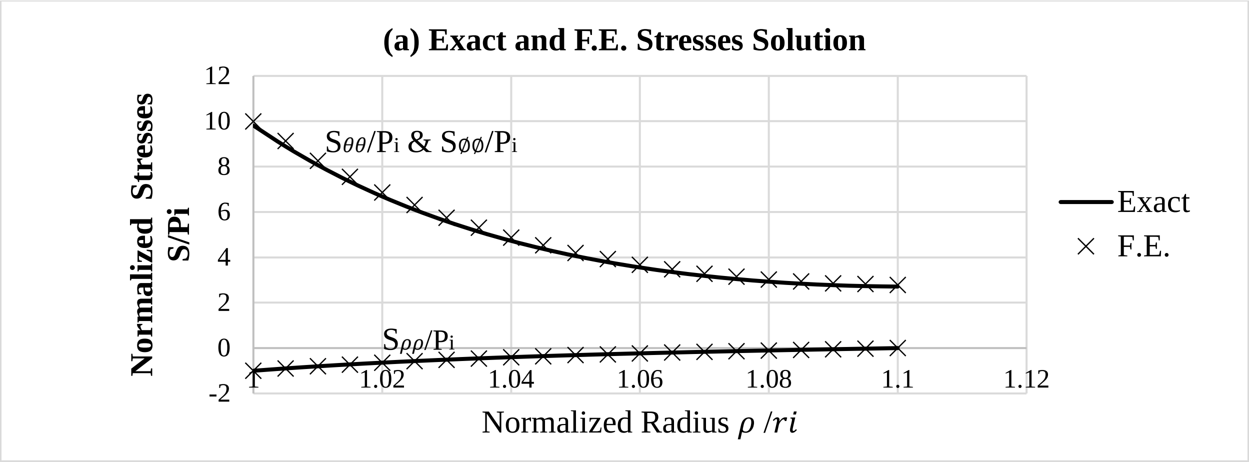

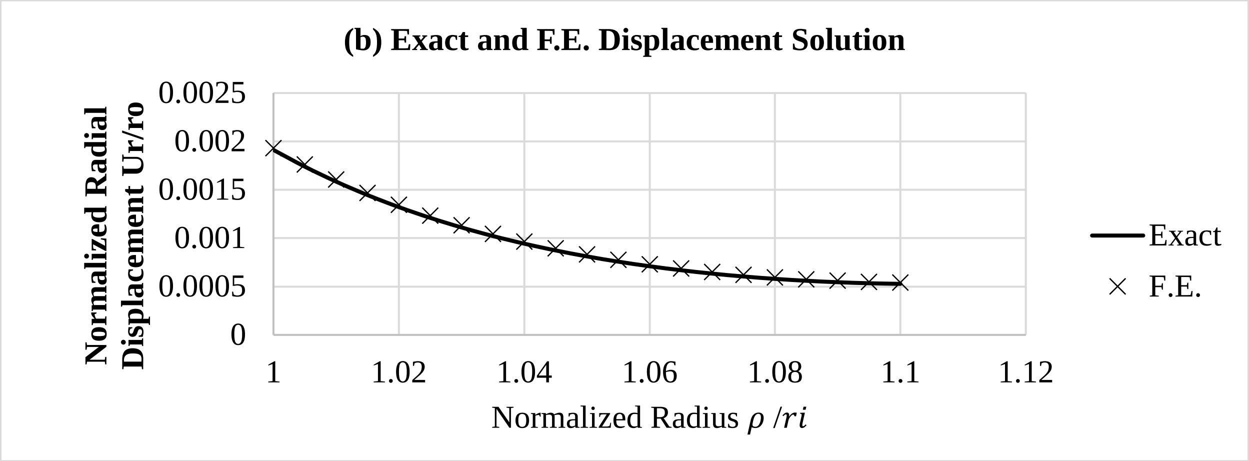

Figure 5.8 The normalized analytical and numerical solutions of: (a) stresses (P_i is the initial pressure); and (b) displacement ($\mathbf{r_i}$ and $\mathbf{r_o}$ are the inner and outer radius, respectively).

For validation of the transverse isotropic sphere in the finite element analysis, the materials constants in Table 5 in section 5.2.3 as an example are assumed for axisymmetric model of 1 mm thick sphere with inner diameter of 10 mm constrained at top center from horizontal displacement with mesh density of 20 by 300 elements (along thickness and circumferential directions). The displacement and stresses are compared to the derived exact solution for the assumed constants in Figure 5.8 where both the exact and the numerical solutions had good match.

5.2.3 Elastic constants of the sclera and cornea

In this part of study, analysis was carried out for buckling an eye with different elastic moduli of sclera and cornea, since they are the major tissues in the eye, and the sclera as an isotopic and transverse isotropic linear elastic body. The axisymmetric model is used for the analysis with a 2.5 x 0.6 mm band.

For isotropic models, the elastic modulus of the sclera was taken as 5.5 MPa (Woo et al. 1977), and was reported for cornea as 1.5 MPa (Richoz et al. 2014). Three different variations in the properties were investigated as given by Table 4. The sclera was kept more rigid than the cornea in varying the elastic modulus while their Poisson's ratio and eye tissues material properties kept constant as reported in Table1.

Table 4 Models with different modulus of elasticity of sclera and cornea.

Model	E of Sclera (MPa)	E of Cornea (MPa)
Compliant	1.8	1.5
Stiff	3	1.5
High Stiff	5.5	3

In addition to variations in the elastic modulus of the sclera, the sclera was reported to be more compliant through its thickness (out of plane) than the in-plane direction by maximum of two order of magnitude (Battaglioli and Kamma 1984). Also, the modulus of the two in-plane directions are similar (Eliaghi et al. 2010). A transversely isotropic elastic material is defined by five independent constants: in-plane and out of plane moduli and Poisson ratios and the shear moduli in the out of plane directions. The modulus normal to the thickness of the sclera was assumed to be 0.03 MPa. The Poisson ratio was assumed to be same in all direction 0.47 based on near incompressibility of the tissue, and the out of plane shear modulus was assumed to be 0.013 MPa (Argento et al. 2014). Table 5 gives the constants of the transverse isotropic sclera model. The transverse isotropic sclera was assigned as “Transverse” model in the analysis.

Table 5 Elastic constants for the transverse isotropic sclera.

Elastic Constant	Numerical Value
$E_{\rho\rho}$	0.03 MPa
$E_{\theta\theta} = E_{\emptyset\emptyset}$	3 MPa
$v_{\theta\emptyset} = v_{\emptyset\theta}$	0.47
$v_{\theta\rho} = v_{\emptyset\rho}$	0.47
μ_t	0.013 MPa

For the eye, material coordinate of the sclera was defined as spherical coordinate positioned in the center of all previously generated sclera curvatures, at intersection of the axial and the equator axes and the material. The buckling was carried out for 1 mm of indentation after analyzing the inflation for all models using 2.5x0.6 mm band. Figure 5.9 shows the percent change in the axial length and the maximum von Mises for all models in terms of the indentation located in the sclera at the sclera-choroid interface at the eye equator.

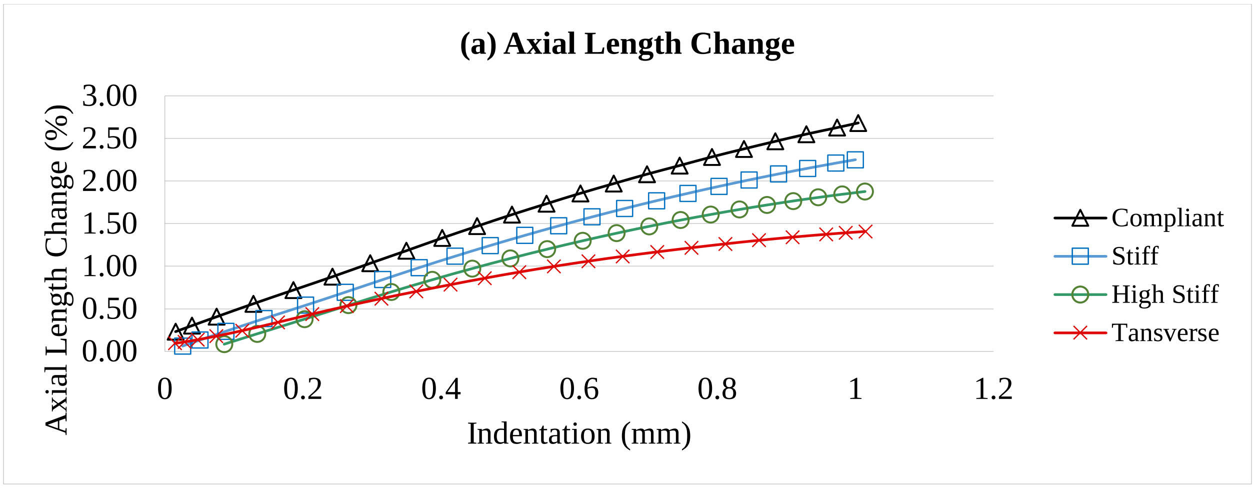

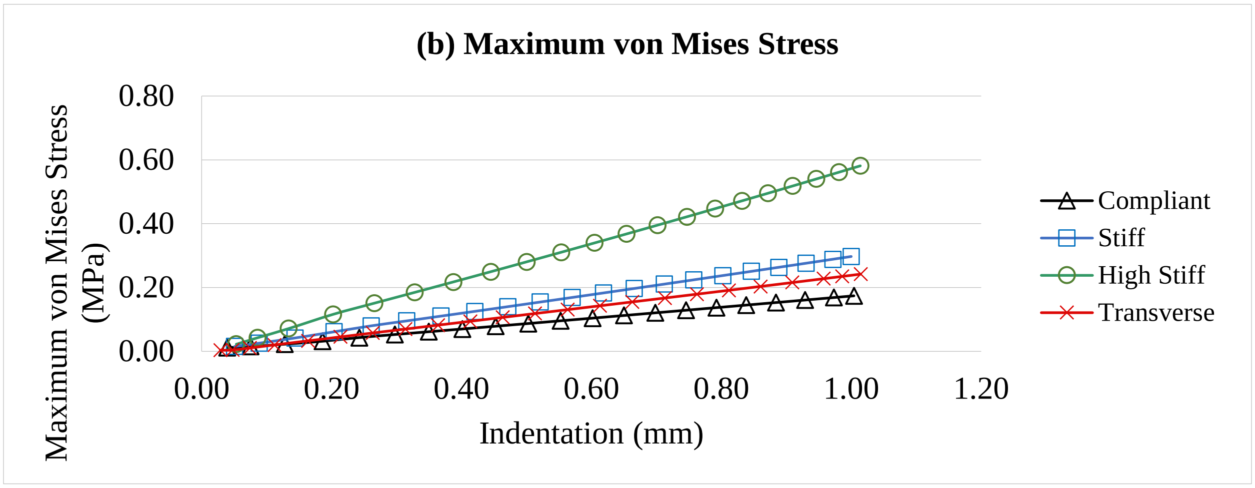

Figure 5.9 (a) axial length change and (b) maximum von Mises stress for all models.

The results show that the axial length increases as the elastic modulus of the sclera decrease in the isotropic models and the relation is reversed for the maximum stresses. Figure 5.10 shows the deformation patterns for different models where the Transverse model had more squeezed sclera since it is more compliant normal to the indentation. The modules of elasticity of the Stiff and High Stiff models are one and about two folds of the Complaint model, respectively. At the maximum indentation, the axial length percent change of Stiff, High Stiff and Transverse model are about: 0.43%, 0.75% and 1.27%, respectively, less than Compliant model. Transverse model showed intermediate amount of maximum stress between Compliant and Stiff model and the High Stiff showed additional 0.412 MPa to the Compliant model. The variation in the sclera elastic modulus can also give insight into the effect of the age where the sclera become stiffer as the age increase (section 3.1.1) and thus less axial length change is expected.

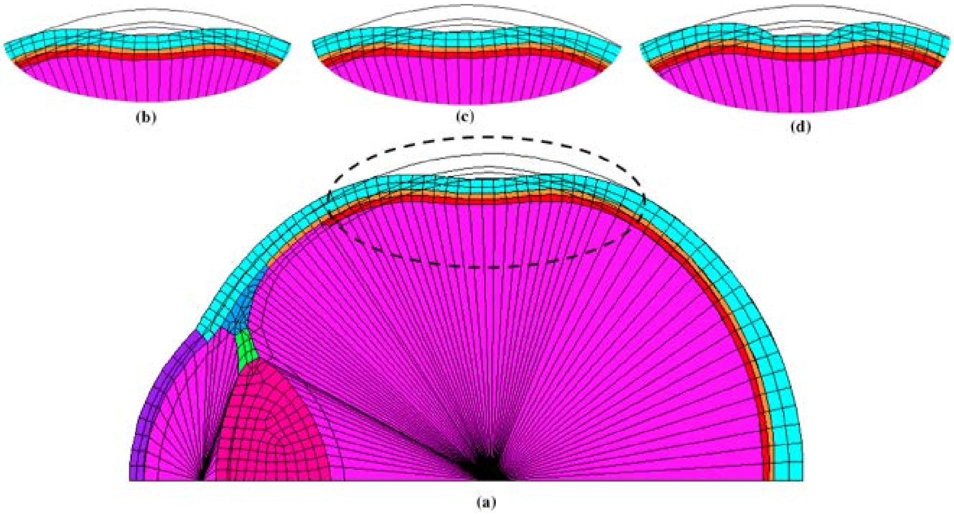

Figure 5.10 Deformation pattern at the indent sclera for: (a) Compliant, (b) Stiff, (c) High Stiff and (d) Transverse model.

5.2.4 Mesh refinement

To evaluate the effect of mesh refinement effect on axial length change and the maximum von Mises stress, the number of elements in the sclera, which is the main structural tissue of the eye, was varied in the axisymmetric and the three-dimensional models. With 25% cornea thinning, analysis was done for the case of a 3x0.68 mm band with 1.5 mm indent in the axisymmetric model and a 5x1 mm of 180˚ extent segmental buckle with 1 mm indent used for the three-dimensional model. In the original models, the number of elements along the circumference of sclera contact with buckle and band and within ± 30° from buckle center are of 26 and 21, respectively, were doubled, inflated and then indent with 1 mm at the equator. Figure 5.11 shows the change in the axial length and the maximum von Mises in location of maximum stresses for before and after refinement of all models where the maximum stress of the buckle located in the sclera surface at the end of the buckle extent.

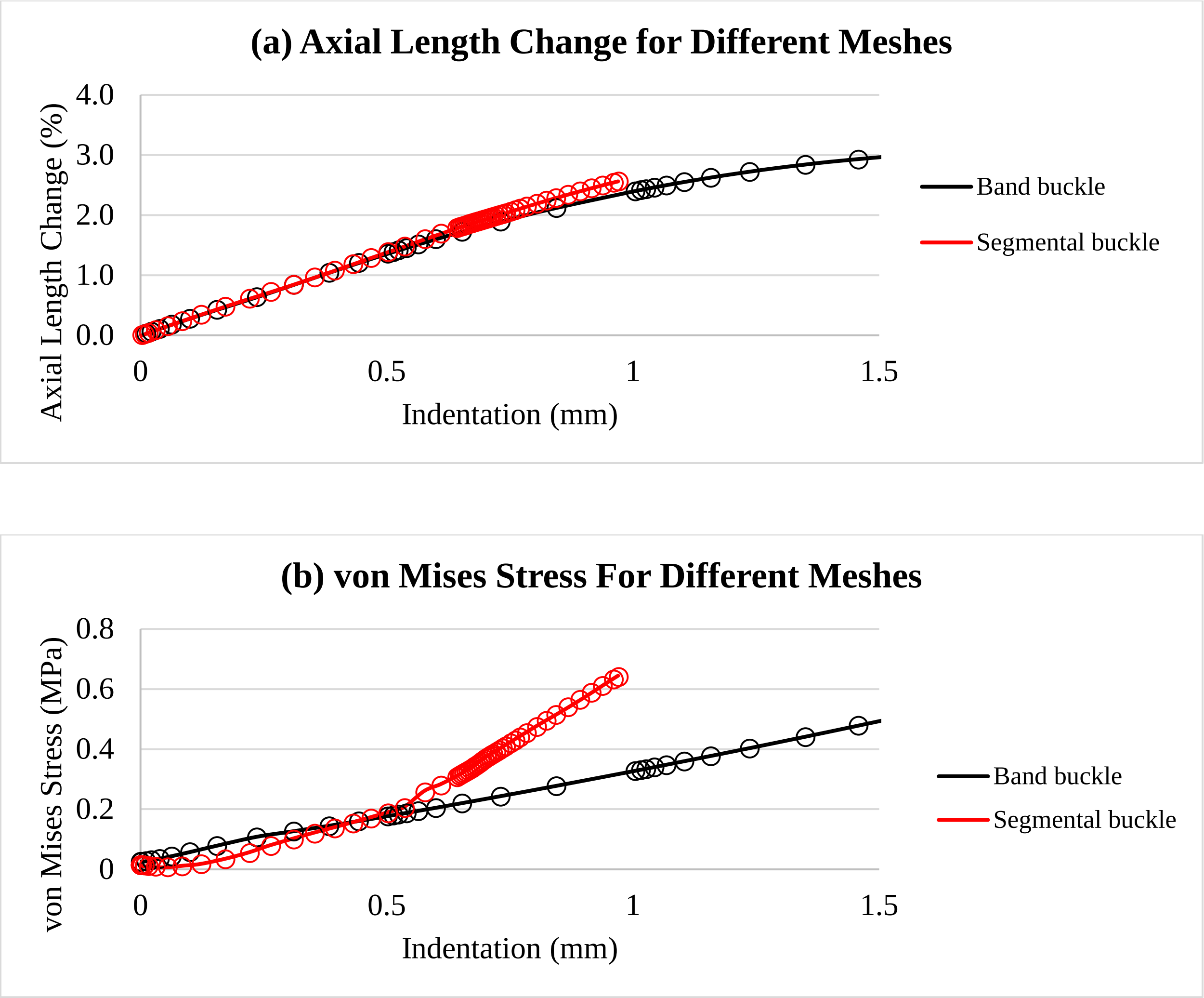

Figure 5.11 (a) axial length change and (b) von Mises stress of axisymmetric (band) and three-dimensional (segment) model for orginal (line) and refined (o) mesh.

Results of the axial length and the peak von Mises stress for the different meshes in the axisymmetric and the three-dimensional models are in good match and thus there is no significant difference with the refinement of high order elements in the buckling of both models. Mesh refinement throw the eye wall thickness was done in a previously study and no significant difference was found (Aldhafeeri R. 2015).

6.0 ENCIRCLING BAND ANALYSIS

In this section, the effect of eye buckling with an encircling band will be analyzed in terms of cornea thinning, indentation, width and location of the band from limbus. Different outputs will be investigated such as changes in the axial length, anterior chamber depth, cornea power, total eye power, maximum stresses on the eye and volume of the vitreous cavity which is another way of expressing the deformation in clinical studies. Since the load and geometry are axisymmetric, the axisymmetric model will be utilized for this purpose.

Eyes with normal cornea thicknesses and with 25% and 50% thinned cornea are investigated. Different bands geometries of 2.5, 3 and 3.5 mm in width are considered here (Figure 6.1). The band is applied at the anterior, equator and posterior of the sclera which is about 11.5, 12.6 and 13.7 mm along sclera surface from limbus. Also, the results are reported for 0.5, 1 and 1.5 mm indentation of the sclera.

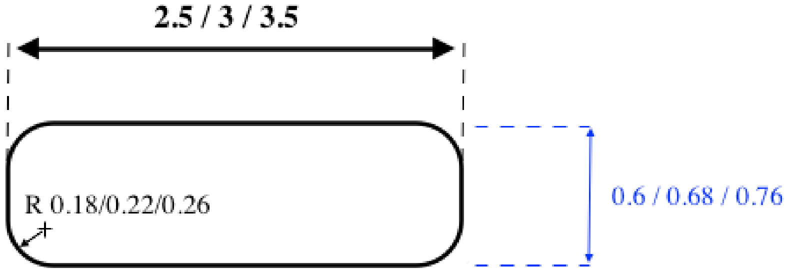

Figure 6.1 Dimensions of the bands.

6.1 RESULTS

Figure 6.2 shows a sample eye deformation pattern for the case of a 1.5 mm indentation of 3 mm band at anterior, equator and posterior of the sclera on eyes with 25% cornea thinning and analogues generated full views of the models. The change in the axial length can be expressed in millimeter or diopter. The change in diopter is given by:

$$\Delta d = \frac{n_c}{f} - \frac{n_c}{AL} \quad (6.1)$$

where n_c is the refractive index of the cornea equal to 1.336, f is the focal length in mm which is assumed to be equal to the pre-buckled axial length Al of the undeformed eye (having zero refractive error) and assuming the cornea curvature is unchanged (Wang et al. 2007). A one diopter change in the axial length is equal to change of 0.4244, 0.4195 and 0.4146 mm for eyes with 0, 25 and 50% cornea thinning, respectively. Figure 6.3 shows the calculated axial length change in diopters as a function of cornea thinning, band width, indentation and location of the indentation where a positive diopter indicates a myopic shift in the axial length of the eye.

All models have anterior chamber depth of about 2.75 mm which can change due to buckling. Figure 6.4 gives the reduction percent in the anterior chamber depth (ACD) for all models in terms of cornea thinning, band width, indentation and location of the indentation. The negative reduction indicates increase in ACD.

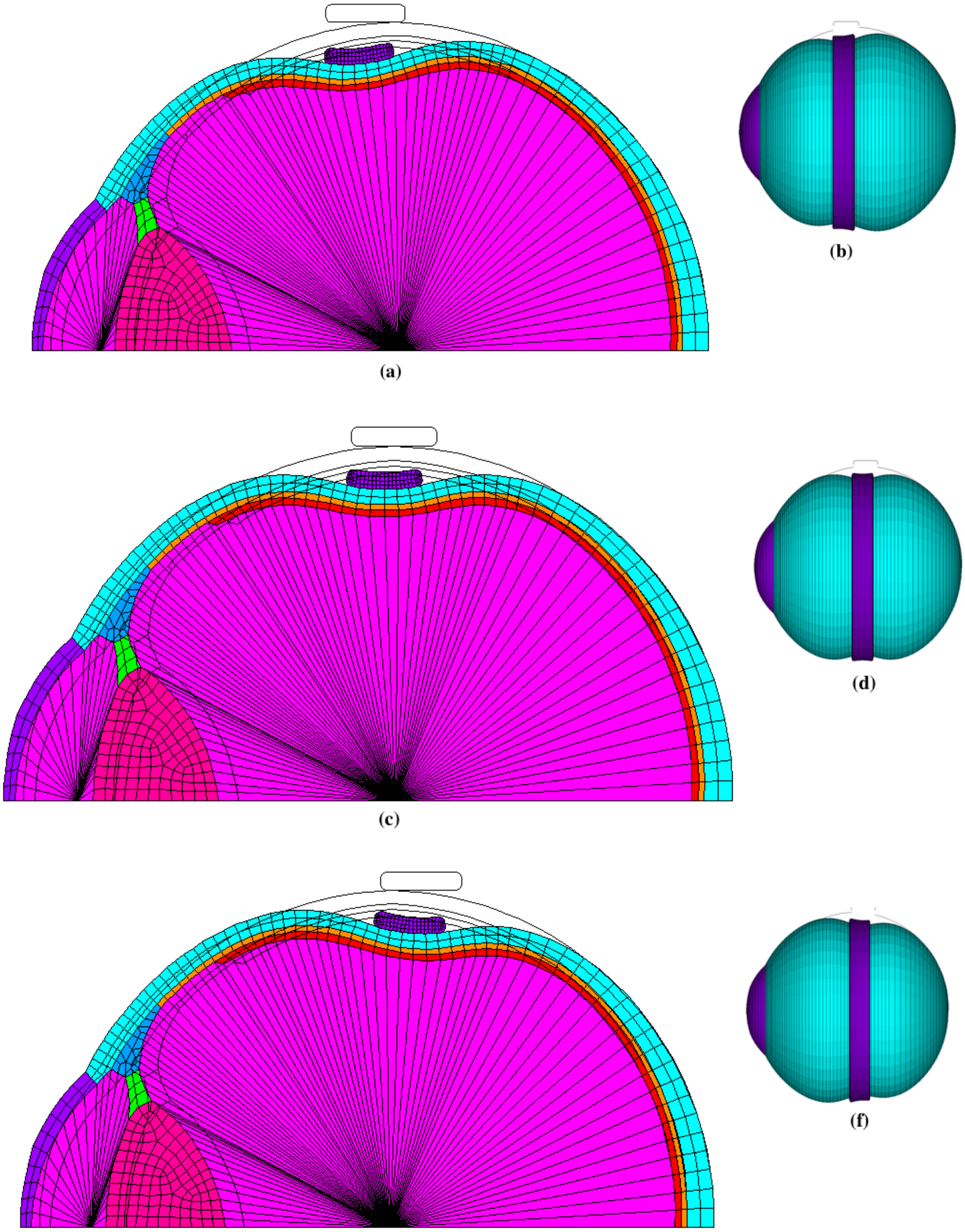

Figure 6.2 Deformed Models of 3 mm band for 1.5 mm indentation and 25% cornea thinning at (a) anterior, (c) equator and (e) posterior of sclera and their generated full views (b), (d) and (f), respectively.

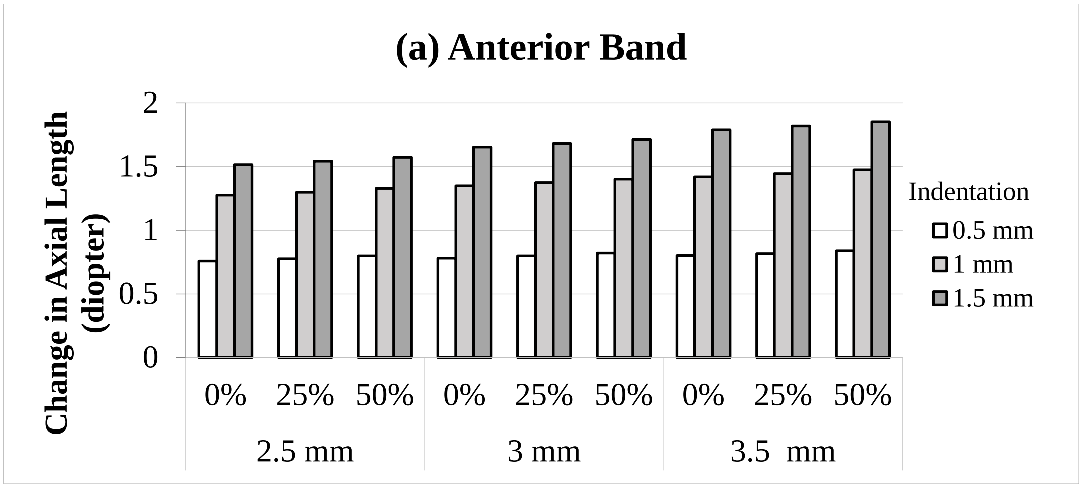
(a) Anterior Band

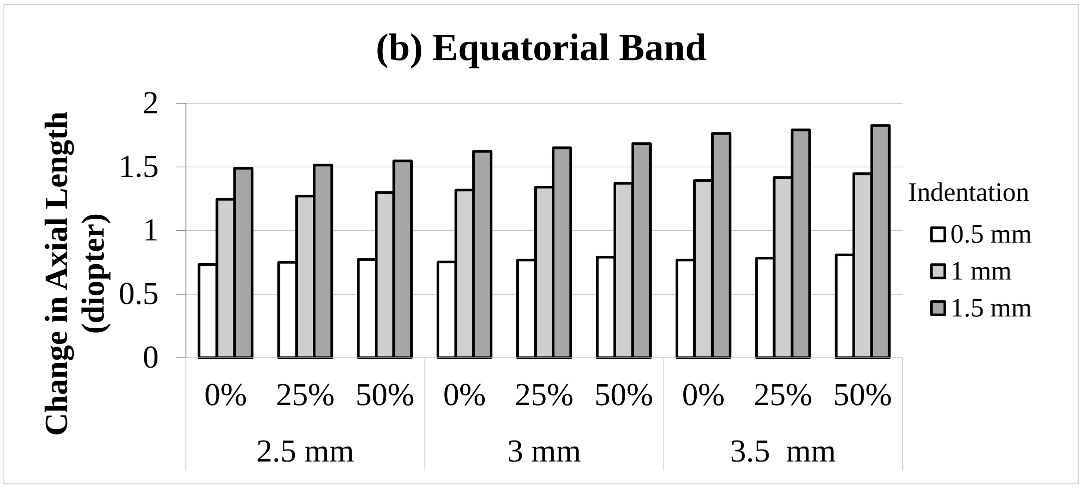
(b) Equatorial Band

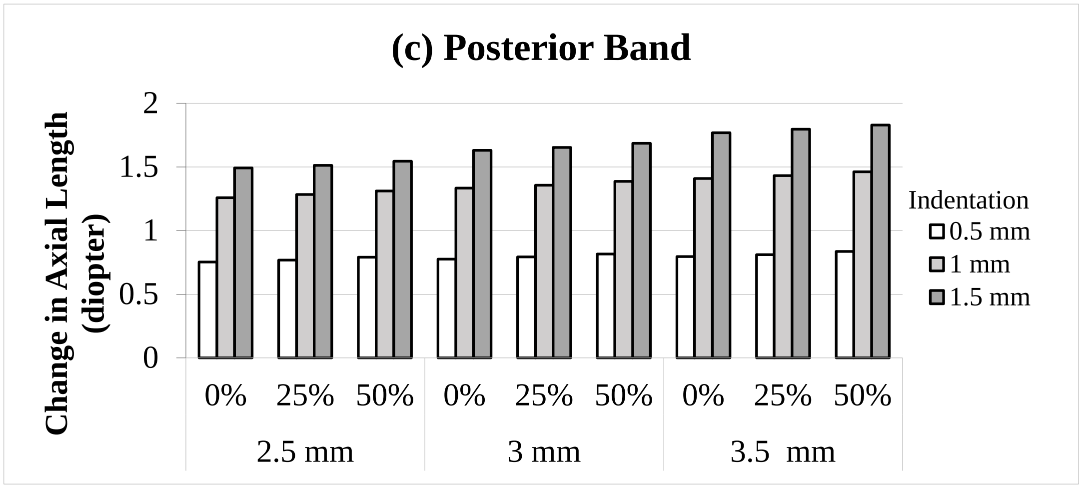
(c) Posterior Band

Figure 6.3 Axial length change in diopters for various cornea thinning, buckle widths, indentations and locations: (a) anterior, (b) equator and (c) posterior of the sclera.

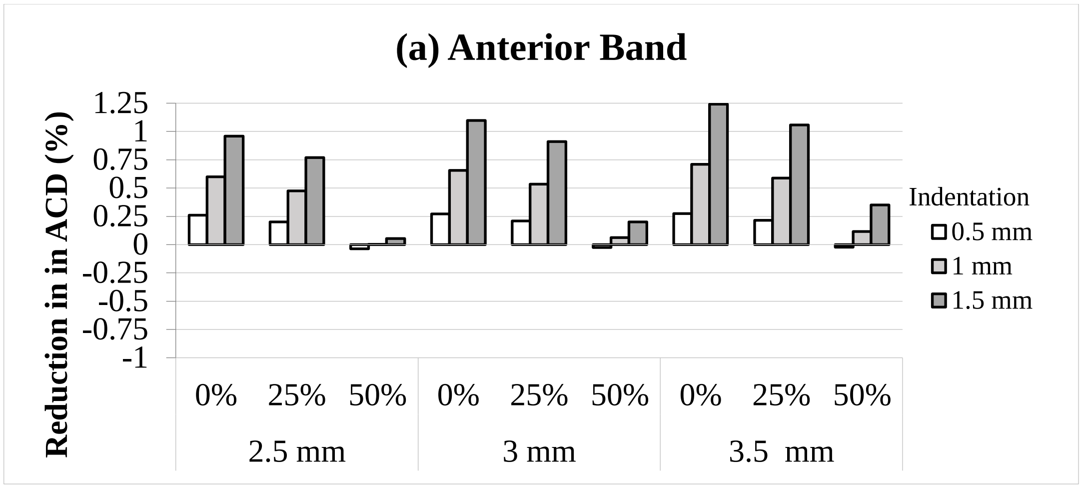

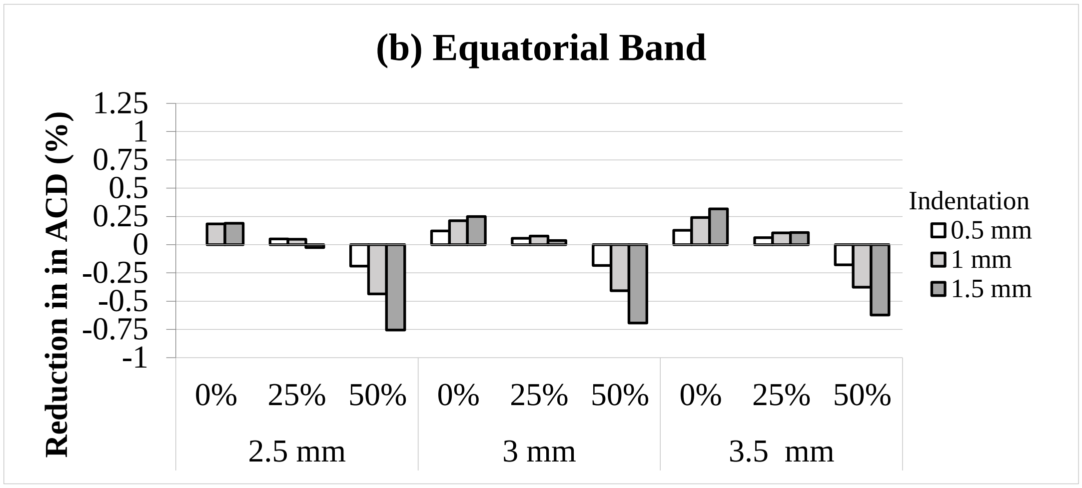

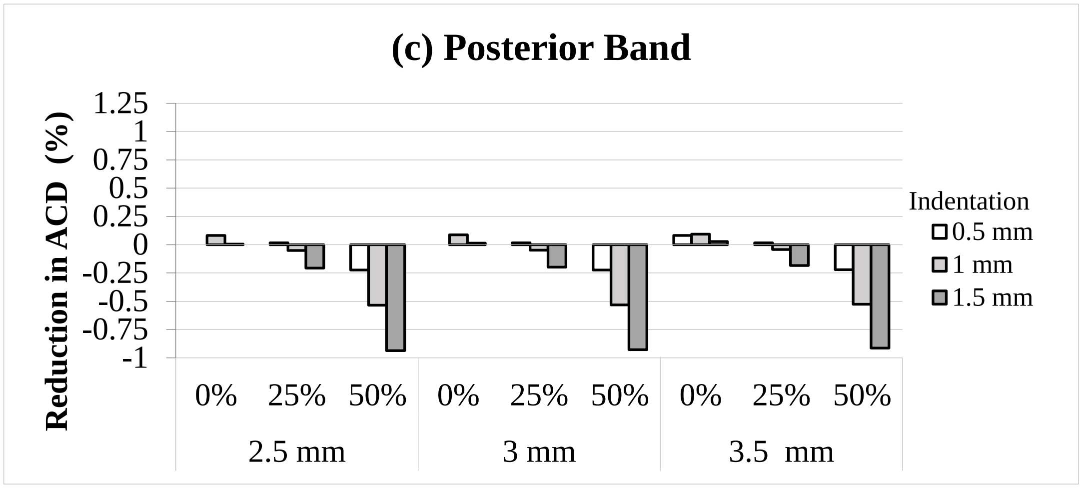

Figure 6.4 Reduction in ACD for various cornea thinning, buckle widths, indentations and locations: (a) anterior, (b) equator and (c) posterior of the sclera.

Eye buckling can change the cornea curvature and thus its refractive power and the total eye power. Cornea power along a meridian (m) at any state can be calculated using the equation:

$$P_m = (n_c - n_{air})/r_m \quad (6.2)$$

where n_{air} is the refractive index of the air equal to 1 and r_m is the radius of curvature along a meridian. Since the model is axisymmetric, P_m equals the spherical power of the cornea P_c. To calculate the radius of the curvature, points at the 6 mm cornea optical zone are fitted to circle using a best fit using a MALAP subroutine (Chernov, N. 2009). Figure 6.5 shows example points on the deformed cornea of the 25% thinned cornea with 3 mm band at the equator of the sclera, where the points in the upper half of the cornea is reflected for more accuracy in the circular fitting. The calculated curvatures for original corneas before buckling are: 7.813, 9.979, 13.806 mm for 0, 25 and 50% thinning, respectively. Figure 6.6 gives the calculated change in cornea power for different locations as function of cornea thinning, buckle widths and indentation. Positive diopter indicates steepening of the cornea (myopic cornea) and negative diopter indicates flattening of the cornea. The lens curvatures showed no change in its curvatures.

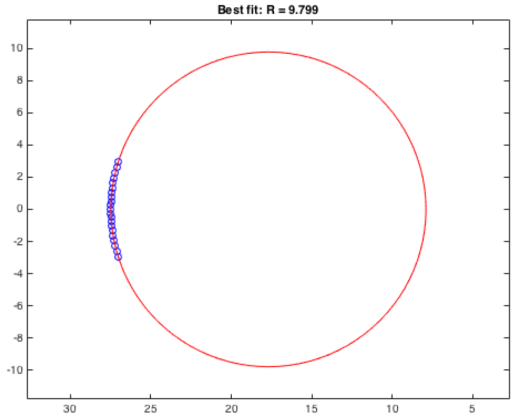

Figure 6.5 Example of circle fit in the optical zone, (line) circle fit, (o) points of cornea curvature (model with 3 mm band, 25% thinned cornea at 1.5 indentation at equator).

The total eye power (P) is given by the formula:

$$P = P_c + P_l - P_c P_l (ACD)/n_c \quad (6.3)$$

where Pi is the lens power fixed at 19 diopters and ACD is the anterior chamber depth in mm. The change in the total eye power is in terms of the change of the axial length (Δd) and cornea power (ΔP) is:

$$\Delta P_{total} = \Delta P + \Delta d \quad (6.4)$$

Figure 6.7 shows the total eye power change as function of cornea thinning, band width, indentation and location of the indentation.

Figure 6.8 gives the percent change in the volume of the vitreous cavity for different band widths, indentations and locations. The original volume of the vitreous cavity is about 5.543 ml. Figure 6.9 gives the normalized maximum von Mises stress which is located at the lower surface of the sclera normal to center of the band normalized by analogues stress in inflation of 17.34 kPa for different band widths, indentations and locations. Figure 6.10 shows the von Mises stress distribution for models with 3 mm band and 25% thinned cornea at anterior, equator and posterior of the sclera.

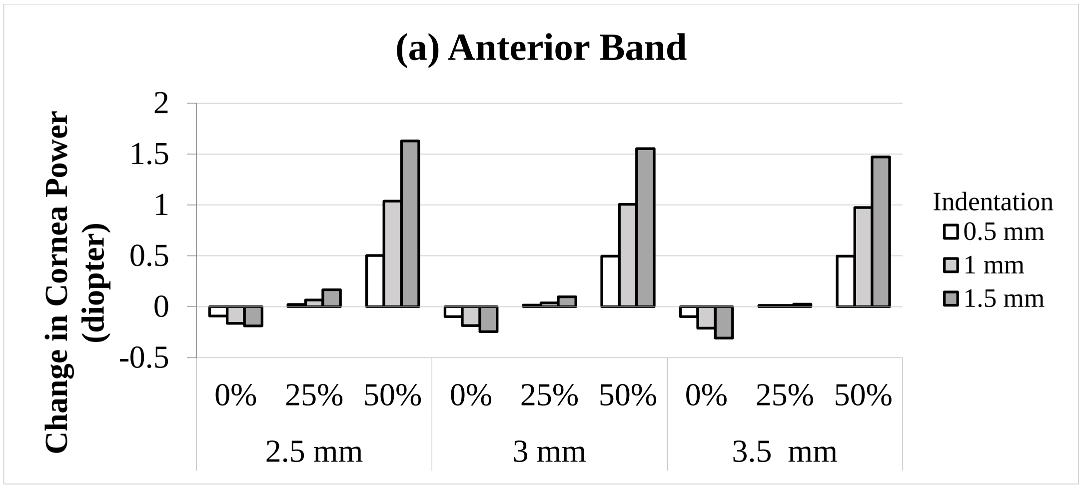

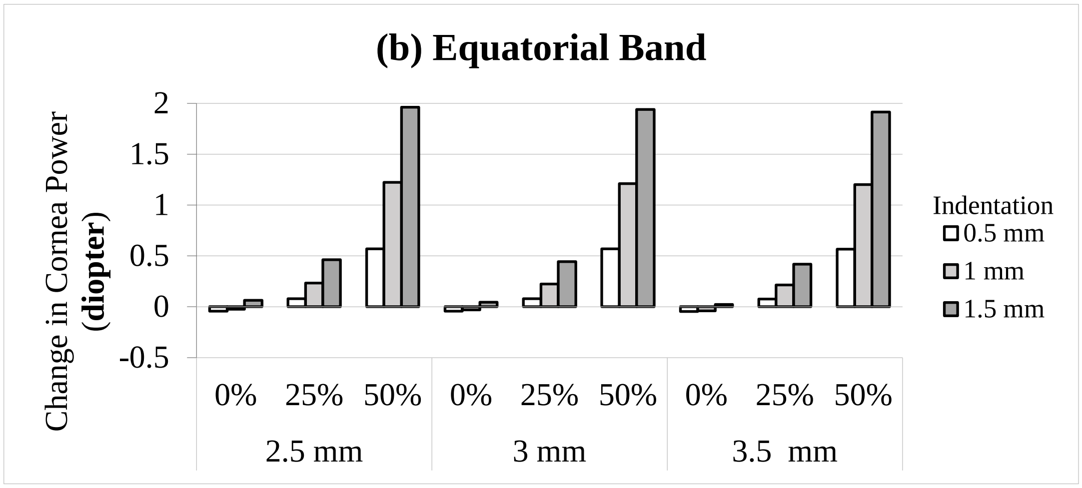

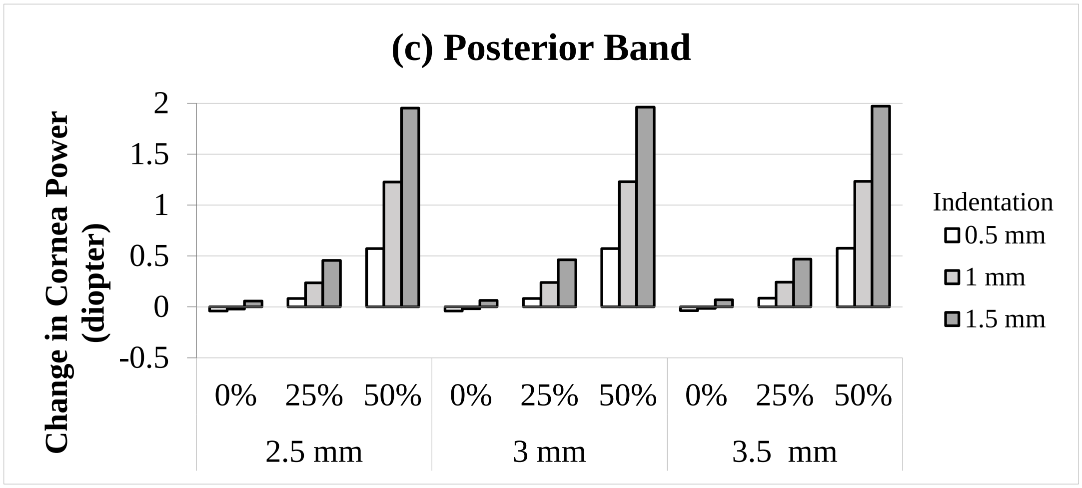

Figure 6.6 Cornea power change for different cornea thinning, buckle widths, indentations and locations: (a) anterior, (b) equator and (c) posterior of the sclera.

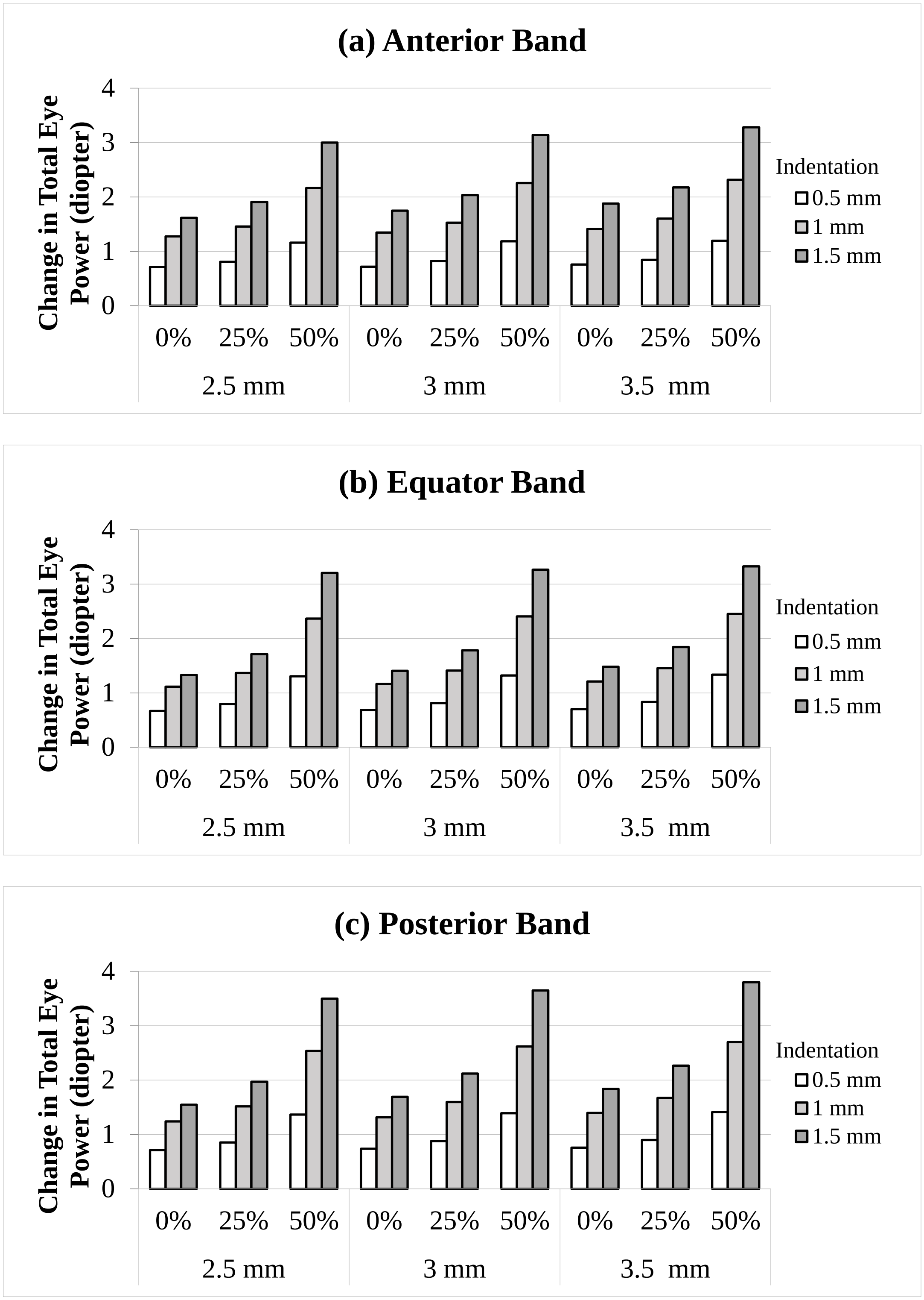

Figure 6.7 Change in total eye power for different cornea thinning, buckle widths, indentations and locations: (a) anterior, (b) equator and (c) posterior of the sclera.

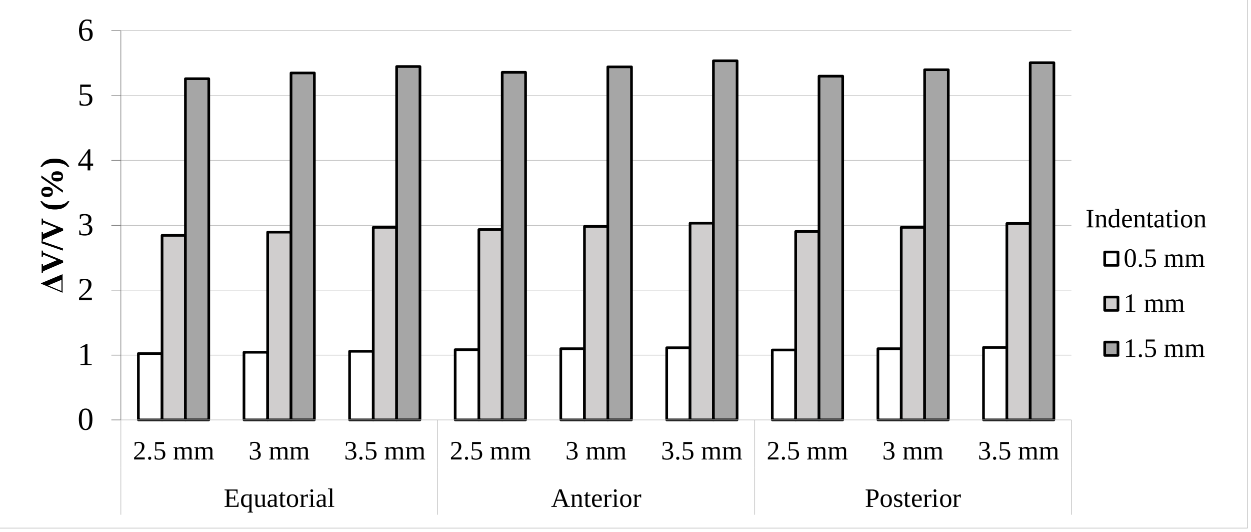

Figure 6.8 Change in vitreous cavity volume in terms of various buckle widths, locations and indentations.

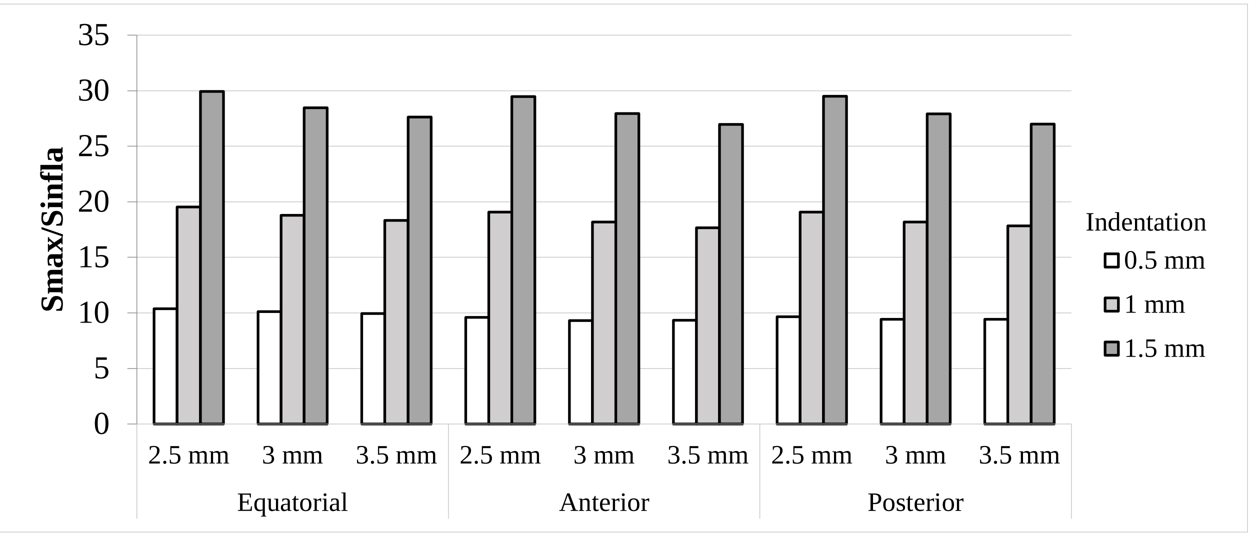

Figure 6.9 Maximum von Mises stress in terms of various buckle widths, locations and indentations.

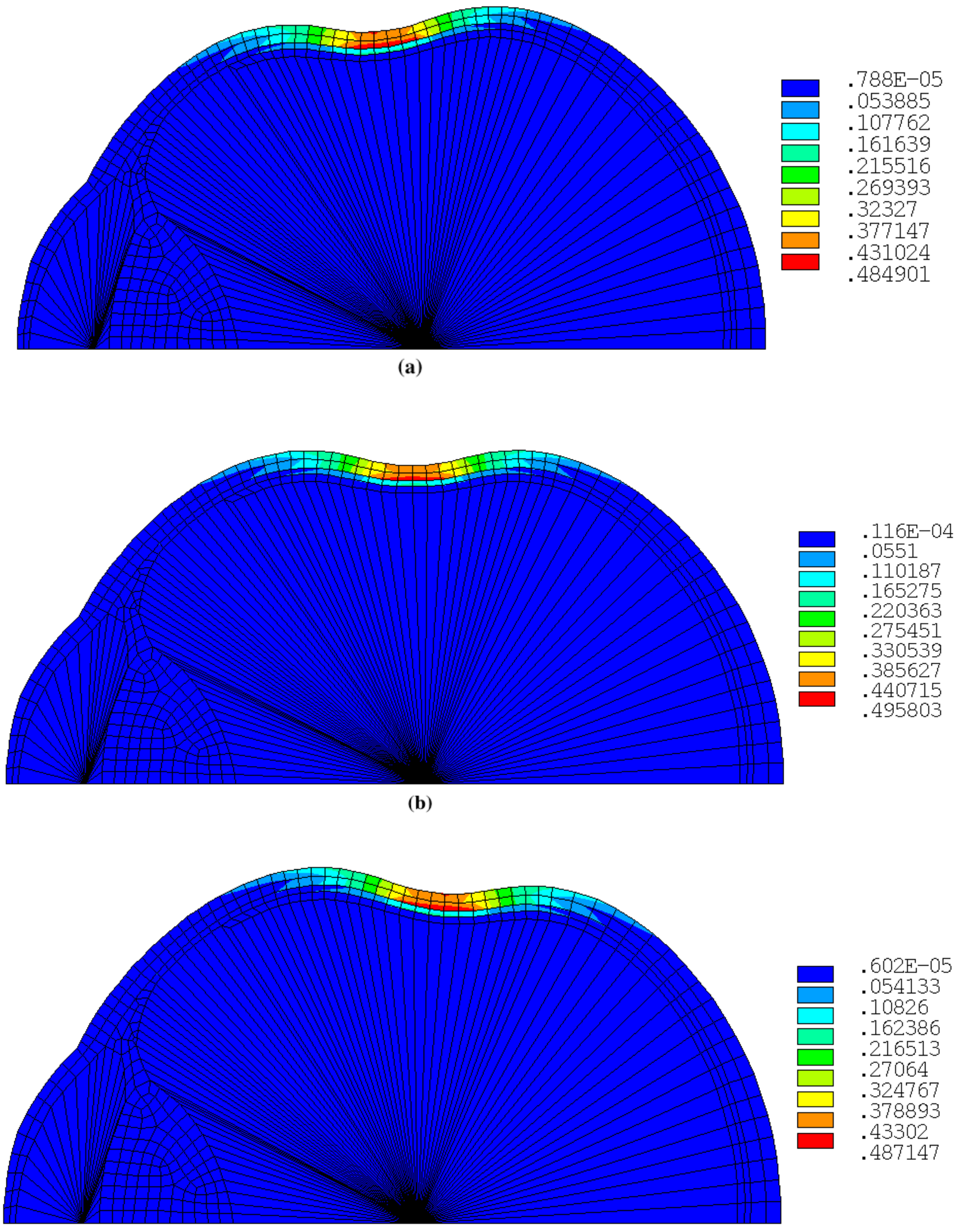

(a)

(b)

(c)

Figure 6.10 von Mises stress distribution for 3 mm band for 1.5 mm indentation and 25% cornea thinning for (a) anterior, (b) equator and (c) posterior band position.

6.2 DISCUSSION

This study investigated the effect of cornea thinning, buckle width, indentation and the location of the buckle in encircling band scleral buckling in retinal reattachment. Finite element analysis with an axisymmetric eye model was used to calculate the eye deformation, induced refractive errors and eye stresses.

In clinical measurements of eyes with encircling buckling, the axial length showed increase of 0.54 and 0.81 mm (Burton et al. 1977, Wang et al. 1994) and change in cornea power of 0.01, -1.7 and 0 diopters (Kinoshita et al. 1994, Hayasshi et al. 1997, Weinberger et al. 1999). It was also reported to cause reduction in anterior chamber depth of 0.19 mm (Burton et al. 1977).

In this study, the axial length was found to increase for all models where the amount of the indentation had the largest effect on increasing the axial length among cornea thinning, widths and location of the band since indentation amount can reflect the amount of load on the eye. The induced axial length increases for 2.5 mm wide band at the equator on an eye with normal cornea thickness are 0.32, 0.54 and 0.65 mm for 0.5, 1 and 1.5 mm of indentation, respectively.

In addition to the amount of the indentation, cornea thinning had a large effect on increasing the steepening of cornea (cornea myopia) which is also reflected in the total eye power. Greater thinning of the cornea will reduce the stiffness and thus increase the deformation of the structure with load. These changes in the cornea with buckling increase myopia in the cornea and the eye. The change in cornea power is about 0.06, 0.46 and 1.96 diopters, and the change in the eye power is about 1.32, 1.71 and 3.2 diopters for 0, 25 and 50% cornea thinning, respectively, for a 2.5 mm thick band at the equator with a 1.5 mm of indentation.

Less cornea thinning and buckle distance from limbus induced a greater reduction in the anterior chamber depth where other parameters had less effect. The induced reduction in anterior chamber depth for a 2.5 mm thick band with a 1.5 mm indentation on an eye with a normal cornea thickness are 0.004, 0.01 and 0.03 mm for a posterior, equatorial and anterior band, respectively. The vitreous cavity volume change is mostly affected mostly by the amount of indentation, for example, a 2.5 mm band at the equator had change percent of 1.03, 2.84 and 5.26% for each 0.5 mm increase in the indentation. The maximum stress is located at the bottom of the indent part of the sclera where the amount of the indentation increases the stresses by about a factor of nine for each 0.5 mm of indentation.

In conclusion, the axial lengths of all models were increased mainly by the amount of indentation. Greater thinning of cornea, band width and location had little effect on the axial length change. However, in addition to indentation, cornea thinning caused more steepening of the cornea and myopia in the total visual power of the eye. The anterior chamber depth showed more reduction for narrow bands on normal cornea close to limbus. All models had reduction in their vitreous cavity volume which is induced most by the amount of indentation. Increased buckling indentation caused highest stresses at the sclera-choroid interface at the indention site where a thinner band at the equator had the maximum stresses of all the models.

7.0 SEGMENTAL BUCKLE WITH ENCIRCLING BAND ANALYSIS

This part of study to investigate the effect of buckling using segmental buckle of different widths and extents with encircling band on eyes with normal cornea and thinned corneas, on the deformation, optical power of the eye and eye stresses. The analysis will evaluate changes in the axial length, anterior chamber depth, symmetry of the cornea, cornea tilt, cornea power, total eye power, vitreous cavity volume and stresses on the eye.

For this, a symmetric three-dimensional finite element analysis of eye was performed with 0, 25 and 50% thinned cornea with buckle widths of 3, 5 and 7 mm and buckle extents of 90˚, 180˚ and 270˚ around the eye. The buckles have rounded edges of length 0.5 mm and groove of 2.6x0.25 mm which is in most medical segmental buckle for placement of encircling band of 2.5x0.6 mm. Also, each buckle was subjected to three sclera indentations of 1/3, 2/3 and 1 mm measured at the center of the buckle contact. Indentation beyond 1mm in all models caused a non-uniform indentation where the buckle at the center became fixed and the tip start to penetrating the eye.

7.1 RESULTS

Figure 7.1 shows example of the deformation pattern for the 5 mm buckle with 180˚ extent on an eye with 25% cornea thinning and a 1 mm indentation. Figure 7.2-3 show the change in the axial length in diopters (using equation 6.1), and the change in the anterior chamber depth (ACD) in percent, respectively, as function of cornea thinning, buckle widths, indentation for different buckle extents.

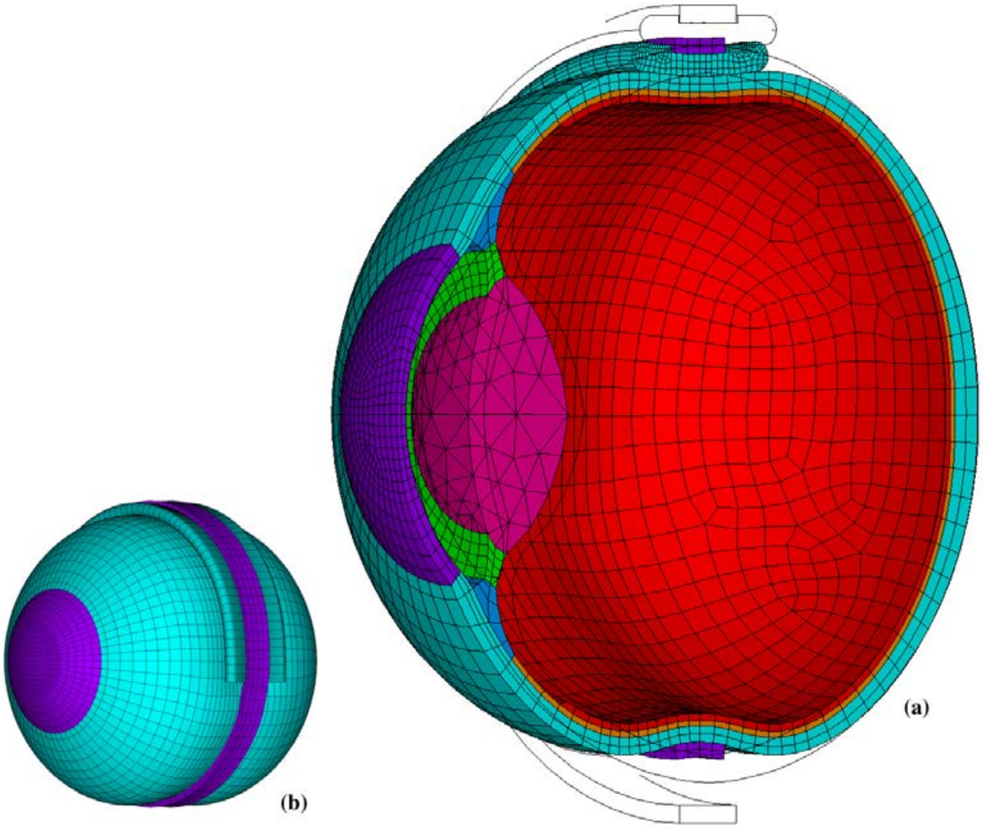

Figure 7.1 Deformed model (a) with 25% thinned cornea, 5 mm thick and 180˚ extent buckle at 1 mm indentation; and (b) full model.

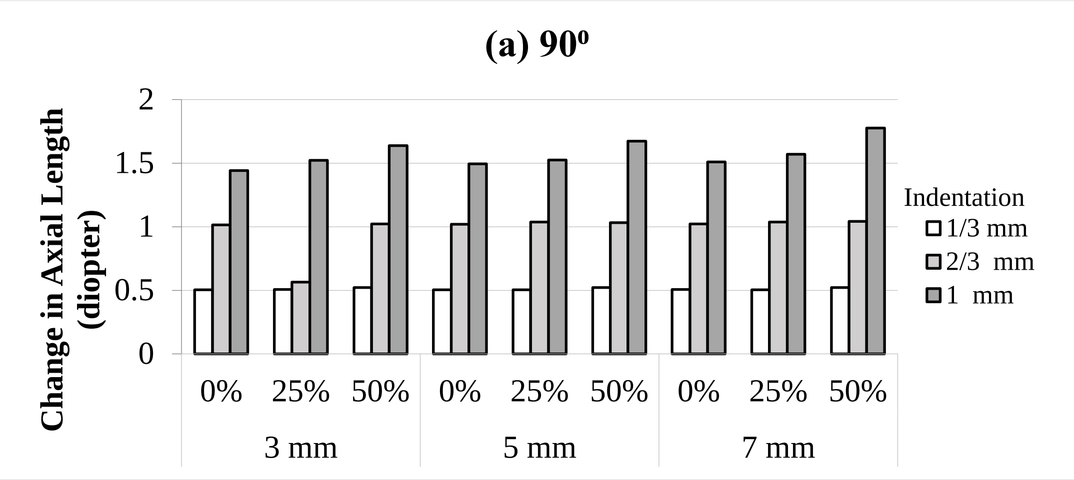

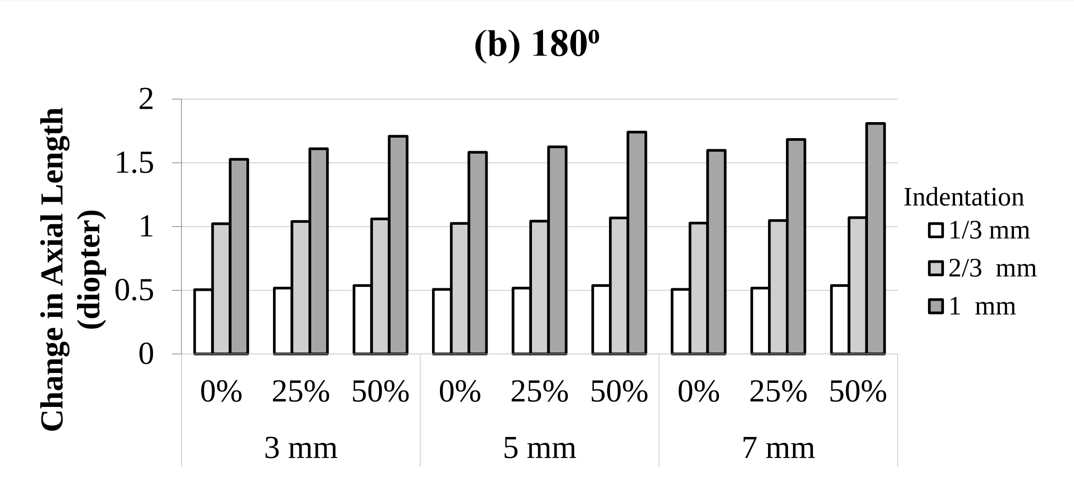

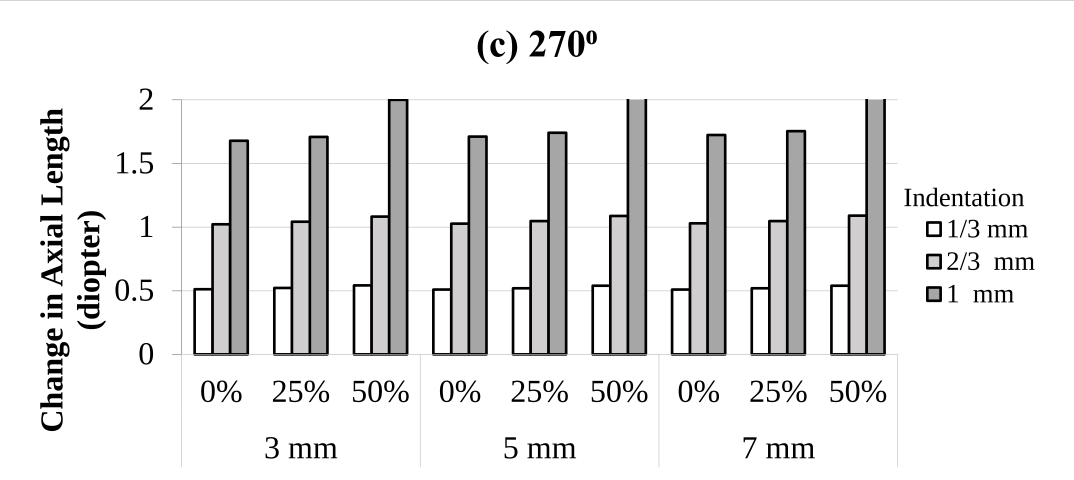

Figure 7.2 Axial length change in diopter for different the cornea thinning, buckle widths, indentations and extents: (a) 90˚, (b) 180˚ and (c) 270˚.

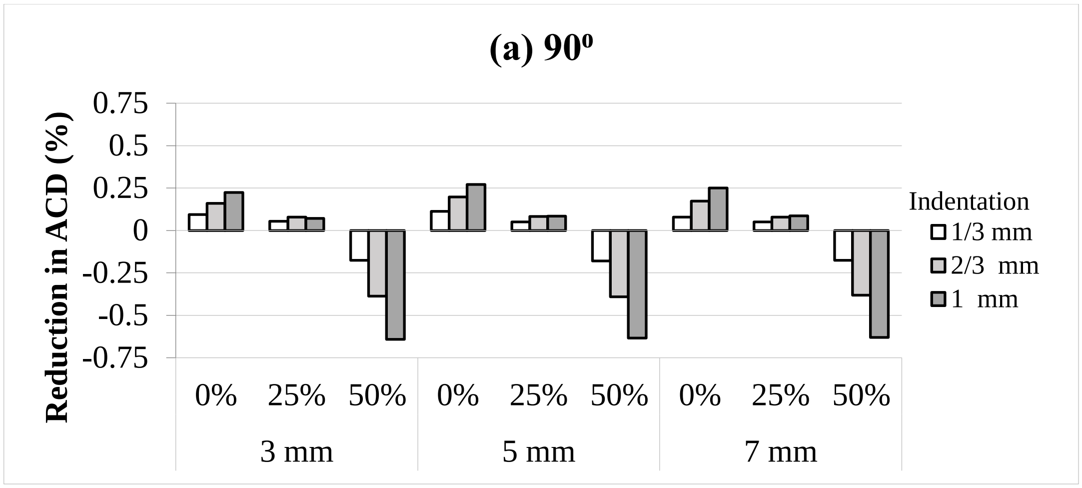

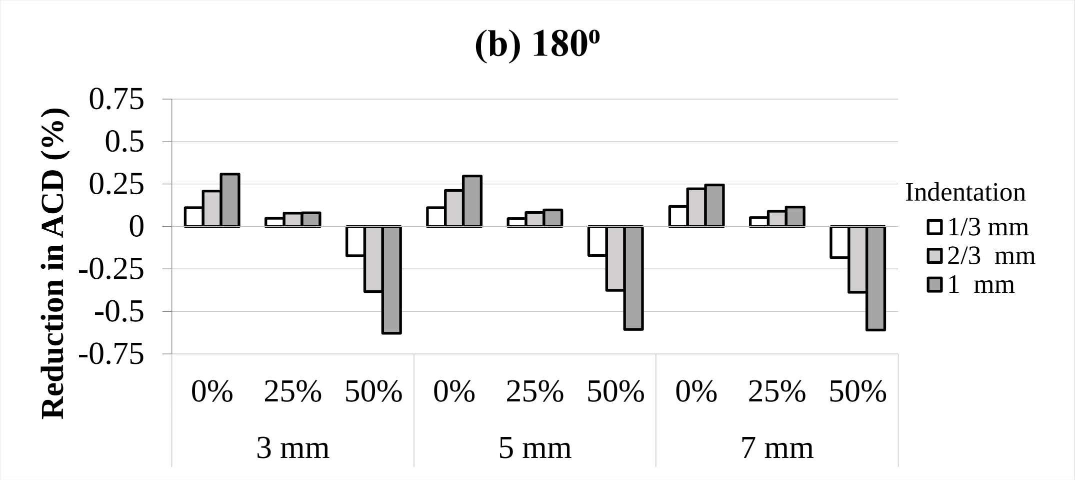

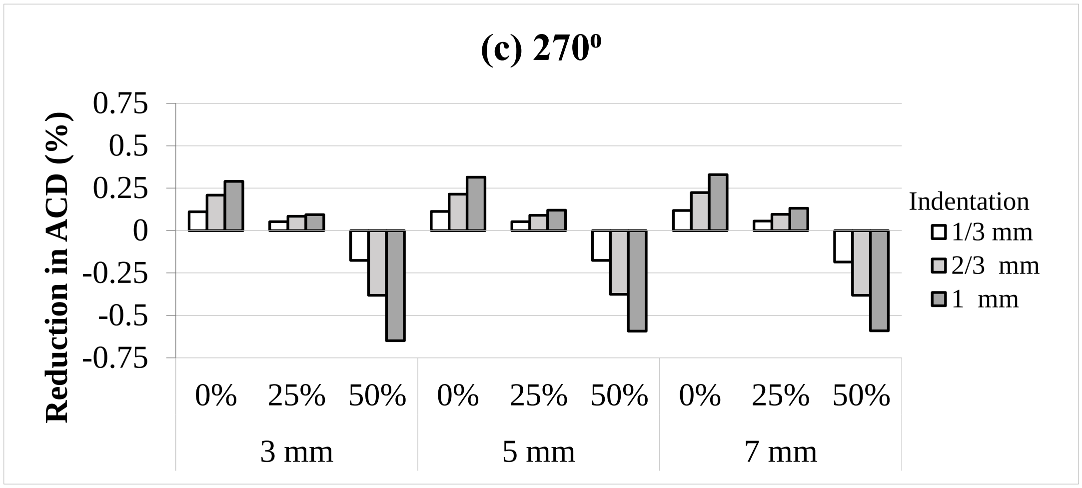

Figure 7.3 Change percent in ACD for different cornea thinning, buckle widths, indentations and extents: (a) 90˚, (b) 180˚ and (c) 270˚.

The imposed buckling load can cause non-uniform deformation to the anterior surface of the cornea and thus can decrease the symmetry of the cornea. Cornea astigmatism error in diopter (asymmetry index) is calculated by subtracting the power of the cornea at the meridian on the symmetry plane and the meridian normal to it within 6 mm diameter of optical zone using equation 6.2. Figure 7.5 gives the astigmatism in diopters for different buckle extents in terms of cornea thinning, buckle width and amount of indentation. The positive diopters indicate more steepening in the meridian on the symmetry plane.

The cornea exhibits a tilt away from center of the buckle (illustrated in Figure 7.4). The evaluated cornea tilt for different buckle extents in terms of cornea thinning, buckle width and indentation is given in Figure 7.6.

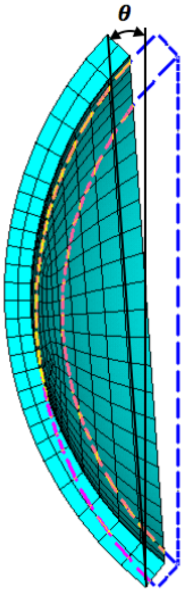

Figure 7.4 Cornea tilt θ (rotation pattern).

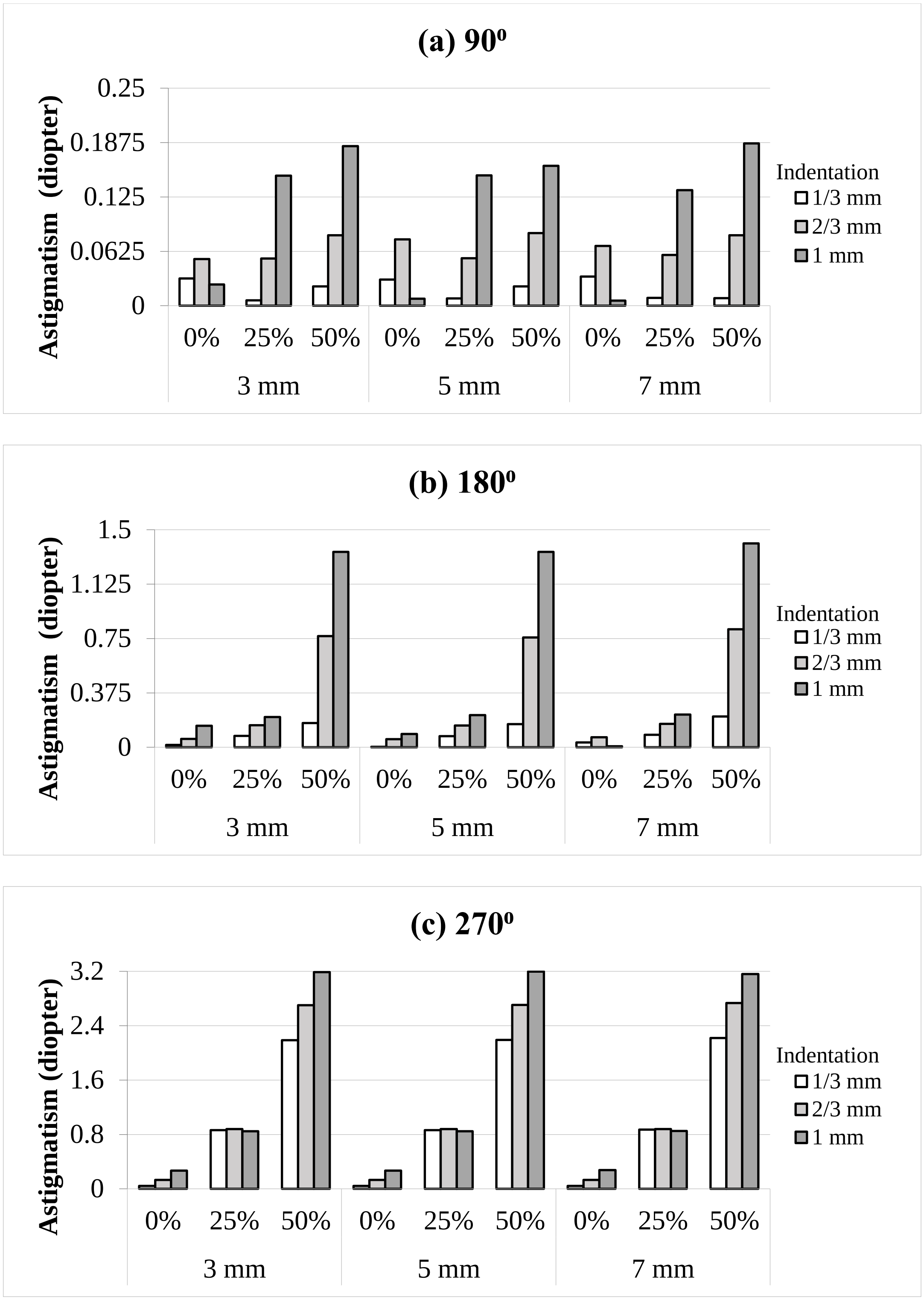

Figure 7.5 Astigmatism in diopter in terms of various cornea thinning, the buckle widths, indentations and extents: (a) 90˚, (b) 180˚ and (c) 270˚.

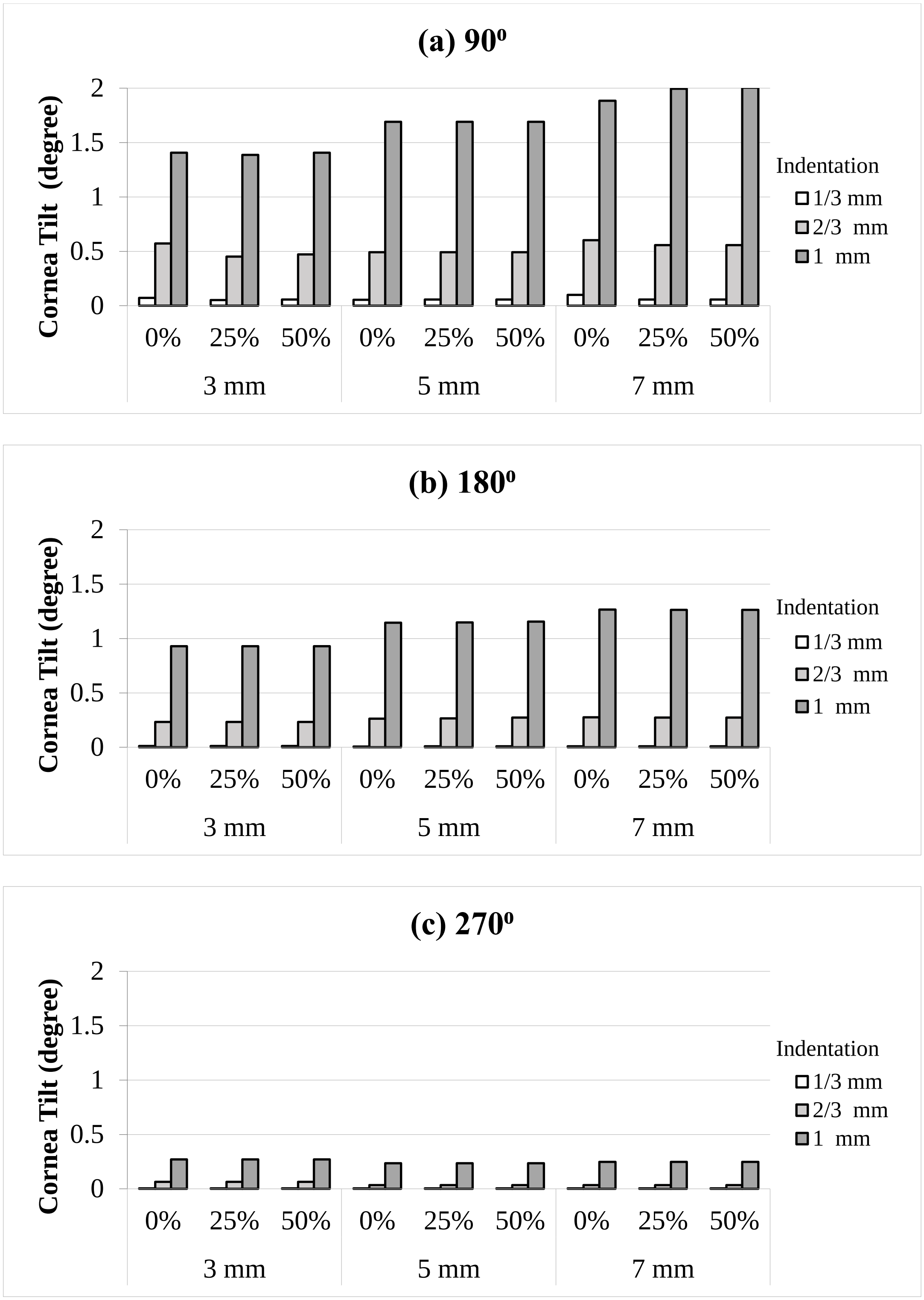

Figure 7.6 Cornea tilt for various cornea thinning, the buckle widths, indentations and extents: (a) 90˚, (b) 180˚ and (c) 270˚.

The spherical power of cornea is calculated by substituting the radius of curvature of the sphere into equation 6.2. For calculating the radius, points on the deformed cornea surface within the optical zone of the anterior surface of the cornea are fitted to a sphere using best sphere fit programmed MALAP (Figure 7.7), (Jennings, A. 2011). The fitted curvatures for original corneas before buckling are: 7.817, 9.979, 13.806 mm for 0, 25 and 50% thinning, respectively.

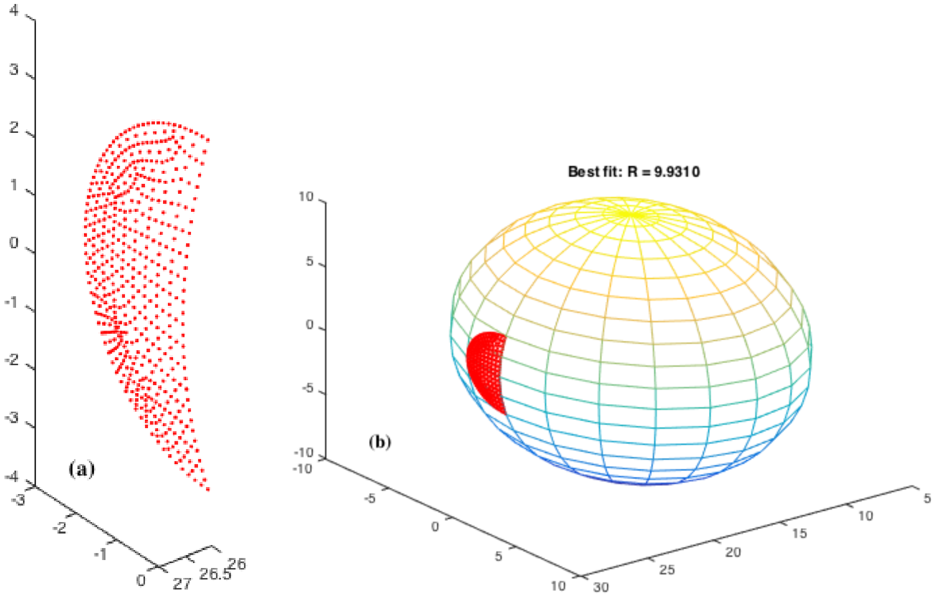

Figure 7.7 Deformed points of 25% thinned cornea due to 1 mm indentation of 5 mm thick and 180˚ extent buckle (a); and fitted sphere to the points (b).

Figure 7.8 gives change in cornea power in diopters for the different buckle extents as function of cornea thinning, buckle width and indentation. Positive and negative diopters indicate steepening and flattening of the cornea, respectively. The change in total eye power in diopter can be calculated using equation 6.4 and it is shown in terms of cornea thinning, buckle width and indentation for different buckle extents in Figure 7.9.

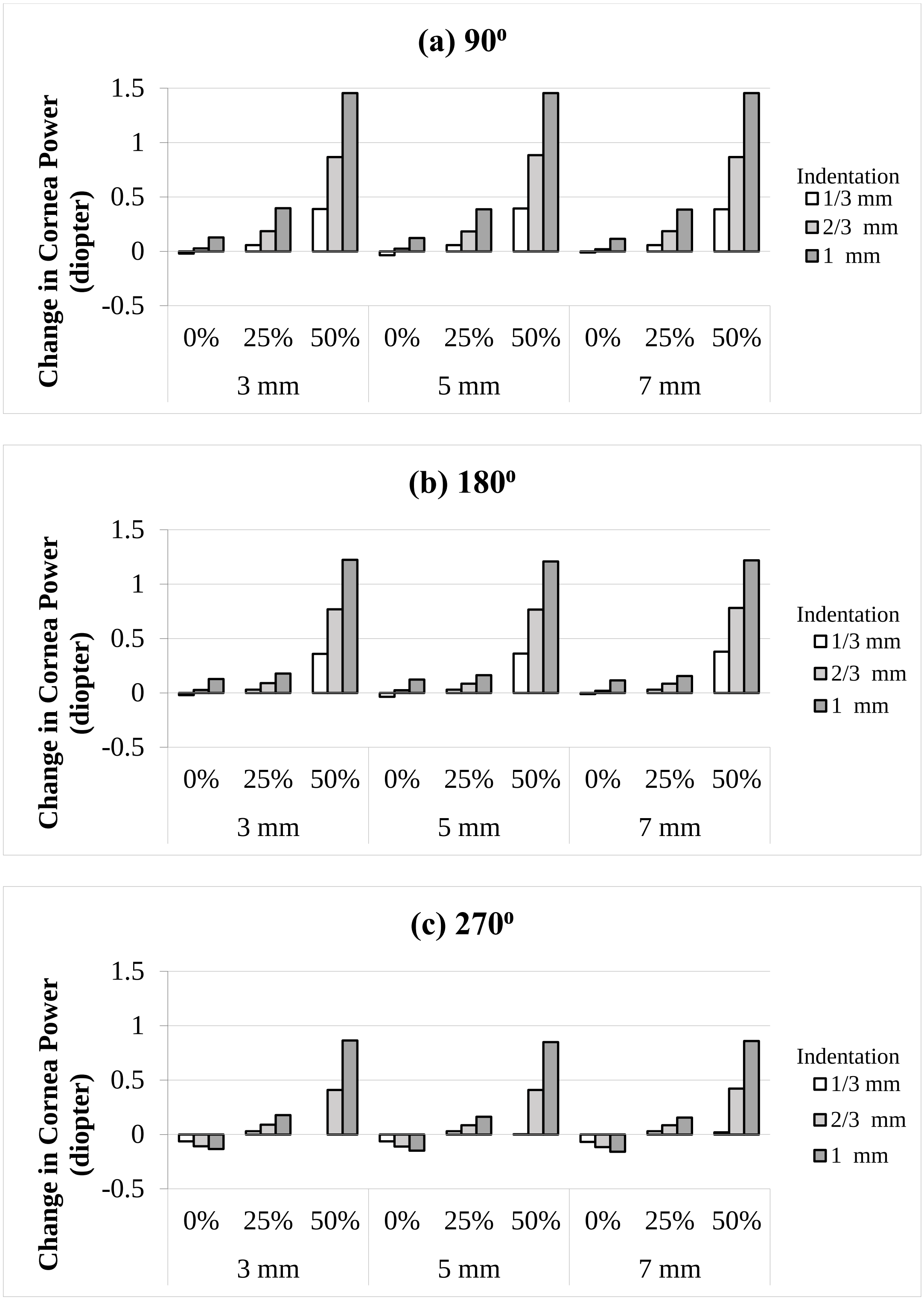

Figure 7.8 Cornea power change in diopter for different cornea thinning, buckle widths, indentations and extents: (a) 90˚, (b) 180˚ and (c) 270˚.

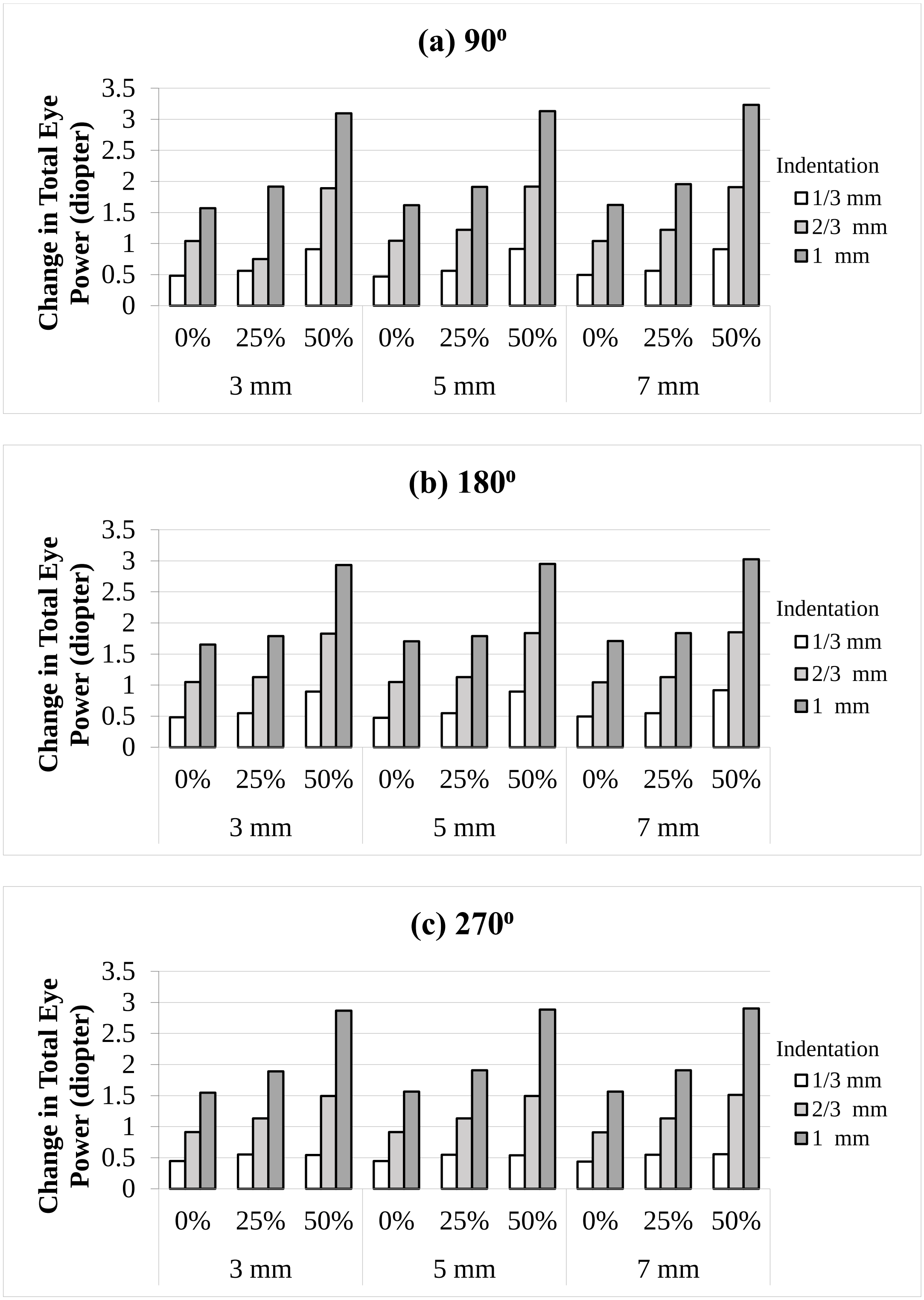

Figure 7.9 Total eye power change in diopter for different cornea thinning, buckle widths, indentations and extents: (a) 90˚, (b) 180˚ and (c) 270˚.

Figure 7.10 shows the percent change in the volume of the vitreous cavity for different buckle extents, widths and indentation of the buckle. The original volume of the vitreous cavity is about 5.543 ml. Figure 7.11 shows the normalized maximum von Mises located at the sclera at the contact edge of the segmental buckle to its analogues stress in inflation of 18.98 kPa for different buckle extent, width and indentation of the buckle. Figure 7.12 illustrates the von Mises stresses distribution for models with different extents and 5 mm thick buckles.

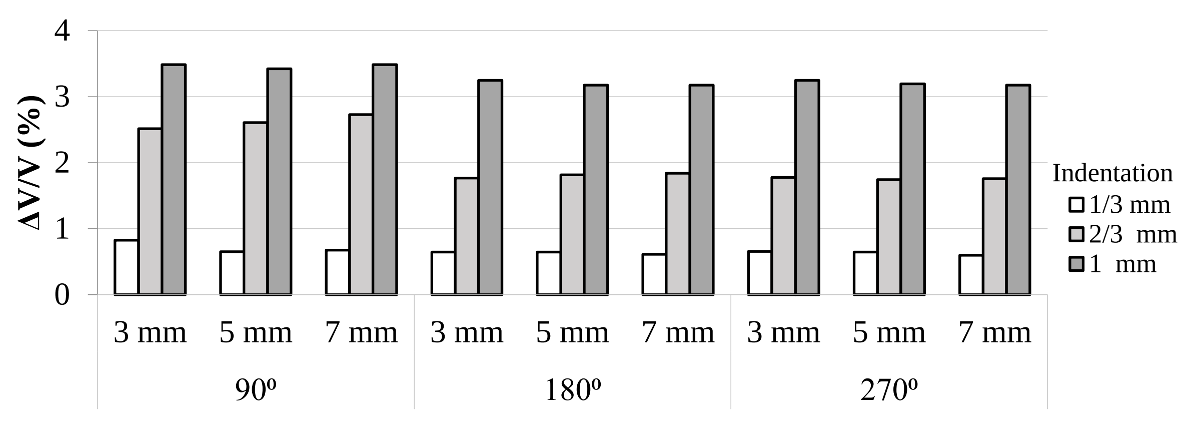

Figure 7.10 Change in vitreous cavity volume in terms of buckle width, extent and indentation.

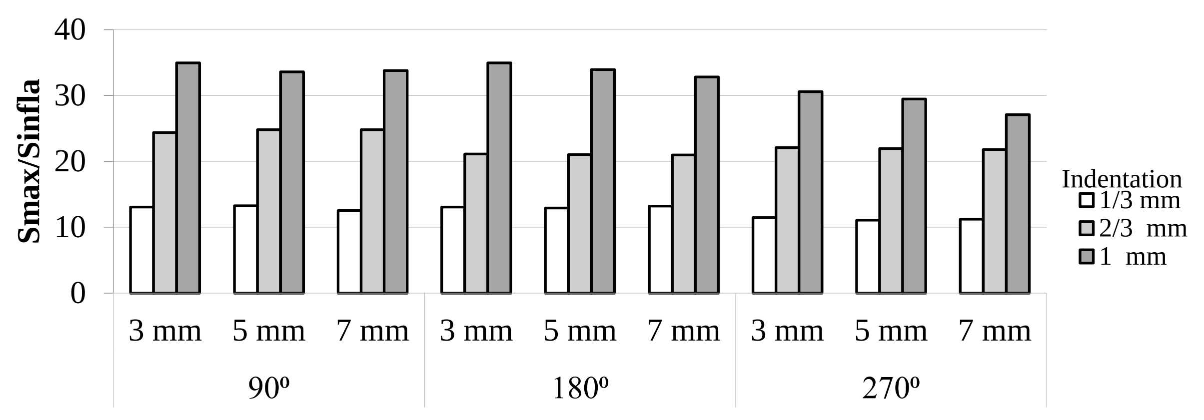

Figure 7.11 Normalized maximum von Mises stress in terms of the buckle width, extent and indentation.

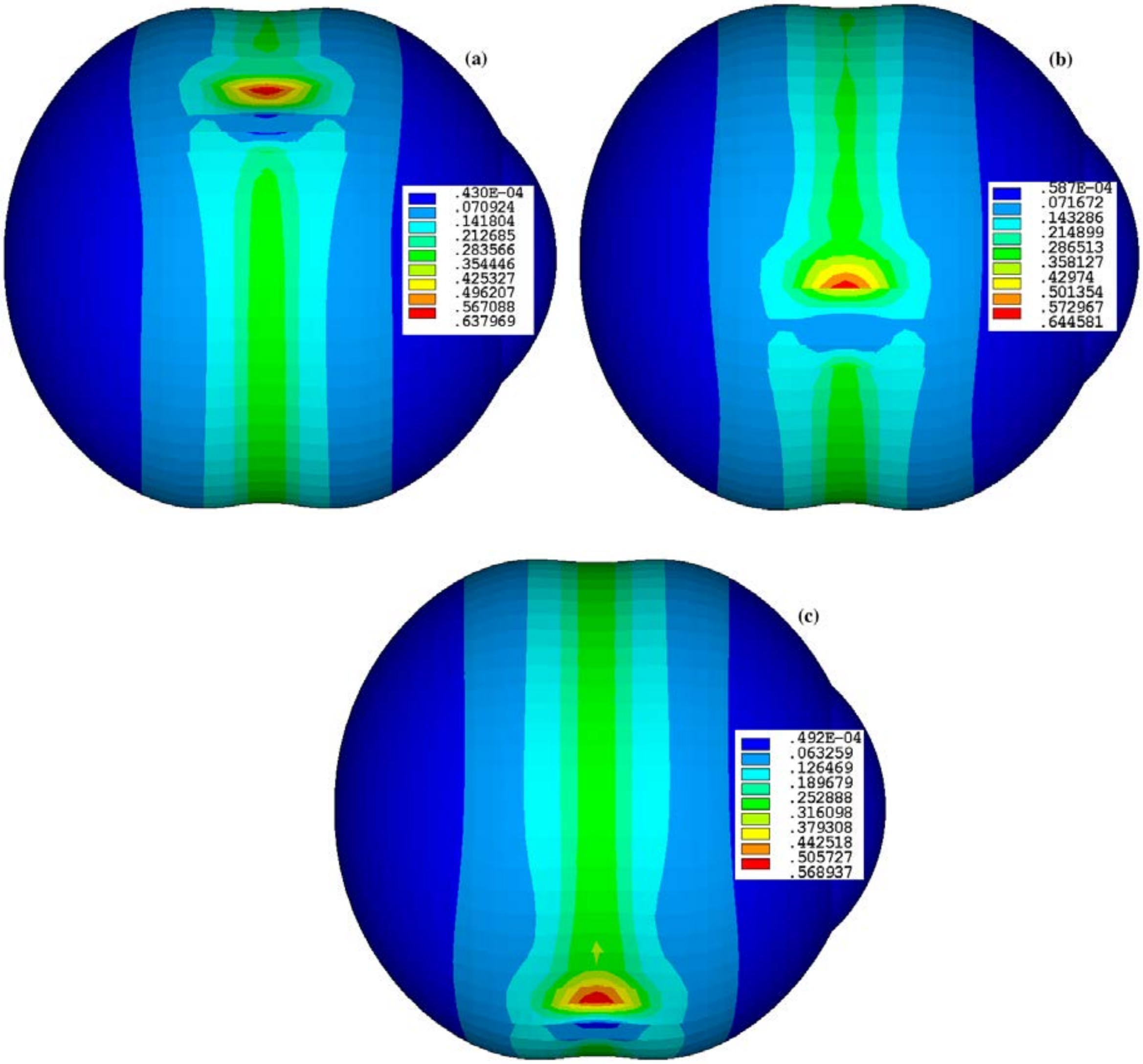

Figure 7.12 von Mises stress distributions for 5 mm buckle with (a) 90˚, (b) 180˚ and (c) 270˚.

7.2 DISCUSSION

In this investigation, the effect of a segmental buckle with different widths and extents and cornea thinning on axial length, anterior chamber depth, astigmatism, cornea tilt, cornea power, eye power, vitreous cavity volume and eye stresses using symmetric three-dimensional model of the eye and the buckle was assessed.

For eyes with segmental buckle, clinical studies reported that the axial length increased by amount of 0.98, 0.6, 0.77 and 0.48 mm and the extent of the buckle had no effect (Larsen et al. 1979, Toyota et al. 1995, Malukiewicz and Stafie 1999, Okada et al.1998); and change in the cornea power has been reported to be -2.2, -0.23, -0.22, 0.5, -1.1 and -0.07 diopters (Toyota et al. 1995, Hayasshi et al. 1997, Malukiewicz and Stafie 1999, Weinberger et al. 1999, Cetin et al. 2004, Karimian et al. 2006). The surgery was also reported to cause a reduction in anterior chamber depth of 0.02 and 0.204 mm (Larsen et al. 1979, Cetin et al. 2004).

In the analysis in this study, the axial length showed increased for all models driven mainly by indention amount where width, extent and thinning had smaller effect. The increase in the axial length for 5 mm buckle width with 180˚ extent on eye with normal cornea is about 0.21, 0.44 and 0.68 mm for 1/3, 2/3 and 1 mm of indentation, respectively, which is close to the clinical reported results and that extents had no effect on the axial length.

For cornea power, increasing indentation and corneal thinning had large effect on increasing the power change which is also added to the total power of the eye. For 5 mm buckle with a 180˚ extent at a 1 mm indentation, the change in cornea power was 0.12, 0.16 and 1.21 diopters for 0, 25 and 50% cornea thinning, respectively, and it was 1.45, 1.21 and 0.85 diopters for 90˚, 180˚ and 270˚ buckle extent, respectively, of 50% cornea at 1 mm indentation. For 0% thinned cornea, the results are close to the reported power change by clinical studies.

An astigmatism error of cornea is induced by indentation and thinning where higher steepening occurred at meridian parallel to center of buckling for all models. A 5 mm buckle with a 180˚ extent at 1 mm indentation had astigmatism error of about 0.09, 0.22 and 1.35 diopters for 0, 25 and 50% cornea thinning, respectively. The astigmatism error for 50% cornea thinning was 0.16, 1.35 and 3.29 diopters for 90˚, 180˚ and 270˚ buckle extent, respectively. Tilting of the cornea was noticed away from buckling location and increased as the buckle extent decreased being 1.69, 1.15 and 0.24 degrees for 90˚, 180˚ and 270˚ buckle extent, respectively, for normal cornea thickness at 1 mm indentation.

Maximum stresses from buckling were located at the edge of the buckle contact on the sclera for all models. An increase in indentation cause a stress increase, for example, the stress increased by a factor of 13, 21 and 34 for a 1/3, 2/3 and 1 mm of indentation, respectively, with buckle of 5 mm width and 180˚ extent. As buckling indentation, the volume of vitreous cavity decreased, for example, it was 0.65, 1.82 and 3.17% of original volume, respectively, for 1/3, 2/3 and 1 mm of indentation with a 5 mm buckle and 180˚ extent.

In conclusion of modeling encircling buckling using finite element analysis, the axial lengths of all models were increased mainly by indentation where the axial length change has its larger effect in the total eye power. Increased cornea thinning, buckle width and changing the buckle extent had little effect on the axial length change. The analysis showed that more thinning of the cornea can induce the astigmatism and myopic error in the cornea. The analysis also showed that increasing the buckle extent can increase the astigmatism error and reduce the tilt of the cornea. All cases had reduction in their vitreous cavity volume and increase in the maximum stress on the sclera at the edges of the segmental buckle where both are induced most by the amount of indentation. The addition of segmental buckle an encircling band can induce greater refractive error in the cornea and increased axial length for smaller indentation than without buckle.

8.0 RIGIDITY IN BUCKLED AND UNBUCKLED EYE

In ophthalmology, the rigidity of the eye refers to the pressure-volume relationship and how the intraocular pressure changes the eye the volume. This is important in surgery for determining if adding or replacing the vitreous fluid is necessary. The pressure-volume relationship has been expressed in different forms, for example, power, linear, logarithmic and differential form (Palllikaris et al. 2010). Experimental studies were conducted on enucleated eyes where buckled and unbuckled eyes are injected by saline solution and the pressure is recorded. The main finding was that buckling reduced the rigidity of the eye. No significant difference was found in injecting gas or saline solution and the mechanism of the reduction in the rigidity of buckled eyes was explained by the change of the sclera shape resulting in different stresses (Friberg and Fourman 1990, Jones et al. 1990, Whitacre et al. 1992). In this part of study, the eye rigidity was studied for cornea thicknesses, buckle indentations, locations of the band and buckle extents.

The model of unbuckled eye was pressurized from an initial pressure and the increase of the volume in both chambers was added to represent total volume of the globe. The model was analyzed with selective band widths of 2.5 and 3.5 mm and indentations of 0.5 and 1.5 mm and corneal thinning of 0% and 50% and at locations of anterior, equator and posterior sclera. For segmental buckle model, the rigidity of 5 mm buckle in one, two and three quadrants with 1 mm indentation and with 0%, 25% and 50% cornea thinning was analyzed. For assessing the mechanism of the rigidity difference in buckled eye, the stresses along the sclera was compared before and after pressurizing for both buckled and unbuckled eyes.

8.1 RESULTS AND DISCUSSION

Figure 8.1 shows results of the experimental work by Friberg and Fourman and our finite element model of unbuckled and buckled eye with 2.5 mm thick band. The initial pressure is about 23.3 mmHg with maximum obtained radius of the band of 10.44 mm in the model and 10.19 mm in the experiment. The results of the model show the rigidity, which is the slope of the pressure-volume line, is reduced by buckling. The buckled eyes have good match to the experimental results, whereas the unbuckled eyes have a greater deviation. This may be from activation of both the fibers and matrix in sclera rather than constrained fibers in buckled eyes as explained in the experiment. This also can give insight into the mechanism of the difference between rigidity in buckled and unbuckled eyes in surgery that elastic matrix is more strained than fibers in buckled eyes.

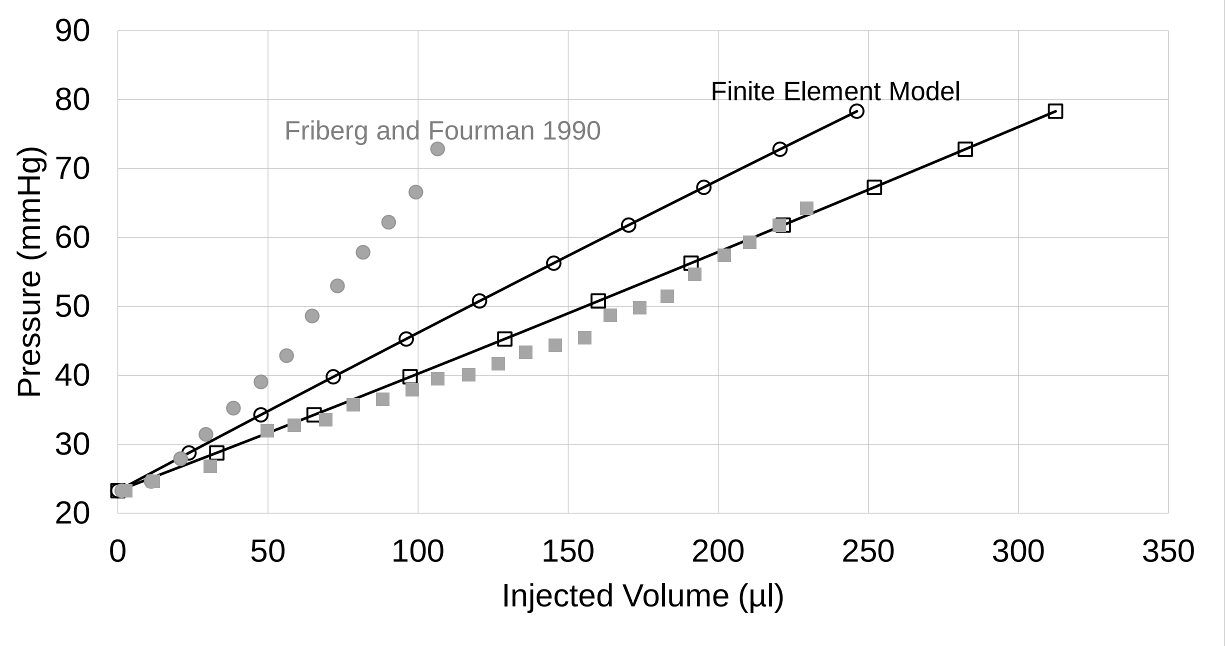

Figure 8.1 Pressure-volume changes for unbuckled (o) and buckled (□) eye with 2.5 mm thick band from an experiment (Friberg and Fourman 1990) and the finite element model.

In finite element model, the pressure-volume relationship is linear-like function and thus the rigidity (k) is calculated as the slope of a line fitted to the data (mmHg/µl). Figure 8.2 gives rigidity of an equatorial 2.5 mm and 3.5 mm band with a 0.5 and 1.5 indentation in 0% and 50% thinned cornea. Figure 8.3 gives rigidity of anterior and posterior 3.5 mm band with a 0.5 and 1.5 indentation in 0% and 50% thinned corneas. Figure 8.4 gives rigidity of 5 mm segmental buckle at 1 mm of indentation with one, two and three quadrants and 0%, 25% and 50% corneal thinning.

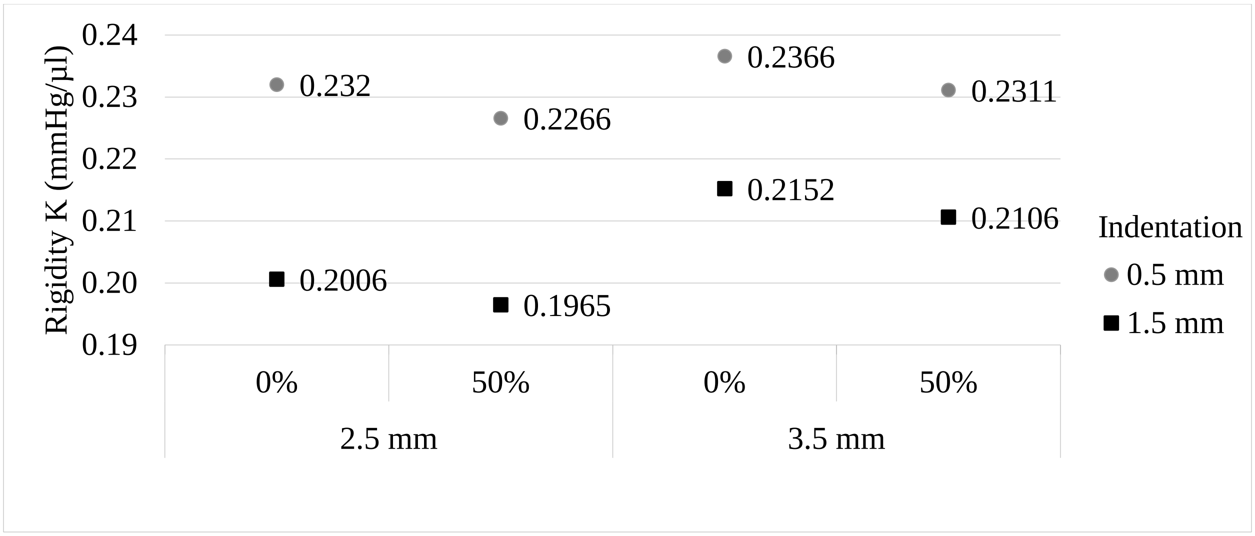

Figure 8.2 Rigidity of buckled eyes at equator with 2.5 and 3.5 mm wide, 0% and 50% cornea thinning and 0.5 and 1.5 mm of indentation.

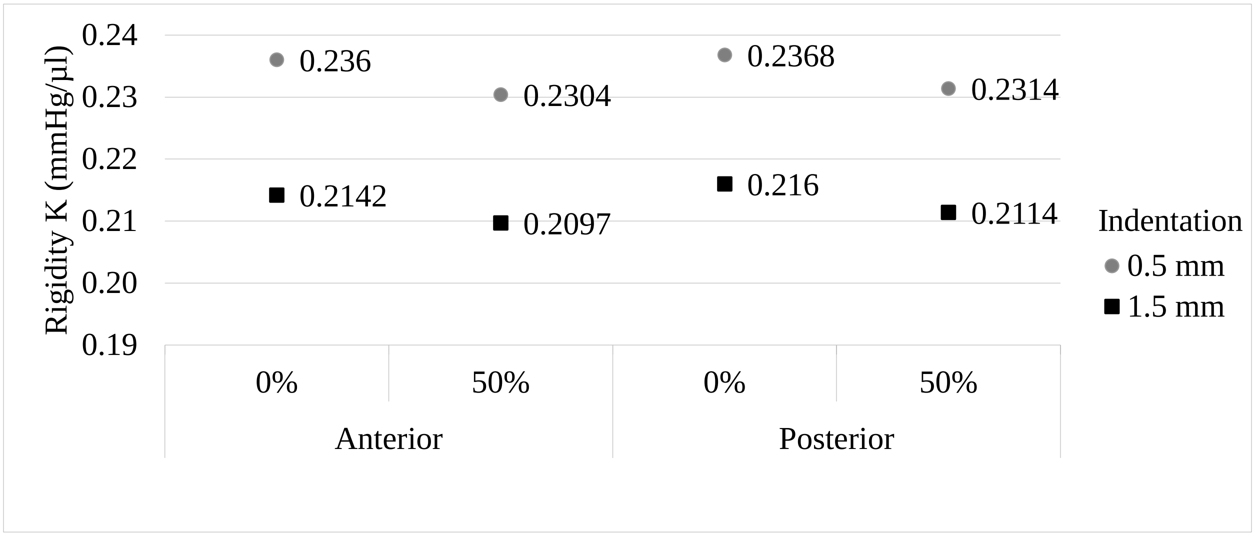

Figure 8.3 Rigidity of buckled eyes with a 3.5 mm band and with 0% and 50% cornea thinning, 0.5 and 1.5 mm of indentation at the anterior and posterior of the eye.

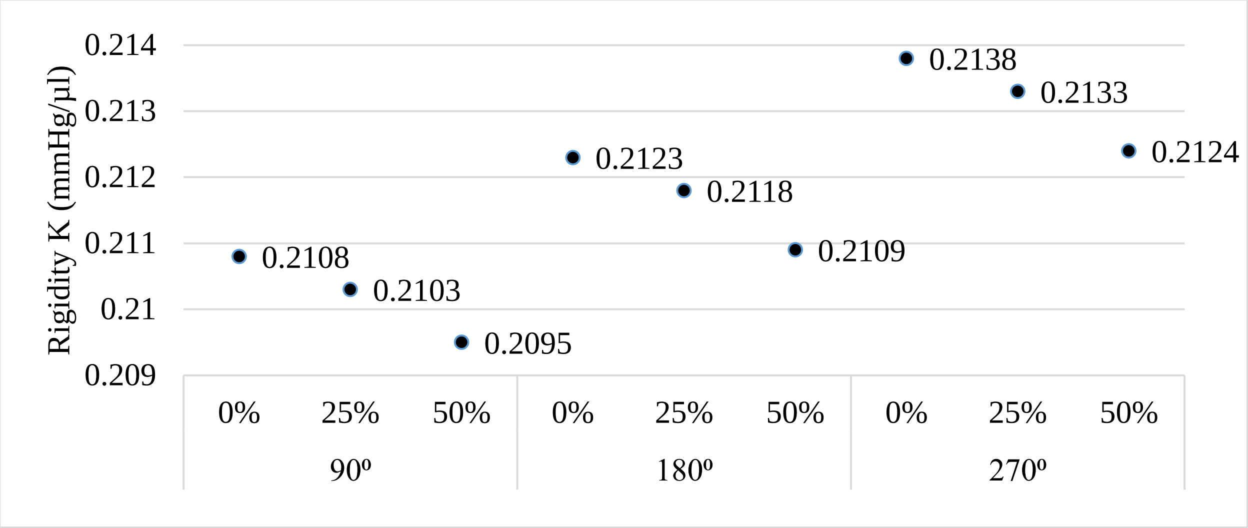

Figure 8.4 Rigidity of model with a 5 mm width and different segmental buckle extents and cornea thinning at 1mm indentation.

The rigidity of the eye showed to be decreased as it got buckled and as the band width decreased and location became closer to the limbus and the extent of the segmental buckle decrease. Furthermore, increase the indentation and cornea thinning of decrease the rigidity of the eye where indentation had the large effect on the rigidity. The conclusion of effect of width and indentation match the conclusion by the reported experiment (Friberg and Fourman 1990, Jones et al. 1990, Whitacre et al. 1992).

To compare added directional stresses in models without and with buckling, model of a 2.5 mm band at 1.5 mm at an initial pressure of 15 mmHg were analyzed at final pressure of about 80 mmHg. The additional circumferential (hoop) and along the sclera (axial) stresses, within its thickness, by pressurizing were calculated as the difference between final and initial stage. Figure 8.5 gives the added hoop and axial stress for buckled and unbuckled eye where the solid line indicates the equator position.

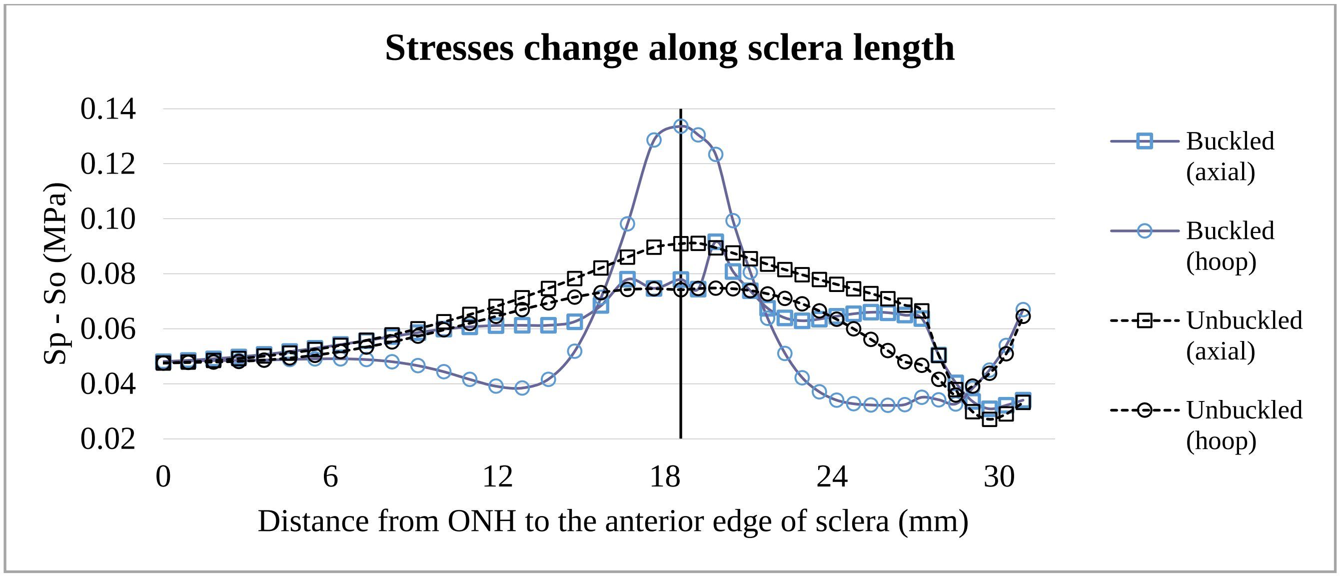

Figure 8.5 Plot of the added hoop and axial stress in unbuckled and buckled eye along the sclera (solid line for equator position).

The results showed that the stress at the edges of the sclera of both models has almost same stresses where the deviation of hoop and axial stress is larger reaching maximum peak at the equator. Friberg and Fourman (1990) explained the decrease in rigidity by the buckle as the change in the shape of the eye, for example, from sphere-like to cylinder-like shell with close ends. In structure mechanics, the latter shape of same thickness and radius of the former shape has the hoop as twice of its axial stress and both stresses in spherical pressure shell causing more tension by the pressure and as a results the strains in that direction and more expansion in the eye. Since the finite element allowed for measuring the stresses, the hoop stress showed more deviation than axial stress where it is higher tension close to the band.

In the summery analysis and modeling eye rigidity using finite element showed that the rigidity decreased by the buckling surgery and as width decreased and indentation increased which is same conclusion by the reported experiments. The finite element model showed rigidity decreased as the band location from the limbus and segmental buckle extent in the three-dimensional model decreased and the cornea thinning increased. The analysis of added stresses added by adding volume in the eye showed the effect of changing the eye shape and as a results the rigidity decreased.

9.0 CONCLUSION

Axisymmetric and three-dimensional finite element model of the eye and scleral buckling components were developed. The models were used for the analysis of the stresses and deformation and its effect on the visual power for buckled eyes with different cornea thinning and encircling bands alone and with segmental buckles. Experimental measurements of the eye were done using a laser scanner.

The scanning of the buckled eyes showed that the axial length increased for all eyes. A pattern of deformation was found in the experiment where the cornea is tilting away from the center of buckle with the addition of a segmental buckle.

The results of the models for encircling band and for the segmental buckle indicates that the indentation mainly increase the axial length and it is most important factor in the myopic shift in the total eye power. The anterior chamber depth showed higher reduction for less cornea thinning, more band distance to limbus, higher indentation and wider band and the buckle. Greater thinning of the corneas caused more steepening in the cornea. Less extension of the segmental buckle caused high tilt of the cornea and decreased astigmatism in the three-dimensional model. Location of the band and its width in the axisymmetric model and the width of the buckle in the three-dimensional model had the least effect on the deformation and the stresses of the eye.

The vitreous cavity volume showed more reduction for higher indentation in all models. The resultant maximum stresses located in the sclera at the sclera-choroid interface in encircled eyes and at the sclera contact surface with the tip of the buckle. In both procedures, the stresses increased mainly with indentation magnitude.

Future work could improve the eye finite element model with a detailed geometry and characterization of all or most eye tissues as nonlinear material. This characterization can also assess the eye model for different surgeries. The sclera and cornea can be tested experimentally for tensile, shear and volumetric phase for different ages to be defined in a two fibers hyperelastic model. The crystalline lens can be modeled as composite lens consisting of the capsule, cortex and nucleus each of which with its defined materials.

Future work on the scleral buckling model could investigate the effect of the lens conditions and lens implantation in cataract surgeries. Effect of gray spots in the sclera which indicates thinned sclera can be also modeled and investigated as dead elements in the sclera thickness. For the surgery, local buckling using different number of segmental and radial buckle driven by suturing alone could be assessed as prescribed displacement along the sutures within explicit analysis where the mesh is less sensitive to the distortion of the element.

BIBLIOGRAPHY

Alastrué, V. (2005). Biomechanical Modeling of Refractive Corneal Surgery. *Journal of Biomechanical Engineering*, *128*(1), 150-156.

Aldhafeeri, R. (2015) Stress Analysis for Scleral Buckling of the Eye. Master's Thesis, University of Pittsburgh.

Allan F. Bower. (2009). Applied Mechanics of Solids (Vol. XVII), *CRC Press Taylor & Francis Group*

Argento, A., Kim, W., Rozsa, F. W., DeBolt, K. L., Zikanova, S., & Richards, J. R. (2014). Shear Behavior of Bovine Scleral Tissue. *Journal of Biomechanical Engineering*, *136*(7),071011.

Atchison, D. A., Jones, C. E., Schmid, K. L., Pritchard, N., Pope, J. M., Strugnell, W. E., & Riley, R. A. (2004). Eye shape in emmetropia and myopia. *Investigative Ophthalmology and Visual Science*, *45*(10), 3380–3386.

Atchison, D. a, Markwell, E. L., Kasthurirangan, S., Pope, J. M., Smith, G., & Swann, P. G. (2008). Age-related changes in optical and biometric characteristics of emmetropic eyes. *Journal of Vision*, *8*(4), 29.1-20.

Atchison, D. A., Pritchard, N., Schmid, K. L., Scott, D. H., Jones, C. E., & Pope, J. M. (2016). Shape of the Retinal Surface in Emmetropia and Myopia, *46*(8), 2698–2707.

Baino, F. (2010a). Scleral buckling biomaterials and implants for retinal detachment surgery. *Medical Engineering and Physics*, *32*(9), 945–956.

Baino, F. (2010b). The use of polymers in the treatment of retinal detachment: current trends and future perspectives. *Polymers*, *2*(3), 286–322.

Battaglioli, J. L., & Kamm, R. D. (1984). Measurements of the compressive properties of scleral tissue. *Investigative Ophthalmology and Visual Science*, *25*(1), 59–65.

Bhardwaj, V., & Rajeshbhai, G. P. (2013). Axial Length , Anterior Chamber Depth-A Study in Different Age Groups and Refractive Errors, *7*(10), 2211–2212.

Bisplinghoff, J. a, McNally, C., Manoogian, S. J., & Duma, S. M. (2009). Dynamic material properties of the human sclera. *Journal of Biomechanics*, *42*(10), 1493–1497.

Brinton, D. A., Wilkinson, C. P., Hilton, G. F., & American Academy of Ophthalmology. (2009). *Retinal detachment : principles and practice*. Oxford University Press.

Bishop, P. N. (2000). Structural macromolecules and supramolecular organisation of the vitreous gel. *Progress in Retinal and Eye Research*, *19*(3), 323–344.

Boubriak, O. a, Urban, J. P., Akhtar, S., Meek, K. M., & Bron, a J. (2000). The effect of hydration and matrix composition on solute diffusion in rabbit sclera. *Experimental Eye Research*, *71*(5), 503–514.

Bryant, M. R., Szerenyi, K., Schmotzer, H., & McDonnell, P. J. (1994). Corneal tensile strength in fully healed radial keratotomy wounds. *Investigative Ophthalmology and Visual Science*, *35*(7), 3022–3031.

Bryant, M. R., & McDonnell, P. J. (1996). Constitutive laws for biomechanical modeling of refractive surgery. *Journal of Biomechanical Engineering*, *118*(4), 473-481.

Burd, H. J., Judge, S. J., & Cross, J. a. (2002). Numerical modelling of the accommodating lens. *Vision Research*, *42*(18), 2235–2251.

Burton, T. C., Herron, B. E., & Ossoinig, K. C. (1977). Axial length changes after retinal detachment surgery. *Am.J.Ophthalmol.*, *83*(1), 59–62.

Cetin, E., Ozbek, Z., Saatci, A. O., & Durak, I. (2006). The effect of scleral buckling surgery on corneal astigmatism, corneal thickness, and anterior chamber depth. *Journal of Refractive Surgery (Thorofare, N.J. : 1995)*, *22*(5), 494–499.

Chang, S. D., & Kim, I. T. (2000). Long-term visual recovery after scleral buckling procedure of rhegmatogenous retinal detachment involving the macula. *Korean Journal of Ophthalmology : KJO*, *14*(1), 20–26.

Chernov, N. (2009). Circle Fit (Pratt method). *Mathworks*.

Coudrillier, B., Boote, C., Quigley, H. A., & Nguyen, T. D. (2013). Scleral anisotropy and its effects on the mechanical response of the optic nerve head. *Biomechanics and Modeling in Mechanobiology*, *12*(5), 941–963.

Coudrillier, B., Tian, J., Alexander, S., Myers, K. M., Quigley, H. A., & Nguyen, T. D. (2012). Biomechanics of the Human Posterior Sclera: Age- and Glaucoma-Related Changes Measured Using Inflation Testing. *Investigative Opthalmology & Visual Science*, *53*(4), 1714-1782.

Czygan, G., & Hartung, C. (1996). Mechanical testing of isolated senile human eye lens nuclei. *Medical Engineering and Physics*, *18*(5), 345–349.

Domniz, Y. Y., Cahana, M., & Avni, I. (2001). Corneal surface changes after pars plana vitrectomy and scleral buckling surgery. *Journal of Cataract and Refractive Surgery, 27*(6), 868–72.

Doyle, L., Little, J.-A., & Saunders, K. J. (2013). Repeatability of OCT Lens Thickness Measures With Age and Accommodation. *Optometry and Vision Science*, *90*(12), 1396–1405.

Dubbelman, M., Sicam, V. A. D. P., & Van Der Heijde, G. L. (2006). The shape of the anterior and posterior surface of the aging human cornea. *Vision Research*, *46*(6–7), 993–1001.

Dubbelman, M., & Van Der Heijde, G. L. (2001). The shape of the aging human lens: Curvature, equivalent refractive index and the lens paradox. *Vision Research*, *41*(14), 1867–1877.

Dzierka, M., & Jurczak, P. (2015). Review Of Applied Mathematical Models For Describing The Behaviour Of Aqueous Humor In Eye Structures. *International Journal of Applied Mechanics and Engineering*, *20*(4), 757–772.

Eilaghi, A., Flanagan, J. G., Tertinegg, I., Simmons, C. a, Wayne Brodland, G., & Ross Ethier, C. (2010). Biaxial mechanical testing of human sclera. Journal of Biomechanics, *43*(9), 1696– 701.

Elsheikh, A., Geraghty, B., Rama, P., Campanelli, M., & Meek, K. M. (2010). Characterization of age-related variation in corneal biomechanical properties. *Journa of the Royal Society*, *7*(51), 1475–1485.

Elsheikh, A., & Wang, D. (2007). Numerical modelling of corneal biomechanical behaviour. *Computer Methods in Biomechanics and Biomedical Engineering*, *10*(2), 85–95.

Elsheikh, A., Wang, D., Brown, M., Rama, P., Campanelli, M., & Pye, D. (2007). Assessment of corneal biomechanical properties and their variation with age. *Current Eye Research*, *32*(1), 11–19.

Elsheikh, A., Wang, D., Rama, P., Campanelli, M., & Garway-Heath, D. (2008). Experimental assessment of human corneal hysteresis. *Current Eye Research*, *33*(3), 205–213.

Elsheikh, A., Geraghty, B., Alhasso, D., Knappett, J., Campanelli, M., & Rama, P. (2010a). Regional variation in the biomechanical properties of the human sclera. *Experimental Eye Research, 90*(5), 624–33.

Elsheikh, A., Geraghty, B., Rama, P., Campanelli, M., & Meek, K. M. (2010b). Characterization of age-related variation in corneal biomechanical properties. *Journa of the Royal Society*, *7*(51), 1475–1485.

Elsheikh A, Whitford C, Hamarashid R, Kassem W, Joda A, Büchler P (2013). Stress free configuration of the human eye. *Med Eng Phys*, *35*(2), 211-216.

Fazio, M. A., Grytz, R., Morris, J. S., Bruno, L., Gardiner, S. K., Girkin, C. A., & Downs, J. C. (2014). Age-related changes in human peripapillary scleral strain. *Biomechanics and Modeling in Mechanobiology*, *13*(3), 551–563.

Fernandez, D. C., Niazy, A. M., Kurtz, R. M., Djotyan, G. P., & Juhasz, T. (2006). A finite element model for Ultrafast Laser-Lamellar Keratoplasty. *Annals of Biomedical Engineering*, *34*(1), 169–183.

Fisher, R. F. (1977). The force of contraction of the human ciliary muscle during accommodation. *Journal of Physiology*, *270*(1), 51– 74.

Friberg, T. R., & Lace, J. W. (1988). A comparison of the elastic properties of human choroid and sclera. *Experimental Eye Research*, *47*(3), 429–36.

Friberg, T. R., & Fourman, S. B. (1990). Scleral buckling and ocular rigidity. Clinical ramifications. *Arch Ophthalmol*, *108*(11), 1622–1627.

Geraghty, B., Jones, S. W., Rama, P., Akhtar, R., & Elsheikh, A. (2012). Age-related variations in the biomechanical properties of human sclera. *Journal of the Mechanical Behavior of Biomedical Materials*, *16*(1), 181–191.

Gilbert, M., Friedlander, M., & Grante, N. (1990). Corneal steepening in human eye bank eyes by compined hexagonal and transkeratotomy. Referactive corneal surgery, *54*, 126–130.

Gilmartin, B., Nagra, M., & Logan, N. S. (2013). Shape of the posterior vitreous chamber in human emmetropia and myopia. *Investigative Ophthalmology and Visual Science*, *54*(12), 7240–7251.

Girard, M. J. a, Downs, J. C., Burgoyne, C. F., & Suh, J.-K. F. (2009a). Peripapillary and posterior scleral mechanics--part I: development of an anisotropic hyperelastic constitutive model. *Journal of Biomechanical Engineering*, *131*(5), 051011.

Girard, M. J. A., Downs, J. C., Bottlang, M., Burgoyne, C. F., & Suh, J.-K. F. (2009b). Peripapillary and posterior scleral mechanics--part II: experimental and inverse finite element characterization. *Journal of Biomechanical Engineering*, *131*(5), 051012.

Goel, R., Crewdson, J., & Chignell, A. H. (1983). Astigmatism following retinal detachment surgery. *Br J Ophthalmol*, *67*(5), 327–329.

Graebel, W. P., & van Alphen, G. W. H. M. (1977). The Elasticity of Sclera and Choroid of the Human Eye, and Its Implications on Scleral Rigidity and Accommodation. *Journal of Biomechanical Engineering*, *99*(4), 203–208.

Grytz, R., Fazio, M. A., Girard, M. J. A., Libertiaux, V., Bruno, L., Gardiner, S., … Crawford Downs, J. (2014). Material properties of the posterior human sclera. *Journal of the Mechanical Behavior of Biomedical Materials*, *29*, 602–617.

Hayashi, H., Hayashi, K., Nakao, F., & Hayashi, F. (1997). Corneal shape changes after scleral buckling surgery. *Ophthalmology*, *104*(5), 831–837.

Hermans, E. a, Dubbelman, M., van der Heijde, G. L., & Heethaar, R. M. (2006). Estimating the external force acting on the human eye lens during accommodation by finite element modelling. *Vision Research*, *46*(21), 3642–50.

Hoeltzel, D. A. (1992). Strip Extensiometry for Comparison of the Mechanical Response of Bovine, Rabbit, and Human Corneas. *Journal of Biomechanical Engineering*, *114*(2), 202.

Holzapfel, G. a., & Gasser, T. C. (2001). A viscoelastic model for fiber-reinforced composites at finite strains: Continuum basis, computational aspects and applications. *Computer Methods in Applied Mechanics and Engineering*, *190*(34), 4379–4403.

Jennings, A. (2011). Sphere Fit (least squared). *Mathworks.*

Jones, I. L., Warner, M., & Stevens, J. D. (1992). Mathematical modelling of the elastic properties of retina: a determination of Young's modulus. *Eye (London, England), 6 (Pt 6),* 556–559.

Johnson, M. W., Han, D. P., & Hoffman, K. E. (1990). The effect of scleral buckling on ocular rigidity. *Ophthalmology*, *97*(2), 190–5.

Karimian, F., Moradian, S., & Anisian, A. (2006). Corneal topographic changes after scleral buckling. *European Journal of Ophthalmology*, *16*(4), 1–6.

Kawana, K., Okamoto, F., Hiraoka, T., & Oshika, T. (2006). Ciliary body edema after scleral buckling surgery for rhegmatogenous retinal detachment. *Ophthalmology*, *113*(1), 36–41.

Keeley, F. W., Morin, J. D., & Vesely, S. (1984). Characterization of collagen from normal human sclera. *Experimental Eye Research*, *39*(5), 533–42.

Keeling, S. L., Propst, G., Stadler, G., & Wackernagel, W. (2009). A mathematical model for the deformation of the eyeball by an elastic band. *Mathematical Medicine and Biology*, *26*(2), 165–185.

Kinoshita, M., Tanihara, H., Negi, A., Kawano, S. I., Ishigouoka, H., Ueda, Y., … Honda, Y. (1994). Vector analysis of corneal astigmatism after scleral buckling surgery. *Ophthalmologica*, *208*(5), 250–253.

Krag, S., Olsen, T., & Andreassen, T.T. (1997). Biomechanical characteristics of the human anterior lens capsule in relation to age. *Investigative Ophthalmology and Visual Science*, *38*, 357–363.

Krag, S, Andreassen, T.T. Mechanical properties of the human lens capsule. (2003). *Prog Retinal Eye Res*, *22*, 749–67.

Lanchares, E., Calvo, B., Cristóbal, J. A., & Doblaré, M. (2008). Finite element simulation of arcuates for astigmatism correction. *Journal of Biomechanics*, *41*(4), 797–805.

Larsen, J. S., & Syrdalen, P. (1979). Ultrasonographic study on changes in axial eye dimensions after encircling procedure in retinal detachment surgery. *Acta Ophthalmologica*, *57*(3), 337–43.

Lindquist, T., Rubenstein, J., Rice, S., Williams, P., & Lindstorm, R. (1986). Trapezoidal astigmatism keratotomy: quantification in human cadaver eyes. *Archives of Ophthalmology*, *104*, 1534–1539.

Ljubimova, D., Eriksson, A., & Bauer, S. (2008). Aspects of eye accommodation evaluated by finite elements. *Biomechanics and Modeling in Mechanobiology*, *7*(2), 139–50.

Malukiewicz-Wiśniewska, G., & Stafiej, J. (1999). Changes in axial length after retinal detachment surgery. *European Journal of Ophthalmology*, *9*(2), 115–9.

Michael, R., Mikielewicz, M., Gordillo, C., Montenegro, G. a, Pinilla Cortés, L., Barraquer, R. I., … Barraquer, R. I. (2012). Elastic properties of human lens zonules as a function of age in presbyopes. *Investigative Ophthalmology & Visual Science*, *53*(10), 6109–14.

Mortazavi, A. M., Simon, B. R., Stamer, W. D., & Vande Geest, J. P. (2009). Drained secant modulus for human and porcine peripapillary sclera using unconfined compression testing. *Experimental Eye Research*, *89*(6), 892–7.

Mrochen M., Seiler T.”Laser Application in Optholomgy” Applied Laser Medicine, 299-315, 2003.

Munnerlyn, C. R., Koons, S. J., & Marshall, J. (1988). Photorefractive keratectomy: A technique for laser refractive surgery. *Journal of Cataract & Refractive Surgery*, *14*(1), 46–52.

Norman, R. E., Flanagan, J. G., Rausch, S. M. K., Sigal, I. a, Tertinegg, I., Eilaghi, A., … Ethier, C. R. (2010). Dimensions of the human sclera: Thickness measurement and regional changes with axial length. *Experimental Eye Research*, *90*(2), 277–84.

Obi, E., Baker, C., Teo, M., Teo, J. (2005). *Rapid surgery*. Blackwell Pub.

Okada, Y., Nakamura, S., Kubo, E., Oishi, N., Takahashi, Y., & Akagi, Y. (2000). Analysis of changes in corneal shape and refraction following scleral buckling surgery. *Japanese Journal of Ophthalmology*, *44*(2), 132–8.

Pallikaris, I. G., Dastiridou, A. I., Tsilimbaris, M. K., Karyotakis, N. G., & Ginis, H. S. (2010). Ocular rigidity. *Expert Review of Ophthalmology*, *5*(3), 343–351.

Pandolfi, A., Fotia, G., & Manganiello, F. (2008). Finite element simulations of laser refractive corneal surgery. *Engineering with Computers*, *25*(1), 15–24.

Pandolfi, A., & Manganiello, F. (2006). A model for the human cornea: Constitutive formulation and numerical analysis. *Biomechanics and Modeling in Mechanobiology*, *5*(4), 237–246.

Pedrigi, R. M., David, G., Dziezyc, J., & Humphrey, J. D. (2007). Regional mechanical properties and stress analysis of the human anterior lens capsule. *Vision Research*, *47*(13), 1781–1789.

Petsche, S. J., Chernyak, D., Martiz, J., Levenston, M. E., & Pinsky, P. M. (2012). Depth-dependent transverse shear properties of the human corneal stroma. *Investigative Ophthalmology & Visual Science*, *53*(2), 873–80.

Pinsky, P. M., & Datye, D. V. (1991). A microstructurally-based finite element model of the incised human cornea. *Journal of Biomechanics*, *24*(10), 907–922.

Pinsky, P. M. and Datye, D. V. (1992) Numerical modelling of radial, astigmatic, and hexagonal keratotomy. *Refract. Corneal Surg*. 8, 164-172.

Pinsky, P. M., van der Heide, D., & Chernyak, D. (2005). Computational modeling of mechanical anisotropy in the cornea and sclera. *Journal of Cataract and Refractive Surgery*, *31*(1), 136–45.

Power, E. D., Stitzel, J. D., West, R. L., Herring, I. P., Duma, S. M., Tech, V., & Storm, O. D. (2000). a Nonlinear Finite Element Model of the Human Eye for Large Deformation Loading. *Journal Of Rehabilitation Research And Development*, (1999), 1999–2000.

Prasad, A., Fry, K., & Hersh, P. S. (2011). Relationship of age and refraction to central corneal thickness. *Cornea*, *30*(5), 553–555.

Richoz, O., Kling, S., Zandi, S., Hammer, A., Spoerl, E., & Hafezi, F. (2014). A constant-force technique to measure corneal biomechanical changes after collagen cross-linking. *PloS One*, *9*(8), e105095.

Rossi, T., Boccassini, B., Esposito, L., Iossa, M., Ruggiero, A., Tamburrelli, C., & Bonora, N. (2011). The pathogenesis of retinal damage in blunt eye trauma: finite element modeling. *Investigative Ophthalmology & Visual Science*, *52*(7), 3994–4002.

Ruberti, J. W., Roy, A. S., & Roberts, C. J. (2011). Corneal biomechanics and biomaterials. *Annual Review of Biomedical Engineering*, *13*, 269–295.

Slaz, J., Rowsey, J., Caroline, P., Azen, S., Suter, M., & Monlux, R. (1985). A study of optical zone size ans incision redeepening in experimental radial keratotomy. *Archives of Ophthalmology*, 103, 590–594.

Schutte, S., Van Den Bedem, S. P. W., Van Keulen, F., Van Der Helm, F. C. T., & Simonsz, H. J. (2006). A finite-element analysis model of orbital biomechanics. *Vision Research*, *46*(11), 1724–1731.

Sigal, I. a, Flanagan, J. G., Tertinegg, I., & Ethier, C. R. (2007). Predicted extension, compression and shearing of optic nerve head tissues. *Experimental Eye Research*, *85*(3), 312–22.

Sigal, I. a, Flanagan, J. G., Tertinegg, I., & Ethier, C. R. (2004). Finite element modeling of optic nerve head biomechanics. *Investigative Ophthalmology & Visual Science*, *45*(12), 4378–87.

Slaughter, W. S. (2002). The Linearized Theory of Elasticity, *Springer Science & Business Media.*

Smiddy, W. E., Loupe, D. N., Michels, R. G., Enger, C., Glaser, B. M., & deBustros, S. (1989). Refractive changes after scleral buckling surgery. *Archives of Ophthalmology*, *107*(10), 1469–71.

Stitzel, J. D., Duma, S. M., Cormier, J. M., & Herring, I. P. (2002). A Nonlinear Finite Element Model of the Eye with Experimental Validation for the Prediction of Globe Rupture, *46*(November).

Studer, H., Larrea, X., Riedwyl, H., & Büchler, P. (2010). Biomechanical model of human cornea based on stromal microstructure. *Journal of Biomechanics*, *43*(5), 836–42.

Studer, H. P., Riedwyl, H., Amstutz, C. a, Hanson, J. V. M., & Büchler, P. (2013). Patient-specific finite-element simulation of the human cornea: a clinical validation study on cataract surgery. *Journal of Biomechanics*, *46*(4), 751–8.

Tanihara, H., Negi, A., Kawano, S., Ishigouoka, H., Ueda, Y., Yoshida-Suzuki, S., … Honda, Y. (1993). Axial length of eyes with rhegmatogenous retinal detachment. *Ophthalmologica. Journal International D'ophtalmologie. International Journal of Ophthalmology. Zeitschrift Für Augenheilkunde*, *206*(2), 76–82.

Tonghe Zhang, C. H. (2014). Changes in Axial Length and Anterior Chamber Depth after Rhegmatogenous Retinal Detachment Repair. *Journal of Clinical & Experimental Ophthalmology*, *05*(06), 102–105.

Toyota, K., Yamakura, Y., & Hommura, S. (1995). Ultrasonographic evaluation of axial length changes following scleral buckling surgery. *Ultrasonography in Ophthalmology 14*, *58*, 100–103.

Uchio, E., Ohno, S., Kudoh, J., Aoki, K., & Kisielewicz, L. T. (1999). Simulation model of an eyeball based on finite element analysis on a supercomputer. *British Journal of Ophthalmology*, *83*(10), 1106–1111.

Wang, F., Lee, H. P., & Lu, C. (2007). Biomechanical effect of segmental scleral buckling surgery. *Current Eye Research*, *32*(2), 133–42.

Wang, H. Z., Chen, M. T., Chang, C. H., Tsai, M. C., Wu, W. C., & Chung, C. B. (1994). The changes of ocular axial length and corneal curvatures after scleral buckling for retinal detachment. *Gaoxiong Yi Xue Ke Xue Za Zhi = The Kaohsiung Journal of Medical Sciences*, *10*(2), 77–83.

Weinberger, D., Lichter, H., Loya, N., Axer-Siegel, R., Muzmacher, L., Gabbay, U., & Yassur, Y. (1999). Corneal topographic changes after retinal and vitreous surgery. *Ophthalmology*, *106*(8), 1521–4.

Whitacre, M. M., Emig, M. D., & Hassanein, K. (1992). Effect of buckling material on ocular rigidity. *Ophthalmology*, *99*(4), 498–502.

Whitford, C., Studer, H., Boote, C., Meek, K. M., & Elsheikh, A. (2015). Biomechanical model of the human cornea: Considering shear stiffness and regional variation of collagen anisotropy and density. *Journal of the Mechanical Behavior of Biomedical Materials*, *42*, 76–87.

Williams G.A., Aaberg Jr T.A.(2006). Techniques or scleral buckling. *Retina*, 4th Edition, 3 pp 2035- 2070.

Woo, S. .-Y., Kobayashi, A. S., Schlegel, W. A., & Lawrence, C. (1972). Nonlinear material properties of intact cornea and sclera. *Experimental Eye Research*, *14*(1), 29–39.